TU Delft

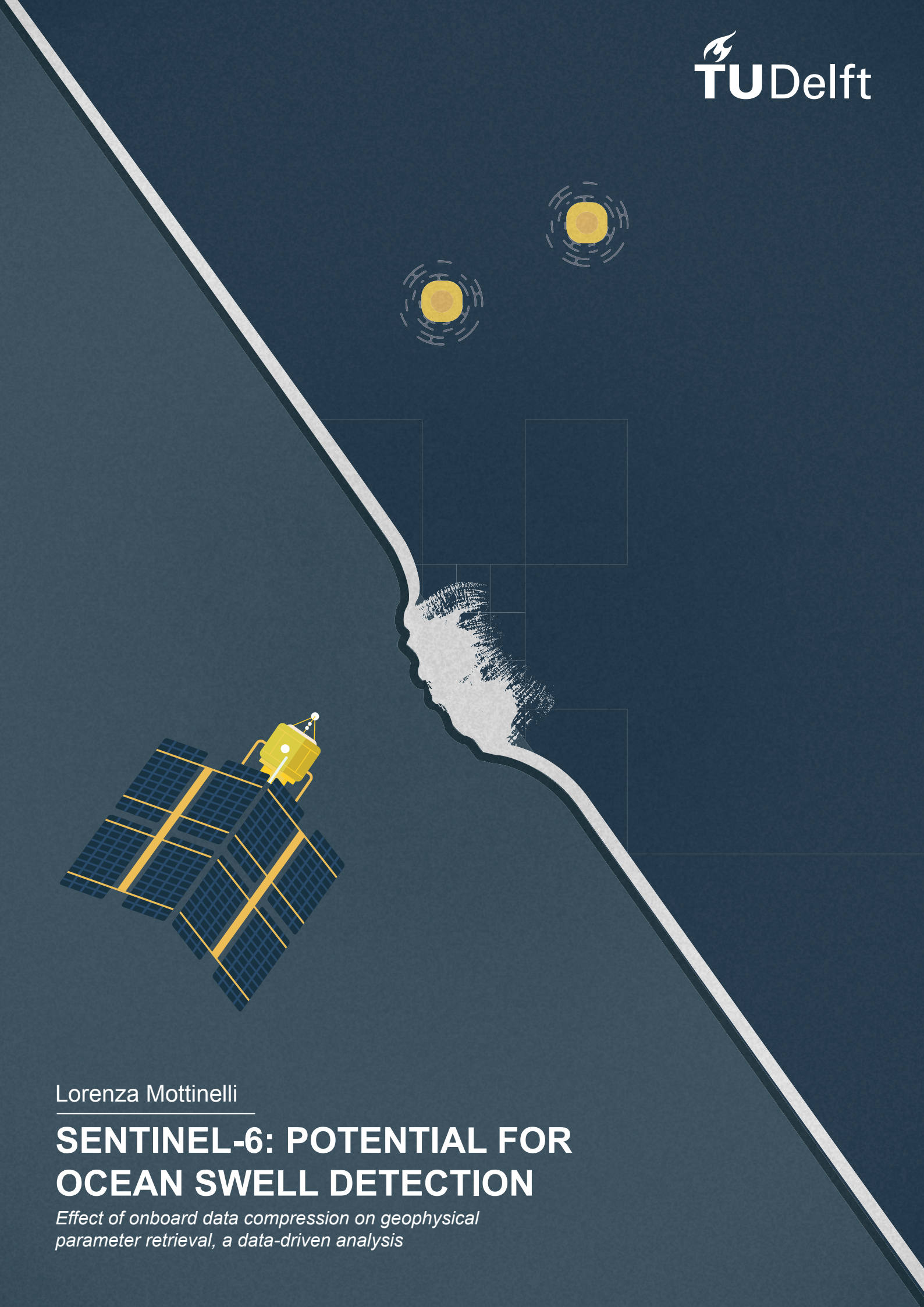

Lorenza Mottinelli

SENTINEL-6: POTENTIAL FOR OCEAN SWELL DETECTION

Effect of onboard data compression on geophysical parameter retrieval, a data-driven analysis

Sentinel-6: potential for ocean swell detection

Effect of on-board data compression on geophysical parameter retrieval, a data-driven analysis

To obtain the degree of

Master of Science

in

Aerospace Engineering

at the Delft University of Technology

To be defended publicly on Friday June 9th, 2023 at 09:30 AM

Author:	Lorenza Mottinelli
Student number:	4546121
Project duration:	February 2022 – June 2023

Chair (TU Delft):	Dr. Ir. W. (Wouter) van der Wal
Supervisor (TU Delft):	Dr. Ir. E.J.O. (Ernst) Schrama
Second supervisor (TU Delft):	PhD candidate Ir. O. (Ourania) Altiparmaki
External examiner (TU Delft):	Dr. Ir. J. (Jasper) Bouwmeester

TU Delft

Custom cover by @gloriazuelli

Preface

During the journey in Delft leading to the last dot in this report, I counted on the support of many people. I would like to first express my gratitude to my supervisors: Ernst, and Rania, thank you for providing me with continuous and concrete support during my thesis. I appreciated greatly the experience and foresight of Ernst while having a PhD supervisor like Rania who taught me a lot and provided me with many stimulating exchanges and ideas. Their understanding, patience, and availability were key during this thesis experience. I would like to also thank the Earth Console team for facilitating and providing access to the FFSAR processor, in particular M. Fornari (European Space Agency) and G. Sabatino (Earth Console) for the technical support. Thanks also to the NoR team for reviewing and approving the sponsorship request.

I am not really planning to write another thesis shortly, so I better take this chance to put down in writing right now how much it matters to me to be surrounded by such incredible family and friends. After all, *verba volant, scripta manent*.

To my friends: thank you for being the most important thing that Delft gave to me in these six years (together with an Engineering Diploma, fingers crossed at the time of writing). Thank you for making studying here so much easier, thank you for the laughs, the dances, dinners, parties, the predrinks, the singing, climbing, kitesurfing and biking biking biking biking biking biking, always together. If you were also my flatmate, thank you for the company during the fun and not-so-fun times, thank you for sharing your time or your moka with me, for keeping it gezellig, for making Delfgauwseweg my home. Matte, Anto, Paula, Emi, Patty, Iri, Reb, Alex, Miguel, Killian, Gilles, Beppe, Ben, Moosha, Pranav, Marina, Oscar, spaceflight friends, Nico, Greta, Gloria, Elisabetta, Anna, Marcelle. Thank you all for truly caring. It is a comforting feeling to move forward in life knowing that you will always be somewhere, scattered around in different countries but here with me, all in the same place.

Finally, I want to thank my family for always providing me with all that I needed to succeed, and for believing in me always: grazie mamma e papà per aver sempre creduto in me, e per avermi sempre dato tutto ciò di cui ho bisogno per raggiungere i miei obiettivi. Thank you, Cesare and Giulio for being the friends I did not have to look for, thanks for welcoming me home with hugs and aperitivos when I most needed them during my studies. Mil gracias Mundi for constantly supporting me and inspiring me to do my best. Grazie nonna Edith, nonna Franca e mamma, per avermi trasmesso la grinta che serve a buttarsi sempre, la forza di perseverare, e la sensibilità di provare sempre a capire.

Lorenza
Delft, June 2, 2023

Abstract

Swell waves are generated in the oceans by big storms and travel for thousands of kilometres until they reach the coast. They are characterised by their long wave period and due to their high energy, they affect coastal infrastructure, sediment transport, ocean mixing and wind stress. It is therefore of utmost importance to study swell as more and higher resolution observations directly benefit ocean weather forecasting together with climate modelling and monitoring. Currently, swell measurements are obtained by in-situ measurements (buoy, ships), wave models and satellite measurements, which are the most recent large update to the swell database as they provide global coverage. In particular, side-looking Synthetic Aperture Radar (SAR) satellites have been employed to obtain the wave spectrum by inverting the SAR spectrum, thereby retrieving swell period and direction. Wave spectra have been obtained also by CFOSAT, a dedicated mission equipped with a wave spectrometer. A potential of SAR nadir-looking altimeter Fully Focused SAR (FFSAR) waveforms to be used for swell monitoring was also most recently discovered. FFSAR data allows us to reach a theoretical along-track resolution of 0.5 m which provides increased accuracy for coastal parameter retrieval. Sentinel- 6, the newest nadir-altimeter in orbit, could be a great candidate for the experimentation of swell parameter retrieval using FFSAR data. Sentinel- 6 compresses the altimeter echoes on-board by truncating the last part of the waveform, the ”tail”, which is the portion that gets distorted in the presence of swell. The impact of this compression has been assessed so far only for Sea Surface Height measurements.

Given the added value that new nadir altimetry missions such as Sentinel- 6 could bring to the swell observation database, a performance analysis was carried out to assess the impact of truncating the waveforms on the retrieval of swell wave parameters from FFSAR spectra. As a first step, the area of interest (AOI) was chosen to ensure the collection of both raw and RMC waveforms. Then, Level-1A (L1A) High Resolution (HR) Non-Time Critical (NTC) data was retrieved for the chosen tracks. The L1A data was then processed by Earth Console to the Level-1B (L1B) FFSAR product. The FFSAR spectra corresponding to the raw and RMC portions of the FFSAR radargrams were generated and a first guess for the swell wave period was obtained. The relevant buoy data was retrieved from the National Data Buoy Center (NDBC) and the Coastal Data Information Program (CDIP) for the epochs corresponding to the satellite observations. Finally, the period estimated from the FFSAR spectra for both raw and RMC was compared with buoy measurements.

The data set obtained included all tracks collected by pass 119 and 206 over the AOI from the launch of the mission until February 2023. To define the best portion of the radargram to be considered to generate raw and RMC waveforms, a sensitivity analysis was performed, concluding that the best overall performance for FFSAR swell period retrieval is achieved for a cutting window stretching across-track from 7 to 13.5 km for raw and from 6.1 to 9.1 km for RMC, and along-track for 6.5 km. These ranges were found to be highly dependent on the choice of the polynomial fit to the waveforms. The FFSAR spectra corresponding to the best interval were computed for both raw and RMC, and the relative swell period estimates were retrieved accordingly and compared with the peak period from buoy spectra.

Overall, both raw and RMC retrievals consistently overestimated the swell period observed by the buoy, especially for passes where lower-period swells were observed. The Mean Absolute Error of the raw period retrievals was found to be lower than that of the RMC retrievals for all cases ran. Finally, When excluding passes where the error was 1σ or more away from the mean error value, the difference between the raw and RMC MAE dropped significantly (MAE raw = 0.95, MAE RMC = 1.15). It can be said that the retrieval of the swell period from FFSAR spectra derived from Sentinel-6 data is impacted by the presence of compressed (RMC) data, however, strong swells travelling in the azimuth direction (along-track) with along-track wind lead to reasonably accurate estimates of the swell period also for RMC altimetry data.

List of Figures

List of Tables

Nomenclature

Abbreviations

AOI	Area of Interest
CDIP	Coastal Data Information Program
CNES	Centre national d'études spatiales
CNSA	Chinese National Space Agency
CS2	CryoSat-2
DPD	Dominant Wave Period
ENL	Effective Number of Looks
ESA	European Space Agency
EUMETSAT	European Organisation for the Exploitation of Meteorological Satellites
GPP	Ground Processor Prototype
ILM	InterLeaved Mode
L1A	Level 1A data
L1B	Level 1B data
L2	Level 2 data
LRM	Low Resolution Mode
MAE	Mean Absolute Error
MWD	Mean Wave Direction
NASA	National Aeronautics and Space Administration
NDBC	National Data Buoy Center
netCDF	network Common Data Form
NOAA	National Oceanic and Atmospheric Administration
NTC	Non Time Critical
P4	Poseidon-4
PRF	Pulse Repetition Frequency
RAR	Real Aperture Radar
RMC	Range Migration Correction
RMSE	Root Mean Square Error
RS	Remote Sensing
S3	Sentinel-3
S6	Sentinel-6
SAR	Synthetic Aperture Radar
SMAP	Standalone Multimission Altimetry Processor
SSH	Sea Surface Height
SWH	Significant Wave Height
UFSAR	Unfocused Synthetic Aperture Radar
WDIR	Wind Direction
WSPD	Wind Speed

Symbols

B	Bandwidth	[Hz]
$\delta R_{\mathrm{atrack}}$	Along-track resolution	[m]
$\delta R_{\mathrm{xtrack}}$	Across-track resolution	[m]
δR_{sr}	Range bin width/ sampling distance	[m]
d	Water depth	[m]
f	Frequency	[s^{-1}]
h	Satellite orbital altitude	[m]
L	Wave wavelength	[m]
R_0	Minimum range to the specular point	[m]
T	Wave period	[s]
v	Velocity	[m/s]
λ	Wavelength	[m]
σ_0	Back-scatter coefficient	[-]
T	Time	[s]
T_s	Swell period	[s]
t_M	time of segment midpoint crossing for buoy recorded swells	[date-time]
Θ_a	Antenna beamwidth	[deg]

Constants

c	Speed of light	[2.988×10^8 m/s]
g	Gravitational constant	[9.81 m/s^2]
R_E	Radius of Earth	[6371.0 km]

Contents

1

Introduction

1.1. Background and relevance

The importance of monitoring swell

The variable most commonly associated with climate change is temperature. However, the climate system is represented by much more than the atmosphere. Changes in wind speed and surface waves play an important role in the characterisation of the ocean system. Waves and wind regulate in fact the flux of energy from the atmosphere to the ocean and influence the mechanisms of this interaction. Swell waves are an evolution of wind waves, that, once formed by strong storms, leave their generation area to travel for thousands of kilometres across the oceans (Alves, 2006). Wind waves and swell together account for more than 50% of the energy carried by waves on the ocean surface (surpassing the contribution of tides, tsunamis...) (Kinsman, 1984). This has been causing a growing concern regarding the impact of swell on the coastline and on offshore and coastal infrastructures (Semedo et al., 2011). In the Arctic for instance, as a result of climate change, longer ice-free periods occur and waves are exposed to stronger surface wind, posing a threat of inundation of the coastlines, which are particularly erodible in the Arctic (Barnhart et al., 2014). Swell has also been identified as a possible source of ocean mixing (Babanin et al., 2009) and of changes in the magnitude and direction of wind stress (Rieder and Smith, 1998). Sediment transport can also be affected by swell (Pomeroy et al., 2021). Studying swell therefore directly benefits ocean weather forecasting, industrial shipping route planning and more generally, climate monitoring and modelling (Schlembach et al., 2023).

Understanding the role of ocean swell, monitoring and modelling it is therefore critical for a diverse range of oceanographic research, coastal management initiatives, and ocean engineering projects (Alves, 2006). These challenges have always attracted the interest of the scientific community, especially since the first satellite-based observations started, leading to the publication of multiple papers on the topic (Ardhuin et al., 2009; Alves, 2006; Quataert et al., 2020; Young et al., 2011; Zou et al.,2019 and more). Multiple researchers focused on coastal swell studies (Pomeroy et al.,2021; Schlembach et al., 2023; Casas-Prat and Wang, 2020), which are of great relevance considering that 23%–37% of the world's population lives within 100 km of the shoreline (Glavovic et al., 2022). As the 2022 report by the International Panel on Climate Change explains, there will be an increase in coastal risks by "at least one order of magnitude over the 21st century" due to sea level rise (Pörtner et al., 2022). This emphasises the necessity of adaptation strategies, which largely rely on advancements in marine and wave forecasting models.

The need for satellite wave measurements

There are multiple available data sources for the observation of swell. These can be mainly classified into in-situ measurements (i.e.: buoys, ships), wave models and finally satellite measurements. While numerical models are the primary basis for forecasts, the input parameters that drive them can only be obtained through observational systems. Therefore, a synergistic utilization of all available sources is necessary to generate accurate predictions (and to satisfy the needs of the other applications mentioned in the previous paragraphs). Although measured waves exhibit a favourable degree of accuracy when compared to modelled data (Bruno et al., 2020), conventional techniques such as moored or static instruments solely provide time-series measurements at a single point or, in the case of ships, along a shipping route. This yields data sets characterized by a high temporal resolution but a low spatial resolution, thereby restrict-

ing information about the spatial variability of the parameters (Hauser et al., 2023). Moored buoys are primarily concentrated on the coasts of North America and Western Europe, leading to significant data gaps in other regions of the ocean. Meanwhile, ships provide limited and localized coverage across the globe. Furthermore, a majority of available in-situ sensors fail to provide high-quality, directional wave spectral data, which is essential to enhance models. To broaden the coverage of such observations, the use of drifting buoys is gaining popularity while directional platforms are being progressively introduced. To address the issue of limited spatial resolution, in-situ data can be augmented with Remote Sensing (RS) techniques, which provide global coverage regardless of weather conditions, and the capability to retrieve directional and historical wave data where other sensors have failed. On the other hand, the RS of waves currently lacks temporal resolution, but the situation is expected to improve with the selection of more dedicated missions and orbits.

Since the launch of the first Synthetic Aperture Radar (SAR) mission, Seasat (NASA 1978), SAR imagers (like Sentinel-1) have been used to estimate the spectral properties of waves longer than ~ 100 m (Wei et al., 2013), including swell. Waves shorter than such cutoff wavelength cannot be retrieved due to limitations of SAR imagers (Alpers et al., 1981). Properties like wave energy, mean period and direction can be derived from SAR imagers by inverting the SAR spectrum into a wave spectrum thanks to the numerical approach presented by Hasselmann and Hasselmann in 1991 ("the ocean-to-SAR spectral transform"). Another instrument allowing the retrieval of swell spectra is a real aperture near-nadir wave spectrometer such as SWIM, on board the Chinese French Ocean SATellite (CFOSAT), launched in 2018. CFOSAT is the first satellite having the primary goal of measuring ocean waves (Hauser et al., 2017) and it can resolve wavelengths below the cut-off limit imposed by the SAR resolution cell Hauser et al. (2023). SAR-interferometers like the most recently launched (December 2022) SWOT mission (NASA, CNES-the Centre National d'Études Spatiales) will also monitor waves (Morrow et al., 2019). The potential has been shown also for optical instruments, like the one on board Sentinel-2 (by the European Space Agency -ESA) (Kudryavtsev et al., 2017) to map the sea surface in daylight and the absence of cloud coverage. An overview of missions dedicated to observing the oceans is given in Figure 1.1.

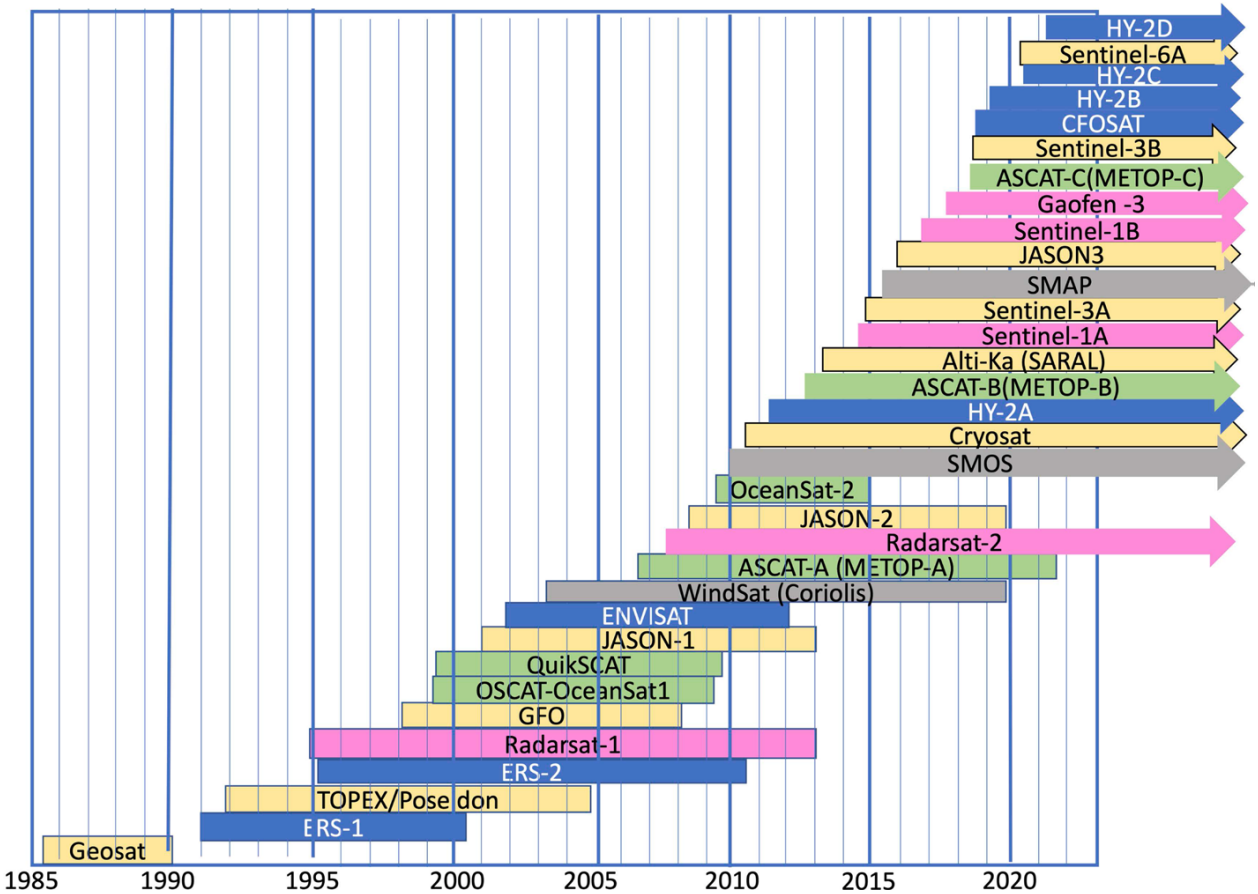

Figure 1.1: Chronologic overview of ocean-related missions. Radar altimeters (yellow), wind scatterometers (green), SAR (pink), microwave radiometers (grey), multi-instrument (blue) (Hauser et al., 2023)

The potential of altimetry for swell monitoring

Radar altimeters provide an even more continuous and long record of data but so far, the only wave parameter collected is the Significant Wave Height (SWH). With the advent of first SAR, then Fully Focused SAR processing (Egido and Smith, 2017), the along-track resolution of SAR altimeters can be narrowed from 300 m to a theoretical value of 0.5 m. The FFSAR altimeter waveform in particular can provide an increased accuracy for coastal parameter retrieval (Schlembach et al., 2023) and it features distortions due to the presence of swell (Moreau et al., 2018). These developments allowed Altiparmaki et al. (2022) to reveal the potential of FFSAR altimetry data to be used for the retrieval of swell wave parameters.

The possibility for altimetry to be a new source for swell monitoring, combined with the ever-growing need for global, continuous, and accurate observations of swell is a strong motivation to look further into the capabilities of the latest altimeter mission launched: Sentinel-6 (S6).

1.2. Research objectives and methodology

As recently highlighted by Rieu et al. (2021), the distortions caused by swell can be observed in the waveform's trailing edge, which corresponds with the portion of data that gets truncated by the RMC compression algorithm on board Sentinel-6. In preparation for the thesis, a Literature Study was carried out[1] to identify the existing research efforts directed towards the understanding of the impact of RMC truncation on parameter retrieval. At the time of writing the Literature Study (Jan 2022), two main studies were identified: one conducted pre-launch, and one used early mission data. The first one generated raw (non-truncated) and RMC waveforms with a mission performance simulator to then re-track both and retrieve Sea Surface Height (SSH), SWH and back-scatter coefficient. It was concluded that these products were not affected by RMC processing for nominal situations (not taking into account scenarios with extreme sea surface slopes) (Kuschnerus et al., 2018). The second analysis by Maraldi et al. (2021) also found negligible differences when comparing range, SSH, SWH and back-scatter obtained from raw data and RMC data from early mission data.

While Donlon et al. (2021) explain therefore that the RMC mode performs within expectations and is therefore employable globally, the presented research aims to investigate the added value of raw waveforms, which are currently collected only over designated calibration areas, in the context of swell studies. To understand if Sentinel-6, operating in its RMC mode, can be suitable for the potential retrieval of swell wave parameters, the novel methodology proposed by Altiparmaki et al. (2022) was applied to both raw and RMC FFSAR processed Sentinel-6 tracks produced over a calibration area and compared to buoy data with the scope to answer the following research questions:

> Does the truncation of waveforms performed by the RMC algorithm on board Sentinel-6 affect the potential of retrieving swell wave parameters from FFSAR spectra?

1.3. Report outline

The first chapter the reader is invited to consult is Chapter 2, where notions on swell waves and wave theory are presented, together with the SAR imaging mechanisms for side and nadir-looking instruments. An overview of altimetry principles is provided with key information about the Sentinel-6 mission and the Range Migration Compression algorithm used by its altimeter. Fully Focused SAR theory is also introduced. Chapter 3 describes the study area and the motivations for its choice and Section 3.2 gives an overview of the input Level1b dataset used for the analysis while the FFSAR data processing needed to produce the SAR altimetry spectra is explained in Section 3.3. Section 3.4 describes the buoy dataset used and the steps taken in processing it. The third chapter is concluded with an explanation of the performance metrics employed for the comparison between raw and RMC (Section 3.5). A sensitivity analysis on relevant settings can be found together with the corresponding results and their discussion in Chapter 4, followed by the conclusions and recommendations. Additional material supporting this research (buoy data, satellite passes information, ...) can be found in the Appendix, while more detailed background information is provided in the Literature Study.

[1]The Literature Study is available upon request to the author

2

Background and Fundamentals

This chapter provides an overview of the background principles required to better understand the thesis work, for more information, the reader is invited to consult the Literature Study. The basics of wave theory and swell are introduced first thing in Section 2.1 and Section 2.2. Then in Section 2.3 imaging mechanisms are explained for SAR imagers and satellite altimeters, with a focus on SAR and FFSAR spectra. An explanation of the Fully Focused SAR theory, which is applied in this work, can be found in Section 2.4. Key information about Sentinel-6 and the new RMC altimeter mode is also laid out in this chapter in Section 2.5.

2.1. Swell waves

The ocean surface has two main types of waves: wind seas and swell waves. During their formation and development, waves are classified as wind seas (from now on referred to as "wind waves"). However, when they move away from their source area or their phase velocity surpasses the wind velocity, they become known as swell waves (Semedo et al., 2011). Swell waves are generated by storms in the oceans and can travel for thousands of kilometres until they reach the shore (see Figure 2.1). They characterised by a long crest and travel undisturbed by local wind patterns (Wang et al., 2022). Swell waves carry the majority of the ocean surface's wave energy and are therefore associated with concerns regarding coastal and offshore infrastructure (Semedo et al., 2011). The main parameters that identify swell are the swell wave period and the wavelength/ distance between the crests. To distinguish swell waves from wind seas, some observation sites use a cutoff period of 10 s, meaning that all recordings with a smaller period are classified as wind seas, while other platforms measure also wind and can thereby determine the wind sea/ swell cut off period based on the current conditions (Coastal Data Information Program (CDIP), 2017). For reference, a 10-second period corresponds to a 156 m wavelength in deep water conditions (see Equation 2.3) while swell generated from particularly strong storms can reach even ~ 800 m of wavelength (period > 20 s) (Shillington, 1981).

Swell data can be retrieved from:

- **In-situ measurements:** National and international buoy networks
- **Satellite measurements:** From satellite products of SAR imagers like Sentinel-1 (ESA) or Gaofen, from the Chinese National Space Agency (CNSA). From dedicated radar spectrometer missions like CFOSAT (CNSA and CNES) or from SAR-interferometers like the SWOT mission (NASA, CNES), launched in December 2022 (Morrow et al., 2019). Potential has been shown also for optical instruments, like the one on board of Sentinel-2 (ESA) (Kudryavtsev et al., 2017) to map the sea surface from images with sun glitter (given that no clouds obstruct the target and that daylight is present).
- **Wave models:** WaveWatch-3 (TU Delft) or the Meteo France WAve Model

Finally, as Altiparmaki et al. (2022) suggested, swell parameters could also be inferred from satellite altimetry data.

Wave spectra from buoys A common mean to display swell wave information is by using wave spectra (an example is shown in Figure 2.2). In wave spectra, the wave energy observed for each frequency f (f = 1/T with T the wave period) and each wave travel direction relative to the geographical North is shown

Figure 2.1: A clear example of a swell wave system approaching the coast (wave breaking). Photo: Mathyas Kurmann//Unsplasj

in a polar plot. The frequencies increase in the radial direction (vice-versa for the periods), while the wave energy recorded is plotted on the z axis, as a color contour. The peak wave period for a given buoy spectra is the period of the wave group with the highest energy density, also referred to as dominant wave period (DPD) by the National Data Buoy Center (NDBC). In Figure 2.2 for example, both a swell system and a wind wave system are observed: the swell period can be derived from inverting the frequency at which the maximum swell energy is obtained ($1/\simeq 0.1$ leads to a 10s period, a small-scale swell), while the direction is seen directly from the plot (a mean direction of around 300°). Similarly, it can be derived that the wind waves have a period of $\simeq$ 3m and a direction of 45°. As the energy of the swell wave group is higher in this case, the peak wave period for this spectrum will correspond to the swell period.

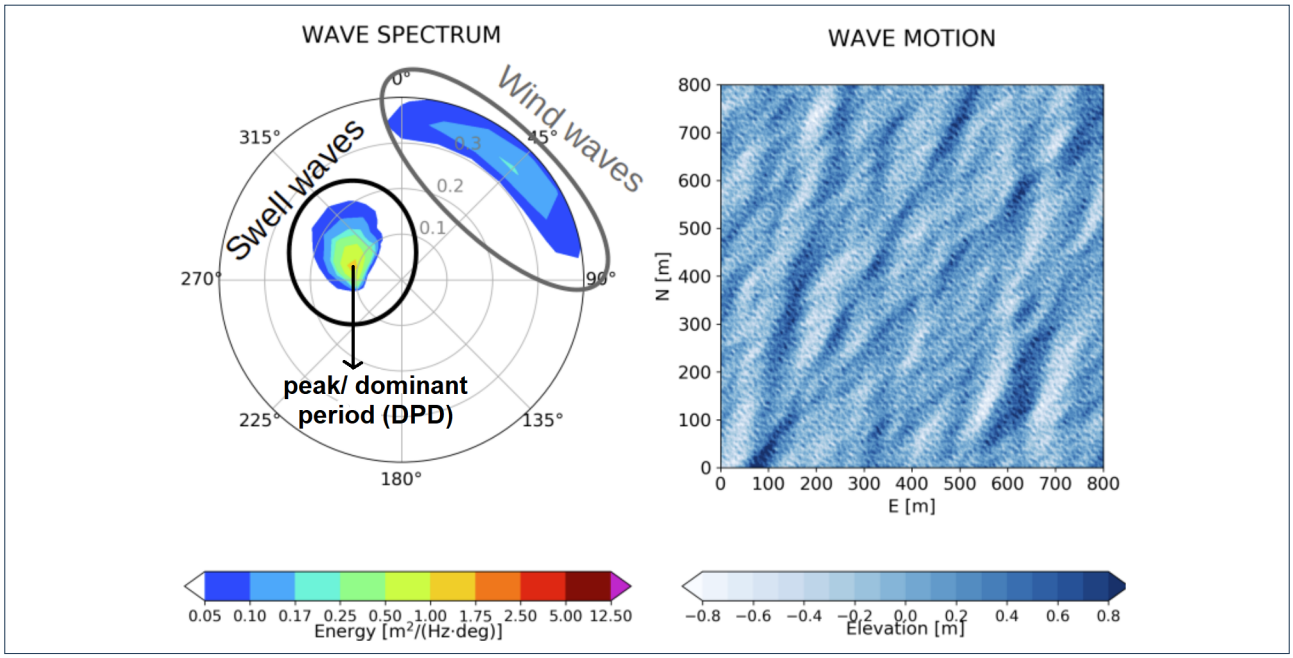

Figure 2.2: On the left, the wave spectral energy plot is shown for an observation of a system featuring both swell and wind waves. The radial scale indicates the wave frequency. On the right, the hypothesised wave motion is shown with its changing elevation. Example wave spectrum from the SWELLBEAT model (Swellbeat, 2020)

As mentioned in the introduction, limiting the swell observation data pool to buoy networks would be sub-optimal, as buoys are not evenly distributed in the ocean and provide a very limited spatial coverage. Measurements from ships and drifting buoys augment the available in-situ measurement capabilities but are still limited to the routes travelled by such sensors. Remote sensing instruments offer the clear advantage of a global coverage, most often independent from weather conditions, thereby providing a higher

spatial resolution for wave measurements. As accurate weather forecasting and climate models require both a high temporal and spatial resolution, the contribution of in-situ platforms remains fundamental to guarantee high temporal resolution observations in critical areas. To improve the temporal resolution of satellite wave measurements, data from different platforms can be combined into single products: this is becoming especially relevant as more dedicated ocean missions are being launched (like the recent CFOSAT and SWOT satellites) and more ways to retrieve wave parameters are being investigated. This is further discussed in Section 2.3.

2.2. Wave theory elements

Among the various sources of swell measurements mentioned above, buoy measurements were chosen to assess the accuracy of the satellite derived swell measurements (this is reasoned in more detail in Chapter 3). When the area of interest for the selection of satellite and buoy data was chosen, many factors were accounted for and are explained in depth in Section 3.1. Among the requirements for swell waves to be detectable, an area where deep water conditions apply had to be selected. This is because when swell waves move into shallow water, they decay rapidly, changing their characteristics (Naeser, 1979).

In order to determine the deep water threshold, linear wave theory was applied. The following assumptions were considered (Resio et al., 2002):

- The wave height, *H* is small when compared to the wavelength, *L* and the water depth, *d* (i.e. *H/L* « 1 and *H/d* « 1)
- The fluid is homogeneous and incompressible
- Surface tension can be neglected
- Coriolis effect due to the Earth's rotation can be neglected
- Pressure at the free surface is uniform and constant. The fluid is ideal or inviscid
- The particular wave being considered does not interact with any other water motions. The flow is irrotational
- The bed is a horizontal, fixed, impermeable boundary
- The wave amplitude is small and the waveform is invariant in time and space
- Waves are plane or long-crested (two-dimensional)

Deep water conditions apply when the relative depth d/L is greater than 0.5:

$$\frac{d}{L} > 0.5 \tag{2.1}$$

where L is the wavelength of the swell system considered. The terminology is introduced in Figure 2.3. In order assess if deep water conditions apply in the study area where swell is traveling, the dispersion

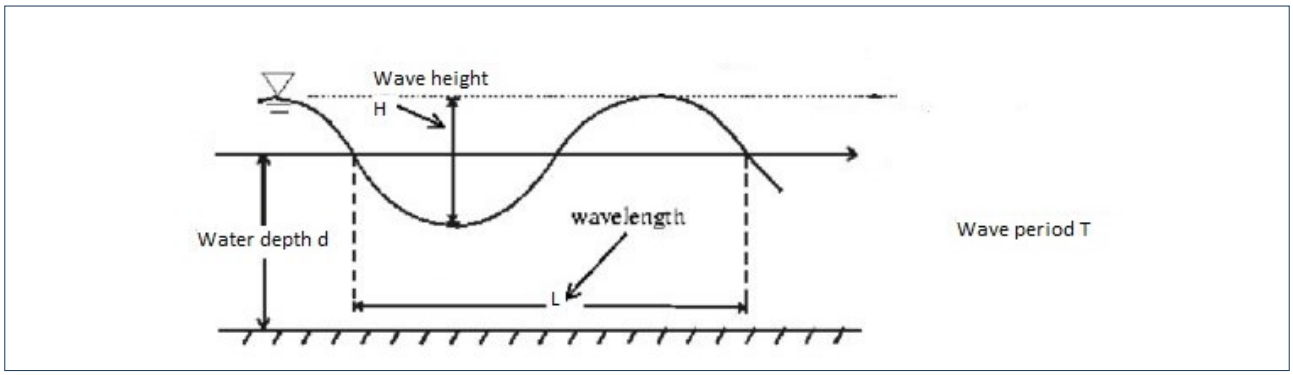

Figure 2.3: Small amplitude (linear) wave, adapted from (Nishanka et al., 2021)

relation will be employed to compute the wavelength of the swell system in question (Krogstad and Øivind A. Arntsen, 2000):

$$L = \frac{g}{2\pi} T^2 \tanh \frac{2\pi d}{L} \tag{2.2}$$

Where g is the gravitational constant ($9.81\ m/s^2$), T the given wave period (= DPD in case the peak period recorded by buoy data is used), d the water depth and L the wavelength. Through trial and error, the wavelength L can be solved for.

Using Equation 2.2, the wavelength corresponding to the highest buoy period recorded in such area in the timeline considered can be computed using the average depth of the study area ($d = d_{avg}$). If deep water conditions apply (can be assessed using Equation 2.1), then deep water conditions can be assumed for all the remaining timestamps in the dataset, where lower wave periods are observed.

For areas where deep water conditions apply, the wavelength of a given wave with period T can be derived using Equation 2.3.

$$L = \frac{g}{2\pi} T^2 \tag{2.3}$$

This allows to calculate the wave celerity $c = L/T$. The wave group velocity C_g of deep water waves can then be obtained using (Krogstad and Øivind A. Arntsen, 2000):

$$C_g = \frac{1}{2} c \tag{2.4}$$

The wave group velocity is particularly useful when computing the wave travel time, which can be relevant in case the timestamp of satellite observations needs to be matched with the one of buoy observations, as is the case for this study (see Subsection 3.4.2).

2.3. Swell from space

The potential of retrieving swell parameters from space-born radars was demonstrated since the launch of the first SAR missions: Seasat (NASA) and ERS-1 (ESA). SAR imagers are radars operating in the microwave range that measure the roughness of the sea surface and use the Doppler frequency of the back-scattered signal to achieve a very high resolution in the along-track direction (azimuth). The imaging mechanisms responsible for the wavelike patterns in radar images were identified early on and have been thoroughly studied, but due to the high non-linearity of the imaging process, it has never been possible to retrieve a one-to-one relation that allows the mapping of a radar image on the ocean wave spectrum (Alpers et al., 1981). This makes the interpretation of SAR wave data a challenge, however, Hasselmann and Hasselmann (1991) brought a significant contribution to the quantitative analysis of ocean wave spectra by introducing the first analytical model relating the SAR spectrum to a wave spectrum. The SAR imaging mechanisms are briefly introduced below together with the SAR spectra inversion principles and limitations.

2.3.1. SAR Imaging mechanisms

SAR imaging mechanisms include but are not limited to those applicable for lower resolution, Real Aperture Radars (RAR). In general, it is assumed for Bragg scattering to be the dominant backscattering process for incidence angles in the range of 20-70 deg (Hasselmann et al., 1985), so those at which most commonly space based SAR instruments operate. For nadir-looking platforms, operating at smaller incidence angle, the dominant back-scattering process is specular scattering (Valenzuela, 1978). For RAR systems, the wave images are generated by the modulation of the radar cross-section by long waves. This modulation has two main components: the tilt and hydrodynamic modulation, and a weaker range bunching component (Alpers et al., 1981):

- **Tilt modulation:** This is caused by the change in local incidence angle that occurs when Bragg-scattering waves are travelling on longer waves.
- **Hydrodynamic modulation:** This mechanism is the consequence of the surface water movement on the waves: water converges on the wavefront facing the direction of wave propagation, while it is smooth in the area behind the wave. This modulation is weaker than tilt modulation.
- **Range bunching:** Range bunching is caused by similarities between the incidence angle and the wave surface slope and its effect is a decrease in range resolution (Ardhuin et al., 2017).

Long ocean waves can also be seen by SAR due to tilt and hydrodynamic modulation, however, there is a third mechanism that comes into play due to the process allowing SAR instruments to reach a higher cross-track resolution. For SAR, localisation of targets cross-track is based on the Doppler frequency of their back-scattered signal. Targets with their own velocities in the range direction are therefore shifted in the SAR image, causing an additional modulation by velocity bunching:

- **Velocity bunching:** When ocean waves are imaged, the change in radial velocity of scatterers along the same wave causes the scatterers to be imaged at varying azimuth (flight) directions,

producing wavelike patterns in the radar image. Velocity bunching can be constructive (for long waves, wavelike patterns in the radar image can be associated to the ocean waves) or destructive (for short waves with random velocities (Kerbaol et al., 1998), radar images are smeared due to the acceleration of the scatterers and consequent degradation of azimuth resolution (Alpers and Rufenach, 1979)).

As Alpers et al. (1981) describe it, an example of this effect causes trains moving cross-track to be shifted in azimuth with respect to the rails: opposite travelling directions result in the shifting in azimuth to be in opposite directions. The dependence of the modulations transfer function on azimuthal angle is illustrated in Figure 2.4.

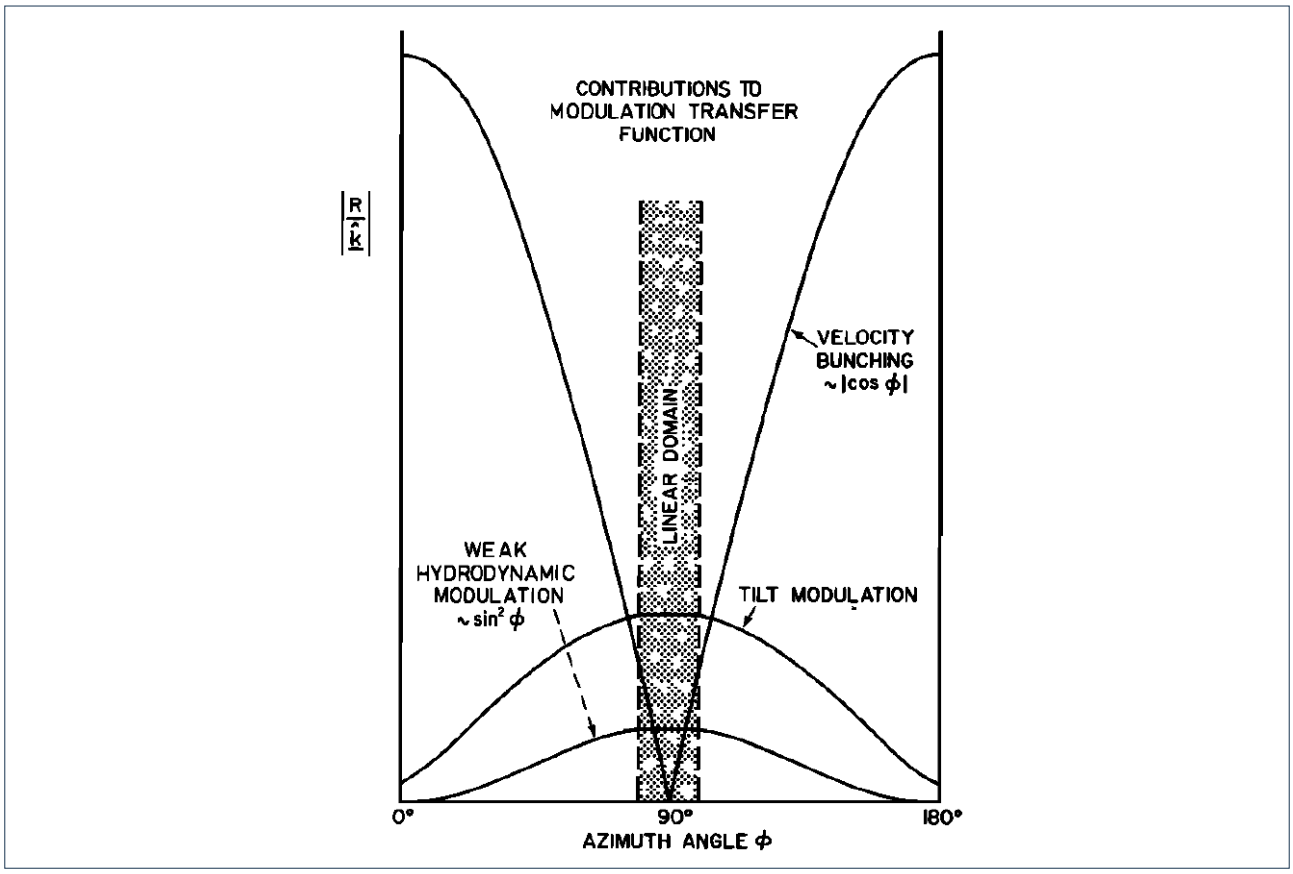

Figure 2.4: Contribution of different imaging mechanism to image modulation of ocean waves as a function of azimuth angle (Alpers et al., 1981)

It can be seen that velocity bunching is the dominant imaging mechanism for SAR, but for waves travelling in the range direction (cross-track), its effect vanishes. Range travelling waves are in fact best imaged by both SAR and RAR. Furthermore, for $\Phi = 0\,\mathrm{deg}$ and an angular interval around that, velocity bunching is a linear process (Alpers et al., 1981): the width of this interval increases for increasing wavelengths λ. The ocean wave spectra of waves travelling in such direction interval can then be obtained directly from the gray spectrum of a SAR image, as the hydrodynamic and tilt modulations can also be described by a linear transfer function for moderate sea states (Alpers and Hasselmann, 1978). For wave travelling in azimuth direction however, velocity bunching is present and is highly nonlinear, making the SAR spectra shape very different from the actual ocean wave spectra (Ardhuin et al., 2017). In principle, SAR should be able to detect azimuth-travelling waves that cannot be seen with RAR, however, due to this non-linearity, the wave spectra can be obtained from the image only for large wavelengths (in particular swell), while the shorter wind waves cause destructive velocity bunching (Alpers and Rufenach, 1979). To summarise, it can be said that:

SAR imagers are limited to observing waves with wavelengths greater than the azimuth cutoff wavelength λ_c: they cannot capture a comprehensive picture of smaller wavelength waves, which get blurred as a result of their motion

The cutoff wavelength depends on wave height and wind speed: low wind and low wave height conditions

lead to constructive velocity bunching Wan et al. (2020): swells are most often resolved successfully as proven by studies retrieving swell parameters from SAR and validating with buoy observations (Collard et al., 2009).

2.3.2. SAR spectra inversion and limitations of current platforms

The paper by Hasselmann and Hasselmann (1991) marked a significant advancement in comprehending SAR ocean wave imaging: the authors proposed the use of a closed-form expression relating SAR images to the corresponding ocean wave spectra: "the ocean-to-SAR spectral transform". Engen and Johnsen (1995) also made an important contribution by introducing a cross-spectral transform allowing the reduction of noise in the spectra and the removal of the $180\ \mathrm{deg}$ ambiguity in the direction of wave propagation. The ESA Level-2 wave mode products include both these spectrum retrieval algorithms (although it has to be noted that at times, the ambiguity removal algorithm fails to retrieve the correct wave direction) (Ardhuin et al., 2019).

The limitations imposed by the cutoff wavelength on SAR wave imaging can be improved by using RAR scatterometers like SWIM on CFOSAT, which can solve for wavelengths up to ~70 m (shorter than the 100-200 m cutoff of SAR (Wei et al., 2013)). CFOSAT provides directional wave spectra which allow to also solve the ambiguity issue that arises using some processors or products. For CFOSAT, the specified wavelength and directional resolutions are required to be at least on the same level as those achieved in wave buoy measurements. Additionally, they should be compatible with the frequency and directional resolutions used in numerical global wave models Hauser et al. (2017).

SAR altimeters have not been considered as a source of measurement of wave spectral properties until recently, when their potential for swell monitoring has been revealed by Altiparmaki et al. (2022). If further studied and exploited, using SAR altimeters could lead to a significant increase of remote sensing data regarding long ocean waves. Incorporating observations from altimeters with those collected by SAR imagers, interferometers and scatterometers would result in a direct increase in the availability of data with a high spatial resolution, thereby benefiting greatly the modelling and forecasting of weather and climate over the ocean. The fundamental principles of SAR altimetry and its relation to swell are therefore explained in the coming section.

2.3.3. Satellite altimetry

As we are now entering the fourth decade of satellite altimetry measurements, new and more complex instruments are being developed. It is therefore important to provide background information on the technology available in order to understand its capabilities and limitations, which are under the lens of scrutiny of this thesis work. The Global Climate Observing System programme recently updated the requirements on Essential Climate Variables. For global mean sea level, the 2022 report specifies a stability goal of $< 0.03\ mm/yr$ (necessary to detect the melting of permafrost) and a stability target of $3\ mm/yr$ (to detect a change in the rising rate of sea level) (World Meteorological Organization (WMO) et al., 2022). To satisfy these stringing requirements, the constellation of altimetry satellites monitoring sea level (together with wind speed, significant wave height and sea surface roughness), is updated with new instruments that are periodically launched in orbit to guarantee continuity of the time series measurements (their accuracy can be better visualised in Figure 2.5). The spatial resolution of such measurements has also increased and can now reach a few hundred meters along-track (Grgic and Bašić, 2021), thanks to the missions equipped with the latest Synthetic Aperture Radar technology, which is introduced in the upcoming paragraphs to allow a subsequent understanding of Fully Focused SAR.

Conventional altimeters "Conventional"-Low Resolution (LRM) Radars such as Jason1, Jason2, ERS1, ERS2, Envisat, had a footprint of a few kilometres along-track which could reach many kilometres with the increase of large-scale surface roughness (Raney, 1998). This causes inefficiencies in data retrieval in the proximity of the coast or in inland waters, where the footprint is contaminated by reflections from the land that get averaged in the signal. The LRM footprint is pulse-limited, meaning that is determined by the length of the pulse emitted by the radar. Shorter pulses allow for a narrower footprint and therefore higher resolution, enabling the detection of smaller-scale surface features, as the signal is averaged over a smaller area. The pulse-limited LRM footprint is visualised on the left side of Figure 2.8, and compared with the SAR footprint which is explained below.

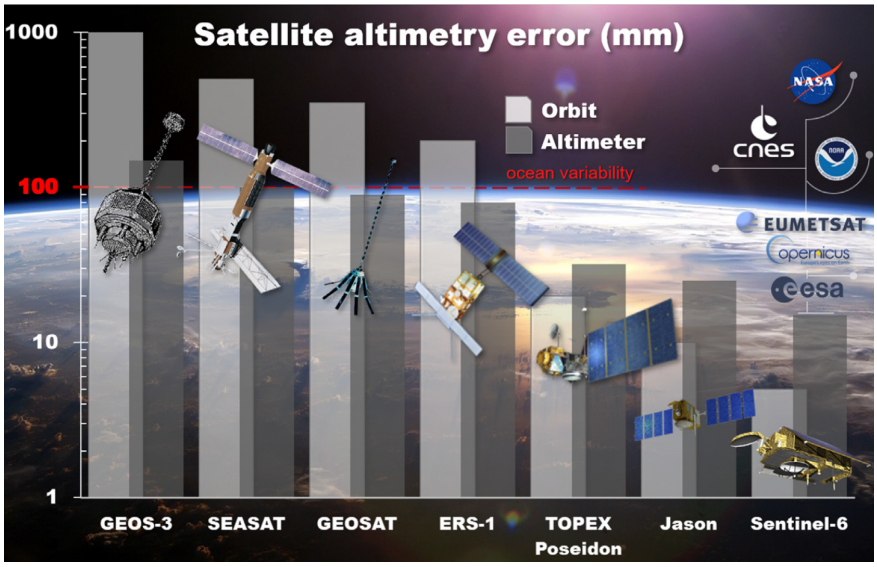

Figure 2.5: Changes of altimetry errors in time (light gray: radial orbit error, dark gray: instrumental error, including corrections, red: ocean variability) (Abdalla et al., 2021)

Synthetic Aperture Radar (SAR) SAR altimeters (also referred to in the literature as delay-Doppler altimeters) allow for an along-track resolution of up to 250 m for a Ku band altimeter (Raney, 1998). This is achieved by exploiting the Doppler effect caused by the movement of the surface scatter relative to the satellite in motion over that surface. Each target on the ground is observed multiple times by the radar as the satellite moves above it, this is because the consecutive pulses from different bursts/ looks of the real aperture radar keep the target within the radar beam (the geometry can be visualised in Figure 2.6).

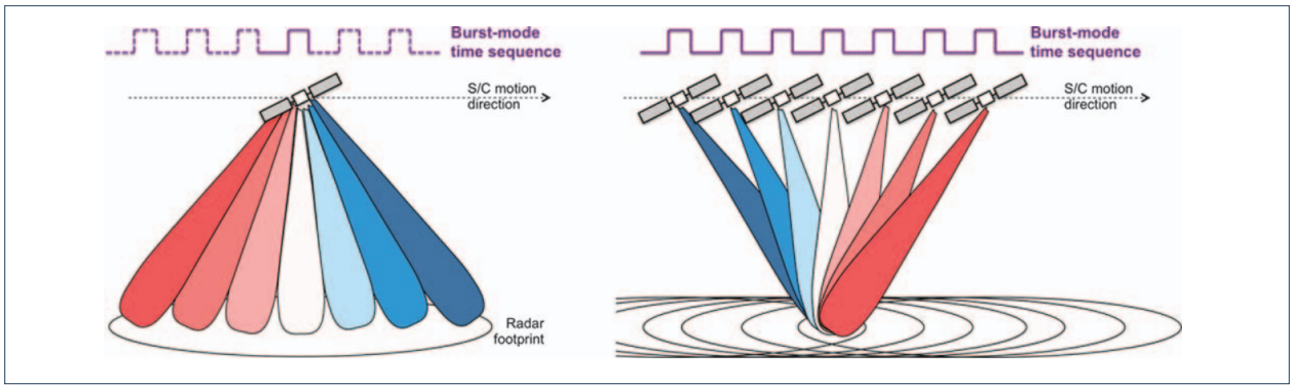

Figure 2.6: Blue and redshift of the Doppler beams/looks (Boy et al., 2016)

When the target is ahead of the pulses illuminating it, the reflected frequency is higher and vice versa when the target is behind the satellite. The beams/looks corresponding to each footprint section are then collected and corrected for the Doppler shift. This technique effectively allows us to ”synthesize” a large aperture by exploiting the motion of a physical antenna with a small aperture. The height measurement is therefore derived from all the signals collected along-track, rather than only the pulse-limited area, as is the case for LRM altimeters (where most of the power radiated is lost as it falls inside the antenna pattern, but outside of the pulse-limited area (Raney, 1998)).

The radar waveform and resolution

Radar altimeters are active remote sensing instruments: they send a radar pulse towards the surface of the Earth and receive the reflected signal, which is a power signal varying in intensity over time. The returned pulse/echo shape is defined as a waveform. It is a time-domain signal that represents the amplitude of the radar pulse as a function of time. The waveform is used to characterize the instrument’s performance and to extract information about the surface being observed (a typical waveform and its associated terminology is introduced in Figure 2.7). In radar altimeters operating over the ocean, such as Sentinel-6, the waveform shape is characterised by a power peak corresponding to the time instant where the signal hits the surface of the ocean. The signal after the peak remains quasi-constant for LRM altimeters (in Figure 2.8e, it can be seen that the surface area of the dispersion rings in the footprint is

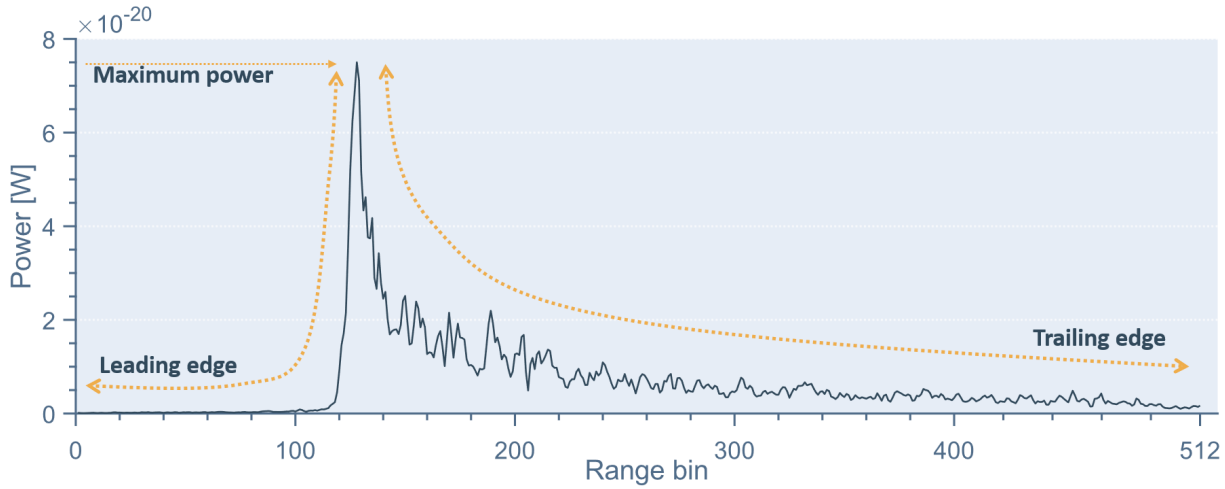

Figure 2.7: FFSAR waveform characteristics and dimensions: leading edge, point of maximum power and trailing edge. Waveform obtained from Sentinel-6 over the study area considered for this thesis

equal), while for SAR altimeters, the signal reflected decreases in time, in correspondence of the trailing edge (Figure 2.8f). The data is sampled by the altimeter in two dimensions: along-track and across-track. The distance between along-track measurements is determined by the along-track resolution (computed for FFSAR waveforms in Equation 2.7)

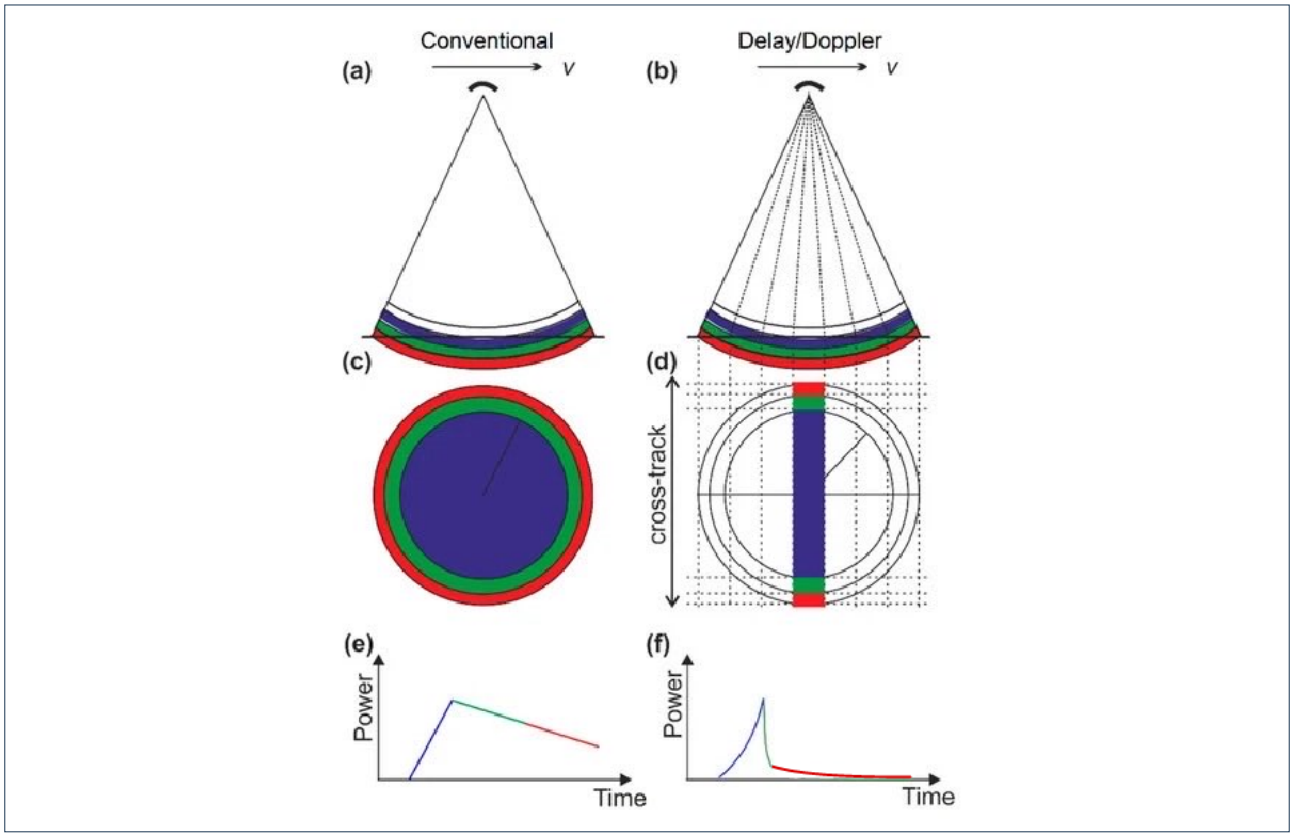

Figure 2.8: a,b: Geometry of pulses transmitted by conventional and SAR radar. c,d: Respective footprint size (colored area). e,f: Corresponding waveform shapes (Jiang et al., 2017)

Increase in cross-track resolution The cross-track resolution is determined by the distance between two range bins within a waveform, which is defined as the range bin width/ sampling distance δR_{sr} (ESA, 2023). As seen in Equation 2.5, range resolution is dependent on the instrument's bandwidth and is therefore a fixed value for a given payload. The range resolution determines the cross-track resolution for SAR and LRM instruments and it can be retrieved using the following equation (Cumming and Wong,

2005):

$$\delta R_{\mathrm{sr}} = 0.886 \frac{c}{2B} \tag{2.5}$$

where c is the speed of light and B the chirp bandwidth (as mentioned previously, the footprint is pulse-limited in the across-track dimension). For reference, the range resolution of Sentinel-6 is reported in Subsection 2.5.3. To quantify the ability of the instrument considered to differentiate two close targets on a surface, this slant range resolution is projected on the ground as described in Equation 2.6. The geometry considered is depicted in Figure 2.10. When considering the evolution of the signal reflection for SAR footprints (as presented in Figure 2.9), it is evident that as time passes, the resolution cell becomes smaller in the across-track direction, meaning that:

As one moves towards the trailing edge of a tail, the cross-track points are spaced closer together. This phenomenon results in the latter part of the waveform exhibiting a higher resolution

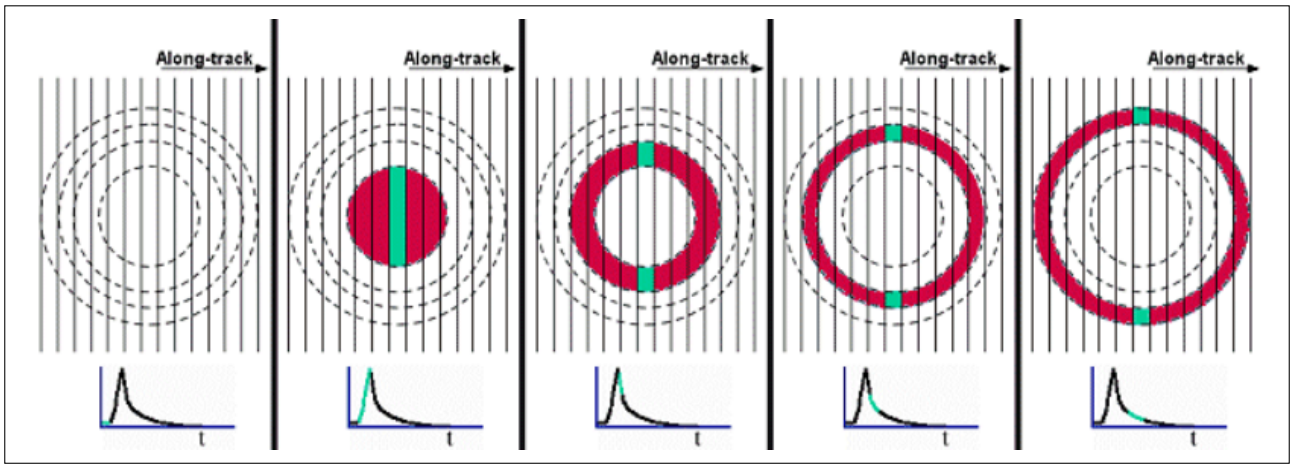

Figure 2.9: Increase in across-track resolution along the SAR waveform trailing edge (Rosmorduc et al., 2018)

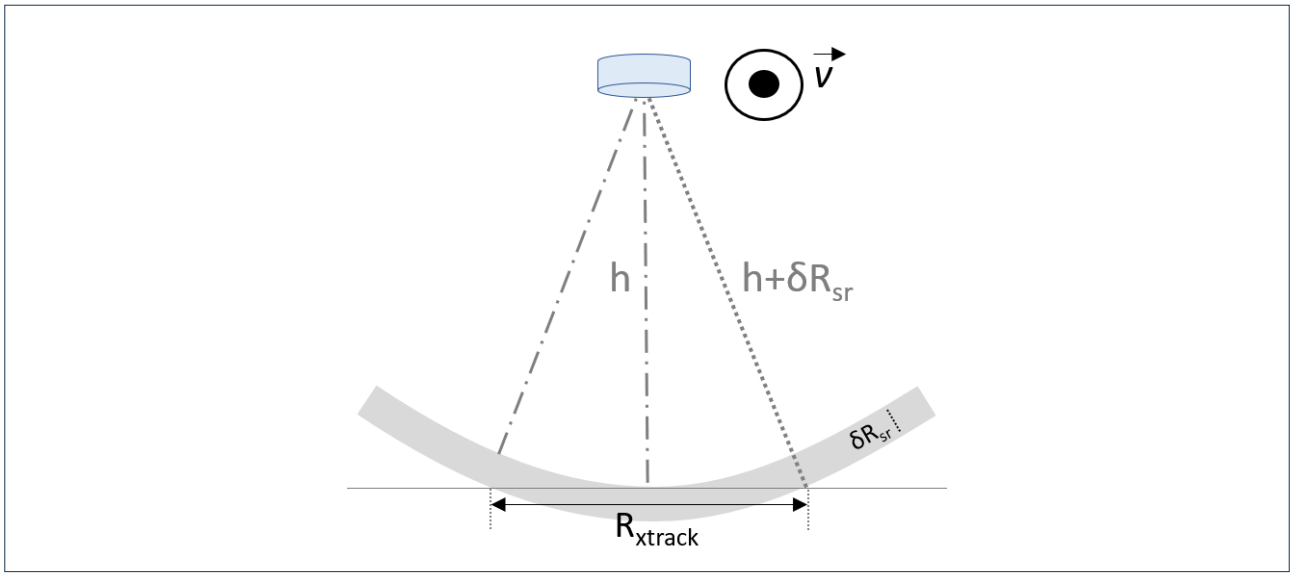

Figure 2.10: Pulse-limited geometry and range resolution, adapted from Jensen (1999a)

The horizontal distance l_{cross} between the scatterer at nadir and the range bin considered can be projected on the ground in across-track direction following Equation 2.6, as explained in (Altiparmaki et al., 2022).

$$l_{\mathrm{cross}} = \sqrt{\left(h + \left(n - n_{\mathrm{ref}}\right) \delta R_{\mathrm{sr}}\right)^2 - h^2} \tag{2.6}$$

where h is the satellite altitude, n is the range bin considered, n_{ref} the reference bin on the leading edge, dR the range sampling distance (see Equation 2.5). Once the waveforms are projected, they can be represented as shown in Figure 2.7 with the x axis values referring to their location across-track in meters. The way that projected waveforms are oriented with respect to the along-track direction for Sentinel-6 is clarified by Figure 2.11.

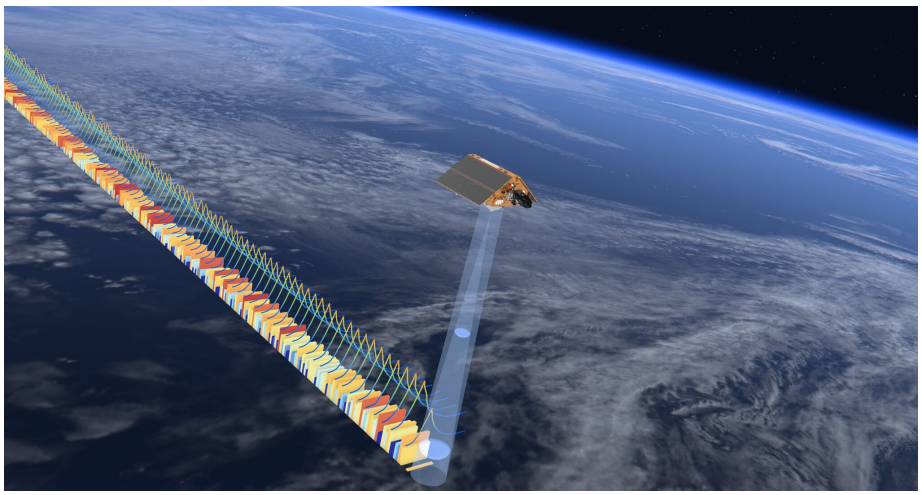

Figure 2.11: Sentinel-6 generating waveforms. Image Credits: ESA

Swell detection with SAR altimeters

Swell has never been observed using conventional altimeters as it was averaged out in the low resolution cells and therefore not detected. However, the higher resolution of SAR unfocused and fully focused processed data allows swell systems to interact with the altimeter signal and to effectively leave a trace in it (Altiparmaki et al., 2022). It has been shown in fact, that SAR waveforms are distorted by long period waves (such as swell and long wind waves) and, as a consequence, the retrieval of Significant Wave Height (SWH) is compromised (Aouf, 2015; Moreau et al., 2018).

The distortions due to the presence of swell have been found to mainly affect the trailing edge of the waveform (as noticeable in the oscillations seen in Figure 2.7), where characteristic undulations can be observed (a smoother signal would be otherwise expected) (Rieu et al., 2021).

Figure 2.12 shows how for conventional altimeters, both short and long ocean waves get averaged in the footprint while for SAR altimeters (right), the footprint in the along-track direction is similar or smaller in size compared to the longer ocean waves, which are therefore only partially imaged by SAR altimeters. The surface illuminated by the footprint therefore varies, leading to the power oscillations seen in Figure 2.7 and Figure 2.13. While the leading edge is also deformed by the presence of swell (Moreau et al., 2018), the oscillations are mostly visible in the tail of the waveform. This can be explained by the increased resolution in the last part of the waveform: the smaller the illuminated area, the higher the impact of long period waves on the waveform, as only a very small portion of them is imaged.

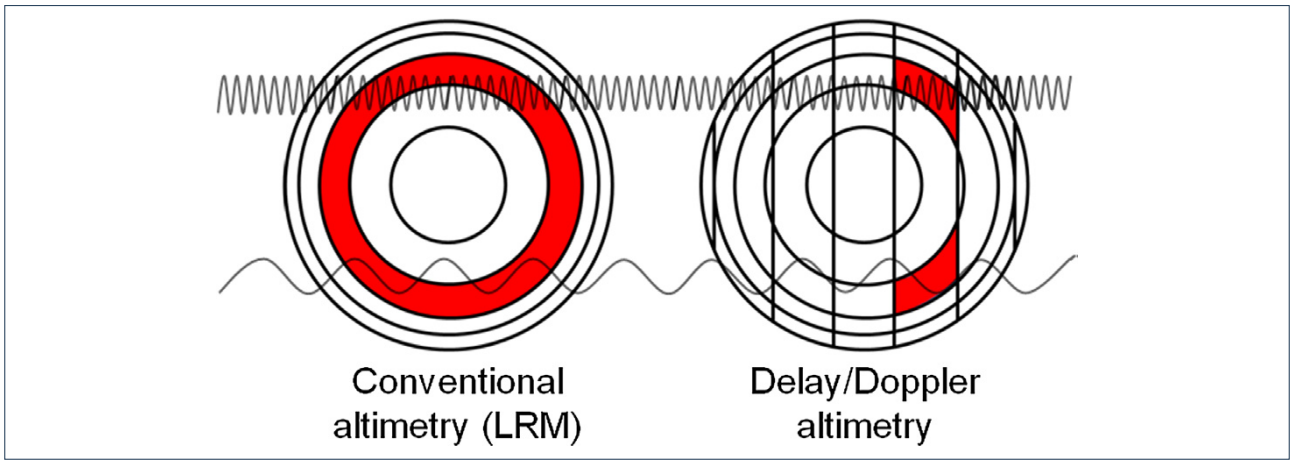

Figure 2.12: Swell imaging geometry in SAR altimeter waveforms (Moreau et al., 2018)

These distortions have been used by Altiparmaki et al. (2022) to retrieve a SAR spectra from FFSAR altimetry data, relying on the analytical relations between the modulations in the SAR spectra and the wave spectra defined by Hasselmann and Hasselmann (1991). The effect of truncating the trailing edge of the Sentinel-6 waveforms on swell parameter retrieval has not yet been investigated, and it will be explored in the following chapters as it is the main objective of this research.

Radargrams A common way to display altimetry data and combine echograms for a given satellite track and latitude interval, is to plot adjacent waveforms from Level 1b datasets as a function of latitude/ along-track distance and range (or cross-track projected distance). The result obtained is shown in Figure 2.13 for Sentinel-6 FFSAR echoes collected over an area in the Channel Islands of California. The leading edge of the waveform can be recognised as the yellow part of the plot, where the power is highest. Before that, no power is received (dark blue area), while the trailing edge of the wave returns a low power, featuring the oscillations due to swell described above. Taking the cross-section of the radargram at a given latitude returns the FFSAR waveform shape overlapped in white on the radargram.

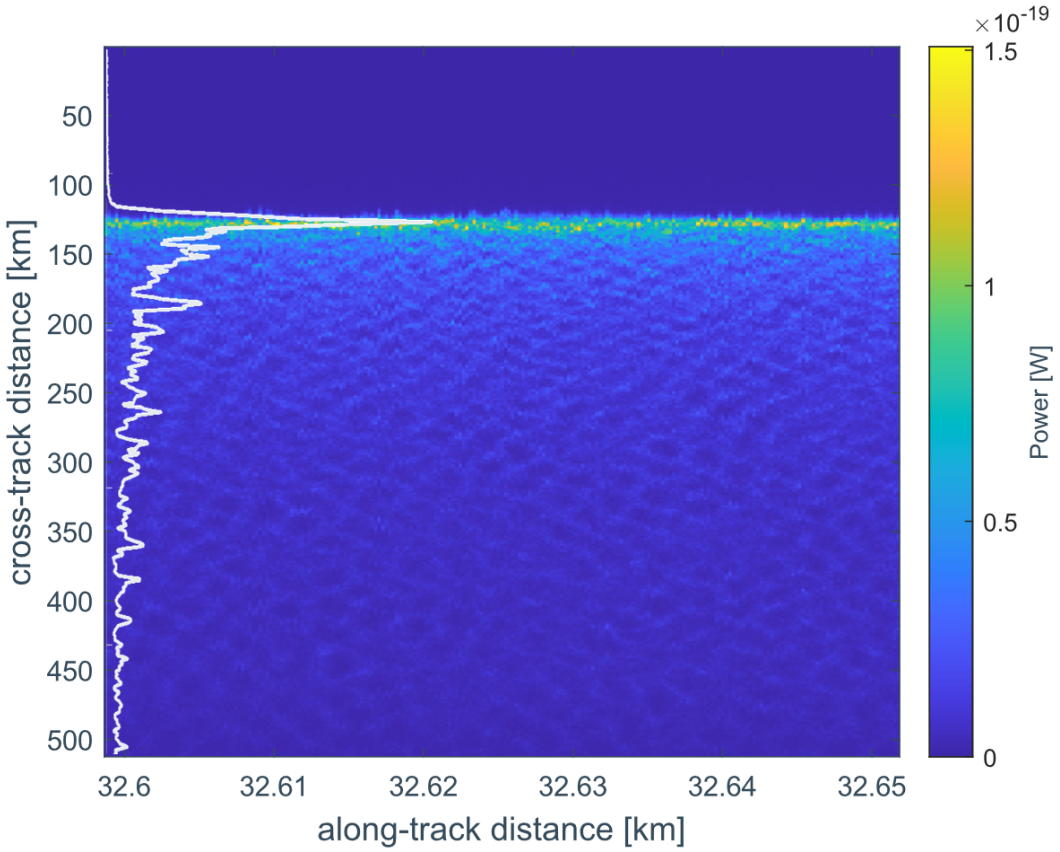

Figure 2.13: Example of FFSAR radargram retrieved using the processor by Earth Console and Sentinel-6 data collected by relative pass number 206 on 27.22.2021 over the specified latitude interval

FFSAR altimetry spectra and imaging mechanisms The projected radargram and resulting spectra shown in Figure 2.14 have been obtained starting from the L1B FFSAR radargram above through methodology proposed by Altiparmaki et al. (2022), with the steps illustrated in Section 3.3. The FFSAR spectra shows the normalised energy of the signal for each wave-number frequency component (along and cross-track) retrieved from the Fourier Transform of the projected radargram. Just like for spectra obtained from SAR imagers:

The imaging mechanisms for nadir-looking SAR instruments (altimeters) are highly non linear and there isn't a one to one relation with the ocean wave spectra

In this report therefore, the swell period T_s is derived from the FFSAR spectra as a *first estimate* of the peak period DPD measured by the buoy in presence of swell. Currently, there is no proposed closed-form expression to invert the FFSAR spectra from SAR altimeters into an ocean wave spectra, but the correlation functions proposed by Hasselmann and Hasselmann (1991) can be used as a starting point for the analysis and interpretation of the altimetry spectra.

The modulations to be considered when interpreting FFSAR altimetry spectra are therefore the same as those explained in Subsection 2.3.1 for SAR imagers spectra, however, as the main scattering system for nadir altimeters is specular scattering instead of Bragg scattering, the relative importance and effect of the RAR and SAR modulations are different than what seen before. In particular, to simplify the interpretation, the hydrodynamic modulation and tilt modulations can be ignored as they are much smaller than

range bunching for nadir-looking radars (Altiparmaki et al., 2022). Range bunching is maximal when the radar signal illuminates targets orthogonal to it and it is very non-linear as swell slopes are usually larger than the incident angle, while it is very small for waves travelling along-track (Altiparmaki et al., 2022). Lastly, Altiparmaki et al. (2022) also concluded based on simulations that range and velocity bunching have similar magnitudes, with range bunching dominating.

Multiple power peaks in Figure 2.14 are expected: an ambiguity of 180° is present just like in SAR imagery (Bao and Alpers, 1998). An additional peak is present in FFSAR spectra however: this causes the symmetry about the satellite azimuth (along-track travel direction) as the instrument is nadir looking and therefore signal from both sides of the track is considered. As explained in Subsection 2.3.1, specific processors allow for the removal of such ambiguity while the secondary peak is a characteristic of near-nadir instruments.

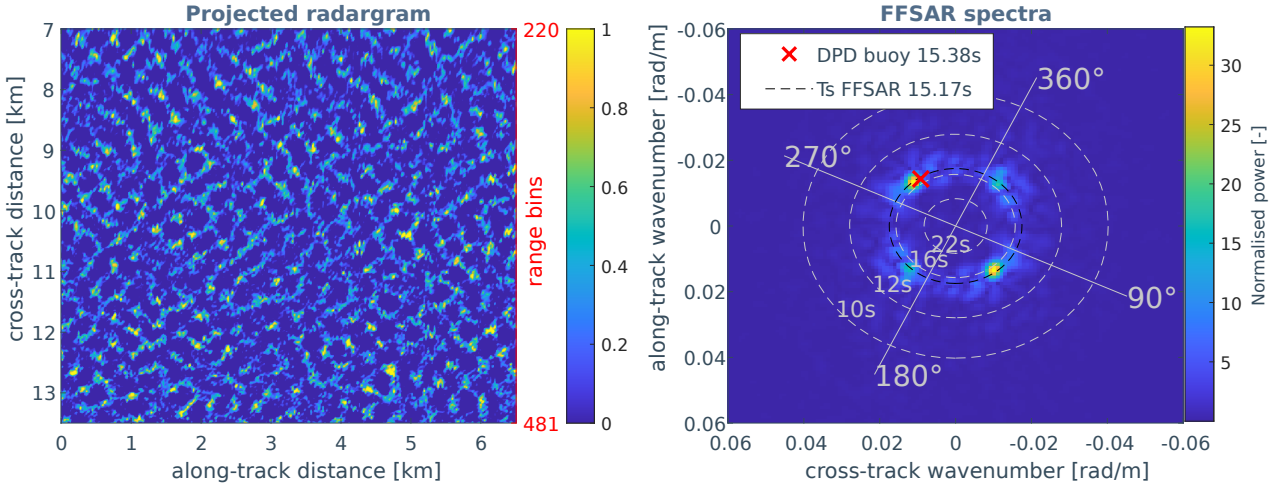

Figure 2.14: Example of normalised projected radargram and corresponding FFSAR spectra. Retrieved using the processor by Altiparmaki et al. (2022) and Sentinel-6 data collected by relative pass number 206 on 27.22.2021 with DPD the peak period retrieved by NDBC buoy 46219 and Ts the swell period estimated from the diagram. Isolines for the peak period of the wave spectra are over-imposed on the FFSAR spectra.

2.4. Fully focused SAR

Considering that the input data utilized in this study is derived from a FFSAR processor, this section will provide a comprehensive analysis of this particular processing mode.

Recently, a new type of SAR processing mode has been introduced. It was first described by Egido and Smith (2017) as Fully Focused SAR or FFSAR mode. This type of processing takes advantage of the phase stability of the radar pulses emitted in each burst (Centre National d'Etudes Spatiales, 2017): the summation of coherent pulses gets thereby extended to the entire synthetic aperture rather than being limited by a number of successive pulses/ bursts, like in the case of D/D processing (Guccione et al., 2018). This inter-burst integration can be therefore performed along an integration time which corresponds roughly to the time during which a scatterer on the surface is illuminated ($2.5\ s$). With respect to unfocused SAR (UFSAR), the resolution is significantly increased along-track and it goes down to its theoretical limit of ~0.5 m (half antenna length, as derived from Equation 2.7) (Egido and Smith, 2017). The across-track resolution remains the same as for SAR and LRM modes as it is pulse width (bandwidth) limited. The FFSAR footprint is shown in Figure 2.15, where the asymmetry of the footprint becomes evident (a higher resolution is achieved only along-track).

FFSAR offers another advantage, which is the increased Effective Number of Looks (ENL). This is accomplished thanks to the increase in the amount of samples that can be multi-looked compared to unfocused SAR (Egido and Smith, 2017) (for more information about multi-looking, see the paragraph below about FFSAR processing). The ENL can in fact be described as the number of independent observations obtained by the radar from a distributed target per unit of time (Egido et al., 2021). Egido and Smith (2017) found the FFSAR ENL to be double of the delay Doppler one for a study case on Cryosat-2 (CS2). The higher ENL available in FFSAR data-sets has practical benefits as it reduces noise (Raney, 2013), resulting in more accurate estimation of geophysical parameters, particularly over ice and open ocean. The noise

level on the geophysical estimates from Sentinel-3 (S3) data collected over the open ocean was found to be respectively reduced by a factor ~√2 (Rieu et al., 2018).

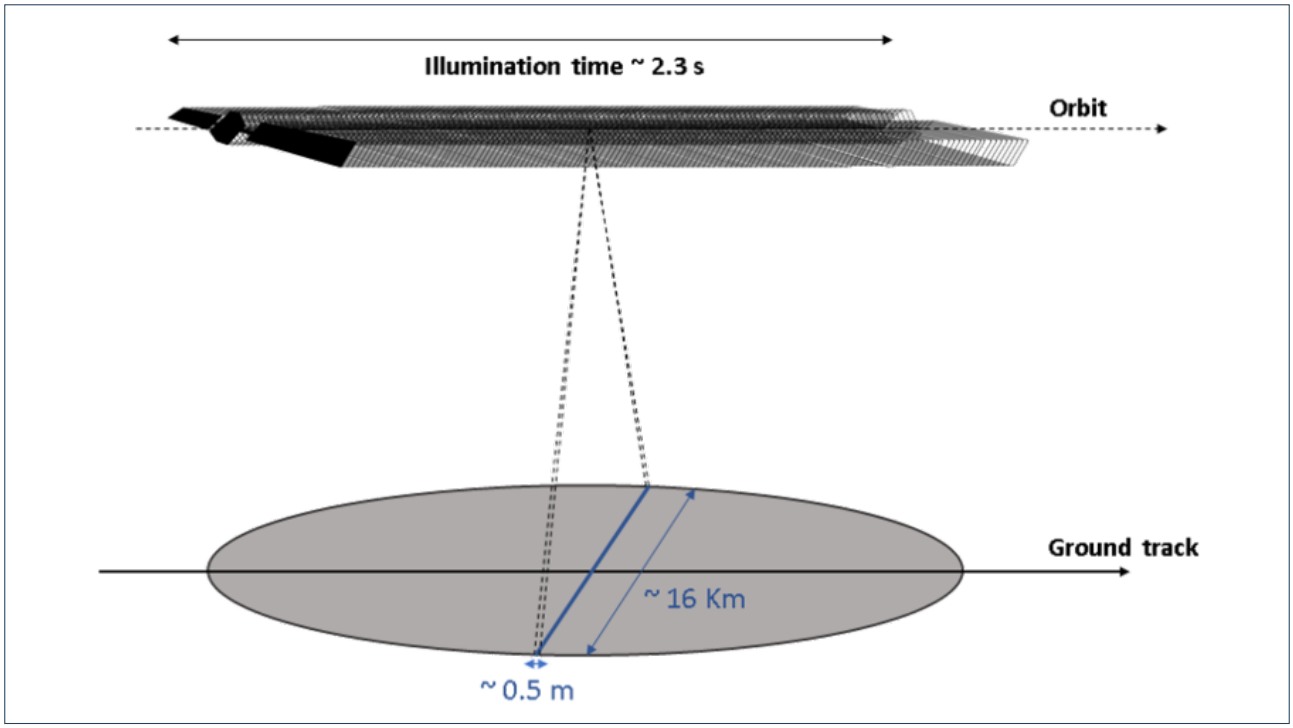

Figure 2.15: FFSAR footprint (blue), LRM footprint (grey) for CryoSat 2 (Centre National d'Etudes Spatiales, 2017)

FFSAR along and across-track resolution

The maximum along-track resolution obtained with FFSAR processing can be retrieved from the 2D Point Target Response and corresponds to the maximum illumination period (T_{SAR}). It can be formulated as follows (Egido and Smith, 2017):

$$\delta R_{atrack} = 0.886 \frac{cR_0}{2 f_c v_s T_{SAR}} \tag{2.7}$$

where R_0 is the minimum range to the specular point, f_c the carrier frequency, v_s the satellite velocity. The maximum illumination period itself is a function of the antenna beamwidth Θ_a:

$$T_{SAR} = \frac{\Theta_a R_0}{v_g} \tag{2.8}$$

where v_g is the speed of the satellite projected on the ground ($v_g = v_s / \frac{R_E+h}{R_E}$ with R_E Earth's radius) and $\Theta_a \simeq 0.886\lambda / L_a$ can be assumed for a large antenna (Egido and Smith, 2017),with L_a the antenna length. This leads to:

$$T_{SAR} = 0.886 \frac{\lambda R_0 \frac{R_E+h}{R_E}}{L_a v_s} \tag{2.9}$$

Substituting Equation 2.9 into Equation 2.7 and considering that $h << R_E$ the along-track resolution can be rewritten as:

$$\delta R_{atrack} \simeq \frac{L_a}{2} \tag{2.10}$$

Half of the antenna length is therefore the highest theoretical resolution achievable with a SAR altimeter in space by applying FFSAR processing to the signal. For context, Cryosat 2 antenna is approximately 1m long.

2.4.1. FFSAR processing, multi-looking and available processors

The processing steps necessary to obtain a FFSAR L1B product from raw (L1A) mission data are summarised below and are described in more detail in (Egido and Smith, 2017).

1. Range Cell Migration Correction: the pulses are aligned with respect to the focusing point and the range measurement is thereby corrected for phase shifts inferred by moving targets.

2. Range Compression: the pulses are compressed in range direction to account for the presence of echoes from multiple targets in the signal.
3. Residual Video Phase correction: accounts for secondary effects that cause distortions in the phase.
4. Relative Range Phase correction: entails the removal of the range phase, which is the dominant phase term, accounting for phase delays on echoes originating from the same target. This is the key term necessary to improve the along-track resolution.
5. Coherent combination of echoes: all the echoes collected for a target over the duration of its illumination have been aligned in range and phase. They can therefore be summed over the integration time to obtain the FFSAR single-look complex (SLC) waveform.

As an additional step to create a Level 1b product, the complex SLC waveforms are multi-looked. Multi-looking is a process during which the single-look echoes from beams targeting the same surface are averaged for successive bursts. The aim of this approach is to mitigate the impact of speckle noise-induced power fluctuations in the signal (Wingham et al., 2006), thereby enhancing the Signal to Noise Ratio (SNR). During multi-looking, the SLC waveforms from FFSAR are combined by averaging them at the posting rate of L1B products (such as 60Hz, 100Hz, 140Hz, 200Hz) (Schlembach et al., 2023). A higher posting rate requires greater computational power and storage capacity, yet research has demonstrated that it leads to an increase in the ENL, which reduces measurement noise and improves the accuracy of geophysical parameter estimation (Egido et al., 2021).

Subsequent to the publication of this novel technique, several investigations pertaining to FFSAR have been documented in the scientific literature. These resulted in the development of various processors. To the knowledge of the author, the principal FFSAR processor based on the back-projection algorithm described by Egido and Smith (2017) is the Standalone Multimission Altimetry Processor (SMAP) developed by Collecte Localisation Satellites (CLS) for Sentinel-3. This processor was used for Cryosat 2 by Kleinherenbrink et al. (2020), adapted for the study of inland waters and later employed also by Schlembach et al. (2023) for a coastal application. Most recently Ehlers et al. (2023) continued the development and optimisation of the algorithm and successfully retracked the FFSAR waveforms. An alternative method was proposed by Guccione et al. (2018) to address the computational complexity associated with FFSAR processing. Guccione's approach focused on modifying the Omega-Kappa algorithm, which is a focusing technique in the 2D transformed frequency domain. This methodology is exploited by the AREALT-FF1 processor by Aresys (Scagliola et al., 2021), which is being employed for the first time on Sentinel-6 data for this thesis, and which was extensively used by Altiparmaki et al. (2022) on Sentinel-3 data to set the ground for potential retrieval of swell wave parameters from (FFSAR) altimetry data.

2.4.2. Applications of FFSAR for Cryosat 2, Sentinel 3 and

FFSAR processing has been already employed for studies involving Cryosat-2, Sentinel-3 and . CS2 and S3 operate in closed-burst mode (lacunar sampling). This results in a sparse sampling pattern, which causes sidelobes to appear in the response along the track direction. The ENL is in turn lowered as a correlation is introduced between adjacent looks (Egido and Smith, 2017). Sidelobes in the case of CS2 and S3 appear every ~90 m along-track (Ehlers et al., 2023). The sidelobes can be visualised in Figure 2.17 for an inland water FFSAR application explored by Rieu et al. (2018) for S3, where it becomes clear that for bigger targets, the signal replicas could interfere among each other. As Egido and Smith (2017) explained on the other hand, S6 is best suited for fully focused processing as it operates in open-burst/ interleaved (ILM) mode, meaning that the signal is received in-between transmission phases (Donlon et al., 2021). The concept is visualised in Figure 2.16 The target replicas are minor and occur every ~300 m in the case of (Ehlers et al., 2023).

Fully focused processing can meet the demands of various applications where smaller scale features need to be separated from other scatterers in an heterogeneous surface (Egido and Smith, 2017). This has significant implications for observations in proximity of the coast, where Schlembach et al. (2023) found an increase of 29% in precision of geophysical parameter retrieval for FFSAR compared to unfocused SAR, as the signal from the land does not get averaged in the resolution cell and therefore does not contaminate the waveforms as much. Other targets with a significant potential for retrieving high quality observations from FFSAR data are for instance inland water bodies, ice sheets and open ocean features that can not be recognized using unfocused SAR. This last case was recently explored by Altiparmaki et al. (2022), who showed the potential for retrieval of swell wave parameters from FFSAR data.

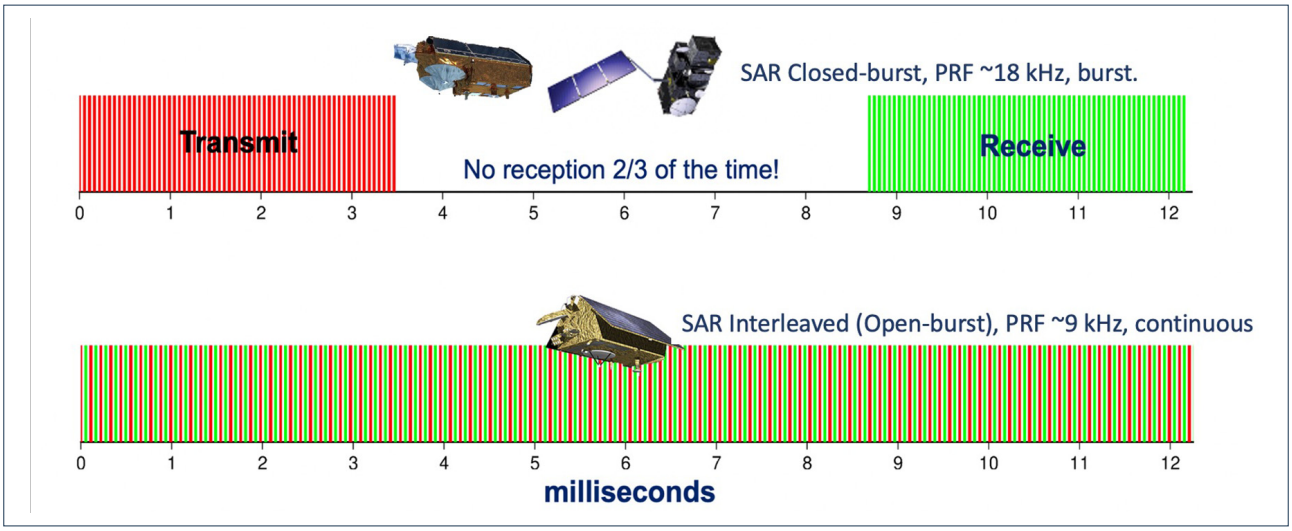

Figure 2.16: Closed (S3, CS2) vs open burst mode (S6) (Donlon et al., 2021)

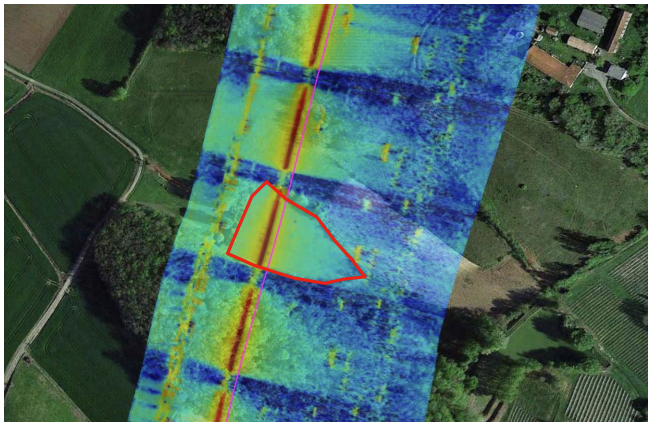

Figure 2.17: Signal aliases in S3 FFSAR data for a ~70m wide pond (cross-track extension is not realistic) (Rieu et al., 2018)

2.5. Sentinel-6

The Sentinel-6 Michael Freilich, previously known as Sentinel-6/Jason-CS (Jason Continuity of Service), is the latest radar altimetry mission currently in operation. It was launched in November 2020 with the primary aim of expanding the sea level data record beyond 2030 while ensuring consistency with the sea level measurements obtained by the previous TOPEX/Poseidon missions. Similar to its forerunners, Sentinel-6 is an integral part of the european Copernicus Programme for Earth Observation.

2.5.1. Mission key information

The Sentinel-6 has been designed primarily as an observational platform for oceanography, meteorology (with a focus on ocean and weather forecasting), and hydrology. Its main mission objective is to ensure continuity for the Copernicus service by generating high-quality, dependable data in a timely manner, with minimal downtime. This objective is aimed at maintaining the reliability and accuracy of the Copernicus service, which is essential for a range of scientific and societal applications. Reference (ESA, 2021) provides additional details on these objectives. The Copernicus Sentinel-6 is a dual-satellite system, consisting of two identical satellites that are launched in sequence. Jason-CS A was launched in 2020, while Jason-CS B is scheduled to be launched in 2026. The primary payload of Sentinel6 is the Poseidon4 (P4) altimeter. In Table 2.1, the characteristics of Sentinel-6 which are of relevance for this thesis are reported (Donlon et al., 2021; Observing Systems Capability Analysis and Review Tool, 2021; Scharroo et al., 2016).

Table 2.1: Mission characteristics of Sentinel-6

Parameter	Value
Inclination	66.039 °
Reference altitude (equatorial)	1336 km
Nodal period	6745.72 s
Repeat cycle	9.9156 days
Number of orbits per cycle	127
Ground track separation at equator	315 km
Orbital velocity	7.2 kms^{-1}
Ground track velocity	5.8 kms^{-1}
On-board data storage	576 Gbit
SAR along-track resolution	300 m
Pulse Repetition Frequency (PRF)	9 KHz

2.5.2. Poseidon-4 altimeter

This main instrument is a SAR altimeter (visualised in Figure 2.18), operating in the Ku and C band: Poseidon-4 (P4). The SAR mode operates in the Ku band (central frequency: 13.575 GHz, total bandwidth: 320 MHz) (Symbios, 2022). SAR data is provided with an along-track resolution of about 300 m (Kramer, 2022). The primary innovative feature of this altimeter is its capability to operate both the SAR and conventional LRM modes simultaneously, on a global scale. This is possible thanks to the ILM mode explained in Section 2.4.

Figure 2.18: The Poseidon-4 altimeter antenna, on the bottom of the satellite. Image Credits: NASA JPL

2.5.3. The Sentinel-6 waveforms and the RMC algorithm

Poseidon-4's global coverage leads to the production of a large volume of data which has to be downlinked in a short amount of time to one of the two ground stations. To reduce the data volume, an on-board Range Migration Correction (RMC) algorithm is applied on board of Sentinel-6 (Phalippou and Demeestere, 2013; Phalippou et al., 2012). This algorithm aligns the bursts in range direction to correct for range migration (as described also in Section 2.4 for FFSAR processing) and then proceeds to truncate the number of samples in the waveform as depicted in Figure 2.19a. The resulting RMC waveform is therefore containing signal only in its first half. raw waveforms are still generated by the mission, but they are collected only over calibration areas. The difference between RMC and raw waveforms is clarified by Figure 2.19b.

The RMC algorithm reduces the data rate by a factor of two (Donlon et al., 2021) while keeping the first half of the waveform intact.

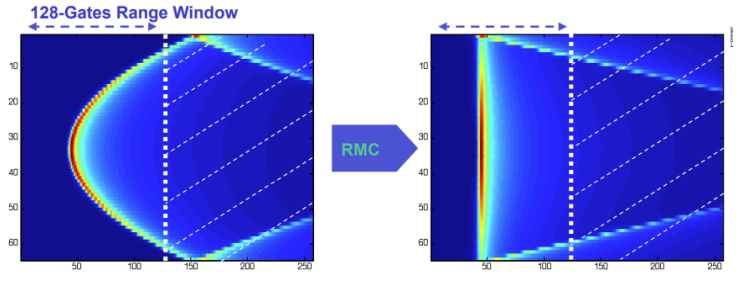

(a) Fast Fourier Transform of a raw burst power, before (left) and after (right) RMC processing. High power is a red and low power (~thermal noise) is dark blue. Cutting of the SAR waveforms is performed after the burst alignment. (Phalippou et al., 2012)

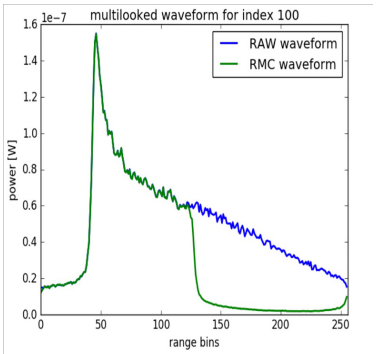

(b) Sentinel'6 unfocused SAR RMC waveform compared to raw waveform (Donlon et al., 2021)

Figure 2.19: RMC waveform creation and comparison with raw echo

Waveform processing Sentinel-6 waveforms have 256 range bins, with a theoretical range bin resolution of 0.47 m (Donlon et al., 2021) which is dependent on the instrument's bandwidth of 320 MHz (see Equation 2.5). The waveforms are however sampled at 395 MHz by the altimeter clock, leading to a range bin width (distance between samples) of 0.37948 m (exact value extracted from private communication, Fornari (ESA), 2023). The algorithm aligns these bins in the range direction to compensate for the migration of the target off-nadir described in Section 2.4. The truncation process removes 128 bins from the trailing edge leaving the RMC waveform with 128 bins, which are sent to the ground where the on-board processing is reversed using the Ground Processor Prototype (GPP) designed by ESA and Thales Alenia Space (Picot et al., 2018). The GPP output is a SAR RMC waveform in the same domain and format as raw waveforms: this allows to pass it as an input to the conventional SAR processing chain, although the data contained in the trailing edge of the original waveform cannot be retrieved. During on-ground processing, zero-padding is applied to the RMC and raw waveforms. This is a technique that doubles the range sampling rate of the waveform (Dinardo et al., 2018; Jensen, 1999b) and halves the range sampling distance/ range bin width which then becomes 0.1897 m (0.37948/2). It is especially convenient to apply zero-padding to improve parameter retrieval in the case of specular surfaces, where the leading edge of the waveform is sparsely sampled (S3-MPC, 2022). For Sentinel-6, zero-padding is applied to obtain the Level 1 product (EUMETSAT, 2021). The range bins available become 512 (in the case of RMC, only the first 256 contain signal, as seen in Figure 2.20).

Operating mode The members of the Sentinel-6 Validation Team recommended in their latest meeting in July 2022 to proceed to operate the satellite with mode mask F to provide maximum coverage of inland waters with high-resolution data (Scharroo et al., 2022). This mode mask activates the "LRMC" mode collecting LRM& SAR RMC data for the open oceans as well as for the coastal areas and land, while over the calibration areas, it activates the "LX" mode which collects LRM and SAR raw data. The altimeter generates the following data rates: (Kuschnerus et al., 2018):

- 0.18 Mbit/s for LRM data
- 19 Mbit/s of SAR RMC data
- 37.7 Mbit/s of SAR raw data

Taking an example orbit that does not fly over calibration areas, for the orbital period reported in Table 2.1, the LRMC mode would produce around 130 Gbit of data, while for the LX mode, the data accumulated in one pass would reach ~255 Gbit. The two-fold increase in data volume necessary to keep raw waveforms would put stringent requirements on data storage, this is why the LRMC mode was preferred. Raw data is therefore currently collected only over calibration sites. In Figure 2.20, the difference between raw and RMC waveforms collected over the area of interest (see Section 3.1) is explained.

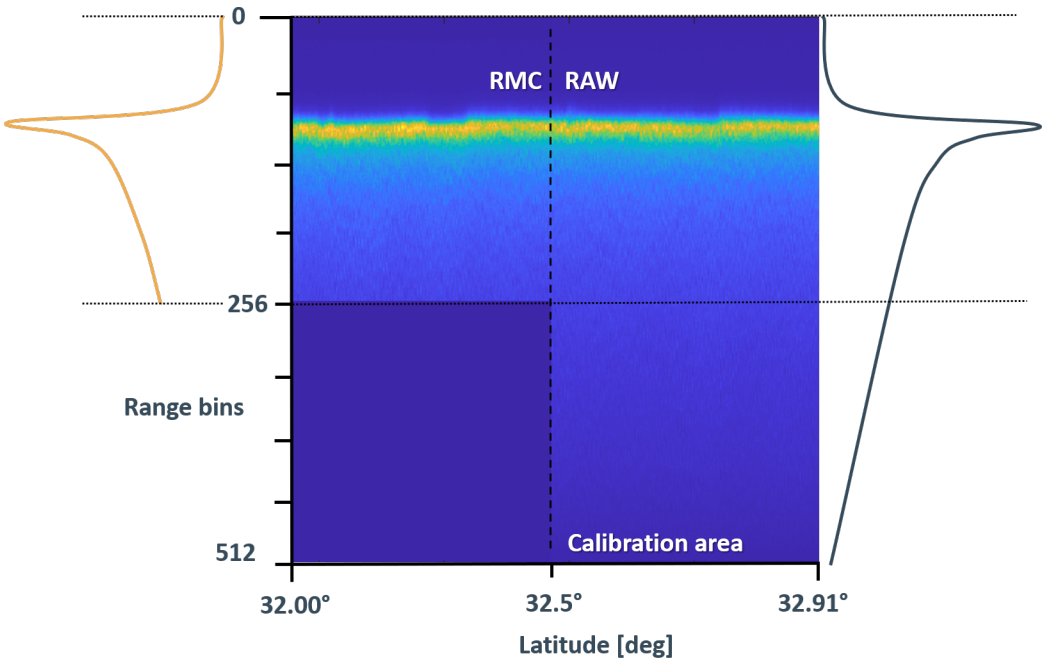

Figure 2.20: Unfocused radargram of Eumetsat L1B raw and RMC waveforms collected over the study area. On the side: the radargram vertical cross-section/ waveforms for the RMC portion (left) and the raw portion (right)

3

Data and Methods

In this chapter, the steps taken to collect the satellite raw and RMC data, process it and compare it to the validation dataset are explained. These consist in the identification of an area of interest, explained in Section 3.1, the collection of raw and RMC FFSAR waveforms from the applicable satellite passes (Section 3.2), the explanation of how the swell period was estimated from FFSAR spectra seen in Section 3.3 and finally the description of the buoy dataset used for validation and the choice of performance metrics in Section 3.4 and Section 3.5.

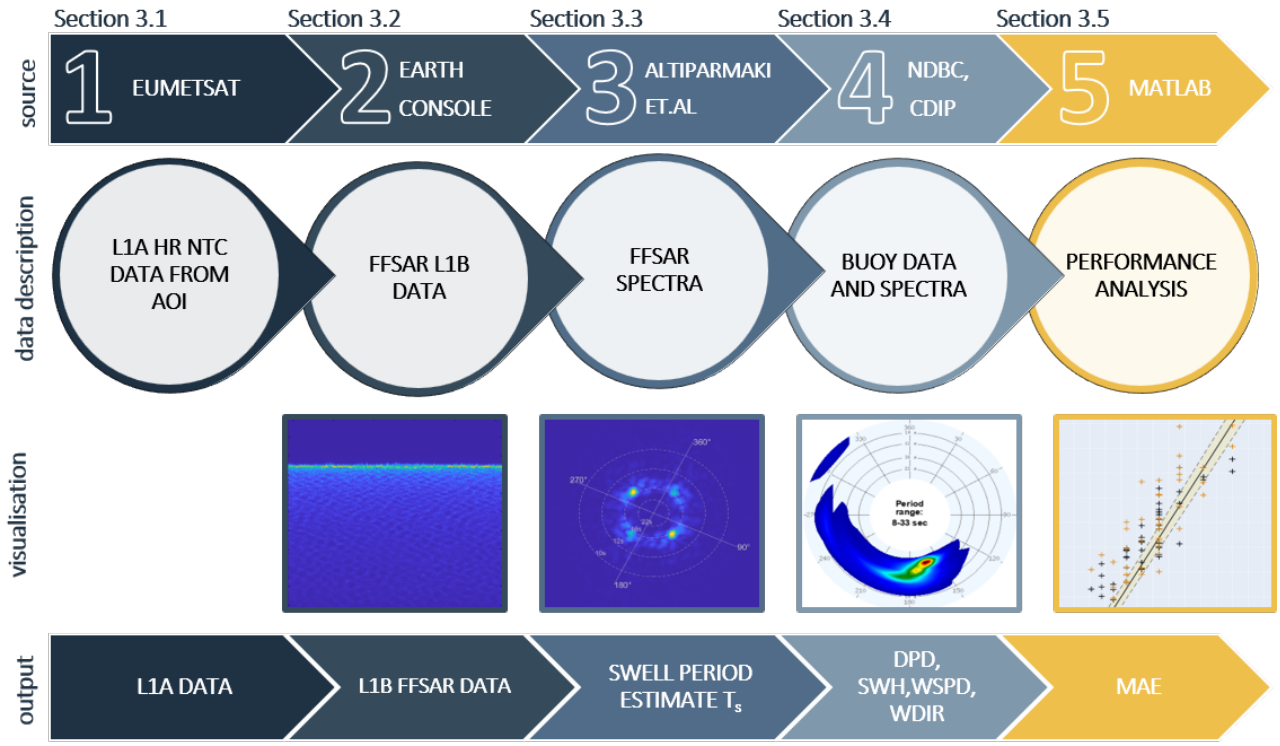

Figure 3.1: Description of the process and methodology. Satellite data acquisition (1), FFSAR processing (2), FFSAR spectra generation (3), buoy data acquisition (4) and finally performance analysis (5). On the top: are tools/ sources used for the data retrieval/ processing, middle: is the output of the considered step and data visualisation, and the bottom: are parameters retrieved for each step. *Note the difference between RMC (half waveform) and raw (full-waveform) sections of the radargrams in the bottom left of the diagram.*

The approach to the performance analysis and its main steps are visualised in Figure 3.1. They can be summarised as follows:

1. **Satellite data acquisition:** Once the area of interest was chosen to ensure the collection of both raw and RMC waveforms, Level-1A (L1A) High Resolution (HR) Non-Time Critical (NTC) data was retrieved for the chosen tracks from the Eumetsat data centre.
2. **FFSAR processing:** The L1A data was then processed by Earth Console to the Level-1B (L1B) FFSAR product, which can be visualised as a radargram for each pass.

3. **FFSAR spectra generation:** The processor provided by Altiparmaki et al. (2022) was used to obtain the FFSAR spectra corresponding to the raw and RMC L1B data and retrieve a first guess for the swell wave period.
4. **Buoy data acquisition:** The relevant buoy data was retrieved from the NDBC and CDIP for the epochs corresponding to the satellite observations.
5. **Performance analysis:** The swell period retrieved from the FFSAR spectra for both raw and RMC was compared with the peak period from the buoy spectra.

In the flowchart, it is highlighted how the main performance parameter: the peak period DPD, is retrieved from buoy data (for passes where the swell is detected) together with other parameters that will support the analysis (such as wave height SWH, wind direction WDIR and wind speed WSPD). A first guess of the swell period T_s is then retrieved from satellite data to set the ground for the performance analysis. Only satellite data collected over days where the swell was recorded was considered, allowing a comparison with the wave period measured by the buoys on said dates and resulting in an analysis of the relative performance of raw and RMC FFSAR data in estimating swell period (see Chapter 4 for the results).

3.1. Satellite data acquisition and description of the study area

As the prime objective of this thesis is to compare the performance of using raw versus RMC data sets for swell parameter retrieval, the choice of an appropriate study area was fundamental to ensure that the satellite data selected featured the presence of both types of waveforms. Due to storage limitations, the simultaneous production of raw and RMC data was performed only for 3 cycles (25-27) during the mission commissioning phase to understand the differences between LRM, raw and RMC-generated data. Generating RMC and raw data at the same time produces three times more data as the currently used LRMC mode (as can quickly be computed with the data rates in Section 2.5). The data from these three cycles is not publicly accessible at the moment, therefore, the following assumption was made:

The selection of raw and RMC waveforms that are adjacent (subsequently generated) on the same satellite track can be suitable to assess their potential of swell parameter retrieval, as long as the ocean wave properties are conserved within the considered ground-track segment.

This assumption is supported by the following reasoning: Sentinel-6 crosses the AOI shown in Figure 3.2 with a ground track velocity of 5.8 km/s (see Table 2.1). This entails a data collection interval of 17 seconds for segments 1 and 2, meaning that the satellite will fly over both raw and RMC collection areas at this time. From Equation 2.4, it can be calculated that even a very fast swell travelling at ~ 40 m/ s would only cover 680 m of the 100 km flown over by the satellite in 17 seconds. It can therefore be safely said that the period of a swell system crossing the satellite track at a given time will not vary between the raw and RMC sections. Furthermore, the validation data used (CDIP buoy 46219) provides two-period measurements per hour, averaged over 26.6 minutes (see Table 3.4): the effect of geophysical parameters that could change over 17 seconds and influence the swell period would thereby get averaged in the buoy measurement anyways. This decision affected in some cases the quality of the retrieved data, which suffered from the presence of a zone of mode-transition, as explained in Chapter 4.

As motivated in Section 2.5, raw data is produced only over calibration areas. This significantly limited the available study areas to the calibration areas used for the Sentinel-6 mission:

- **Ariege:** Continental calibration area in France.
- **Senetosa:** Calibration area in the central Mediterranean.
- **Gavdos:** Calibration area in the eastern Mediterranean, covering the western part of Crete.
- **Bass strait:** Oceanic calibration area in the Bass Strait (between Tasmania and Australia).
- **Channel Islands of California:** Oceanic calibration area in the South-West of California.

To select the study area, the research question (reported here again for reference) was taken as a basis to derive a series of requirements, listed below.

Does the truncation of waveforms performed by the **RMC** algorithm on board of **Sentinel-6** affect the potential of retrieving **swell** wave parameters from FFSAR spectra?

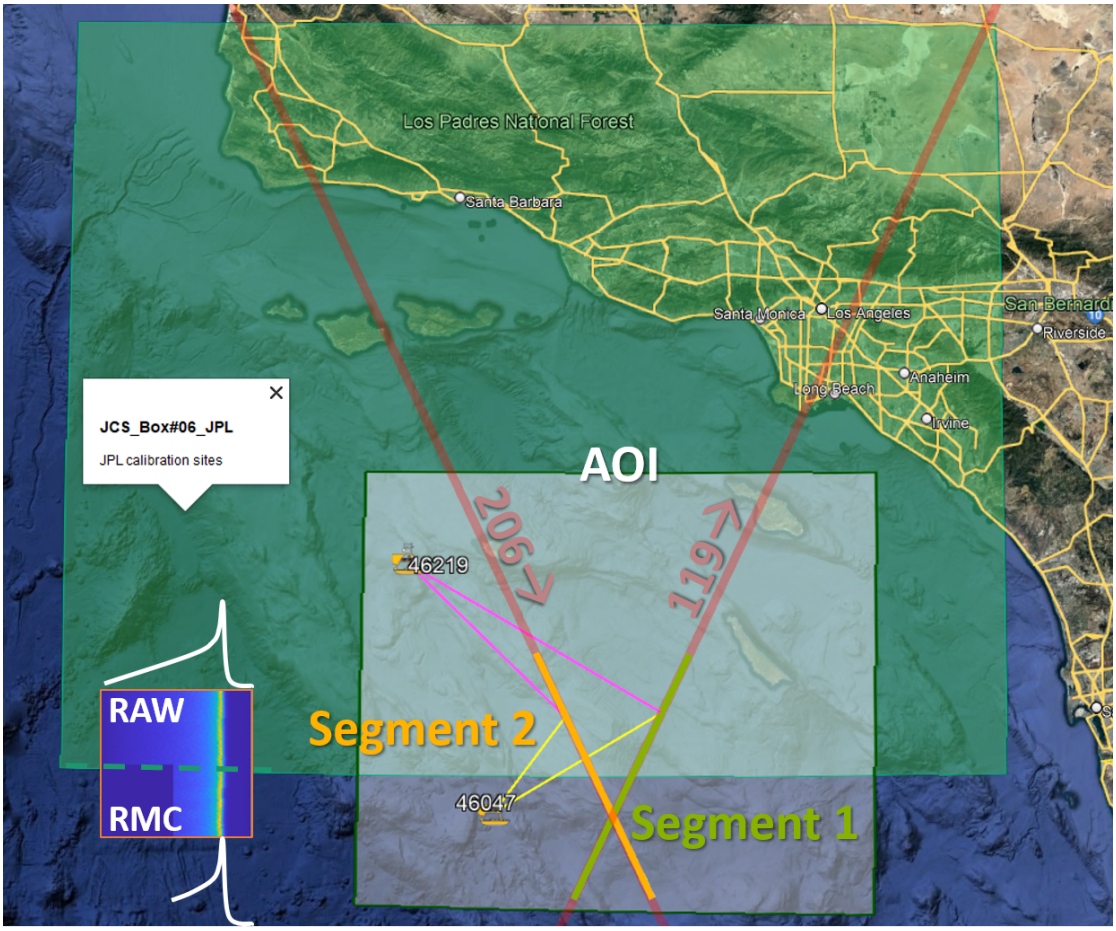

Figure 3.2: Calibration site (green); Area of Interest (white); ground tracks of passes 119, 206 (red); selected track segments 1,2 (orange, green); reference buoys 46047, 46219 (NDBC and CDIP buoy network) and their distances to the midpoint of the segments (yellow, pink)

- **R1:** The area should be crossed by **Sentinel-6** satellite tracks.
- **R2: raw and RMC** data should be available in the area.
- **R3: Swell** should be present in the area.
- **R4:** Buoys measuring wave period and energy should be active in the area to provide validation data.
- **R5:** The buoy measuring time should be similar to the satellite pass time above the area.
- **R6:** Buoys should be sufficiently close to the satellite tracks (to minimize the change in wave parameters as the waves disperse).
- **R7:** The water depth in the study area should ensure for deep water conditions are maintained (Equation 2.1), to preserve the swell wave parameters.

The area of interest that was chosen intersects the calibration area in the Channel Islands of California and can be visualised in Figure 3.2, while the selected satellite data segments are described in Table 3.1. The selection of this calibration area was based mainly on **R3** which could be met only by the two calibration areas located in open oceanic waters: the Bass Strait and Channel Islands areas. As seen in Figure 3.3 the Channel Islands area is exposed to swell generated by storms in the North-West and South-East Pacific, while the Bass strait is more shielded from swell overall and exposed only to the swell from one generation area in the South of Australia (this becomes clear when watching the animated swell models in Collecte Localisation Satellites (2023)).

The selected AOI is crossed by tracks with relative pass numbers 119 and 206 (relative orbit numbers 059 and 103), ascending and descending respectively; this satisfies **R1**.
R2 is guaranteed by the choice of using satellite segments crossing over calibration sites, where raw data is produced by definition (see Subsection 2.5.3). The calibration area extends in the latitude interval 32.5°-35°, therefore by selecting segments in the latitude interval 32.00° -32.91°, the collection of RMC data is ensured over the 32.00° -32.5° interval and of the raw data over the 32.5°-32.91° interval (see

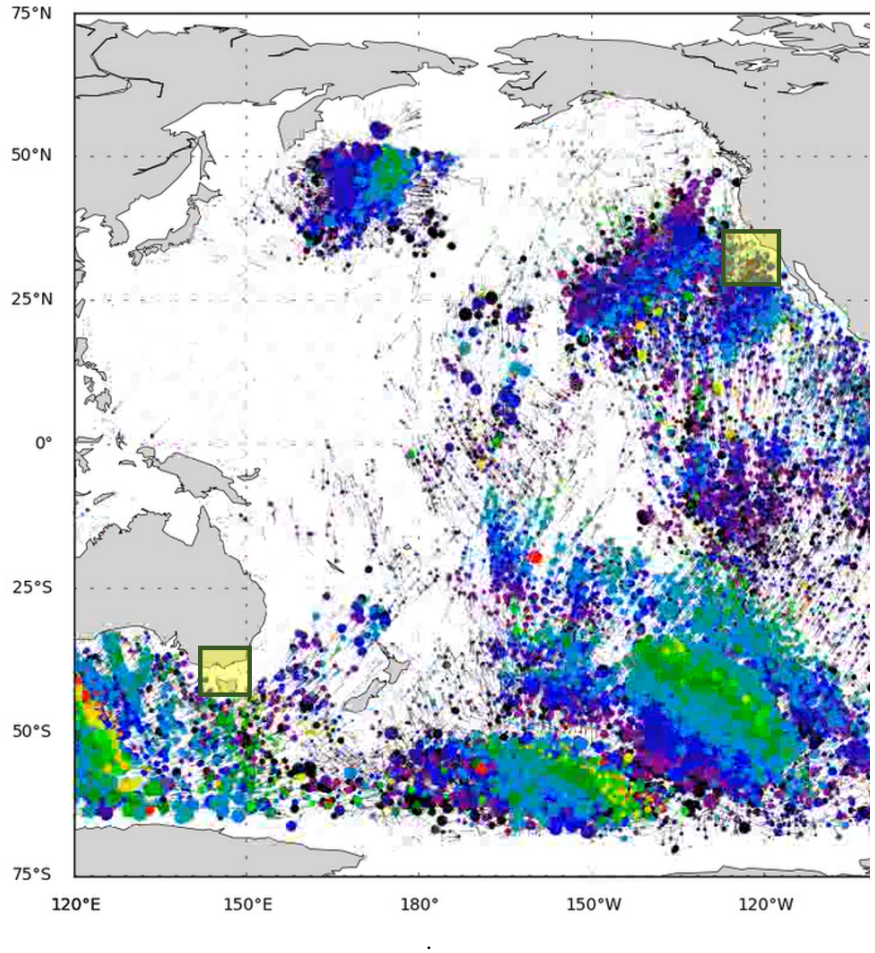

Figure 3.3: Location of the two oceanic calibration areas (yellow squares) concerning the main swell systems seen in the firework plot of April 12, 2023. Blue-green-red dots: small-intermediate-big swell systems (Collecte Localisation Satellites, 2023)

Figure 3.2 and Table 3.1).
R4, R5 and R6 are ensured when selecting buoy data from station 46047 from the NDBC network (National Data Buoy Center, 2023) and station 46219 from CDIP (Coastal Data Information Program, 2023). As the historical data is reported by NDBC for both stations, these NDBC station reference numbers will be used throughout the report. These buoys are located within a 30 to 100 km of distance from the satellite tracks, a distance that swell waves can travel without undergoing a significant change in characteristics. More information about the buoys can be found in Section 3.4.
Finally, **R7** is met by locating the segments of the satellite track as far as possible from the coast, where deep water conditions are met, as explained in Section 2.2 in Equation 2.1. This ensures that sudden changes in wave conditions like wave breaking are avoided: these would lead to misinterpreting the results as the retrieved FFSAR spectra would be compromised.

3.1.1. Level-1A data request

As input to the FFSAR processor, Level 1a HR NTC (High-Resolution Non-Time Critical) data was used; this data was sourced from the EUMETSAT data centre (Eumetsat, 2023), where it is freely accessible. The processing of two segments matching the requirements listed in Section 3.1 was requested. The specifications of the data request are summarised in Table 3.1.

The period specified in Table 3.1 covers all the available and applicable passes over the area at the time of the request. As seen data from the very beginning of the mission in Dec. 2020 could not be used as raw data was not generated until February 2021 could not be used as raw data was not generated until February 2021. The transponder acquisition mode was then active over Catalina instead of the raw acquisition mode to define the Catalina transponder's best location. This also impacted some track 119 passes of late 2021 and early 2022 which could not be considered for the performance analysis (the

Table 3.1: Overview of the satellite data requested for FFSAR processing

	segment 1 (pass 119)	segment 2 (pass 206)
Time period	22.12.2020 -23.02.2023	25.12.2020 -26.02.2023
Type	ascending	descending
Passes available	71	76
Passes with RMC, raw waveforms	44	55
Latitude interval	32.00° -32.91° (100 km)	
RMC latitude sub-interval	32.00° -32.50° (~50 km)	
raw latitude sub-interval	32.50° -32.91° (~50 km)	

available vs usable number of passes is also specified in Table 3.1). An overview of the remaining passes where both raw and RMC are available is provided in Appendix A in Table A.1.

3.2. FFSAR processing (Level 1a to Level 1b)

The FFSAR L1B High Resolution (HR) waveforms necessary for the generation of the satellite-derived spectra over the given study area were obtained through Earth Console, a cloud environment that gives access to the AREALT-FF1 FFSAR processor, developed by Aresys (Scagliola et al., 2021). As mentioned in Subsection 2.4.1, this processor makes use of the Omega-Kappa processing algorithm adapted for FFSAR by Guccione et al. (2018). The reason behind the choice of this processor lies in its availability at the time of data sourcing: the on-demand processing options offered by the P-PRO altimetry services on earthconsole.eu provided excellent technical support and a clear overview of the processing settings.

Table 3.2: Processing parameters description and constraints, adapted from Orrù (2021)

Processing parameter	Possible values	Description
Range oversampling factor	1, 2	1: no zero padding 2: zero padding (see Subsection 2.5.3)
Processed bandwidth factor	0.25 -1.00	Fraction of the Doppler bandwidth that is processed to generate the FF-SAR single look waveforms, allowing to control the along-track resolution
Multilook posting rate	1, 20, 80, 100, 200, 500	Approximate waveform spacing in frequency (Hz). The actual spacing will vary slightly along the orbit depending on orbital parameters
Append the ALES+ FFSAR output to the output NetDCF product	Yes No	User can decide whether to fit the waveform using the ALES+ FFSAR empirical retracking algorithm to estimate range. If Yes: set range oversampling to 1

The processing time was sponsored by ESA's Network of Resources (NoR) sponsorship (European Space Agency, 2020). Assessing the performance of this processor is beyond the scope of this work, but it would be beneficial to explore results obtained with back-projection algorithms such as the one employed described by the FFSAR pioneers Egido and Smith (2017) (see the recommendations on this matter in Chapter 6). The processing parameters which could be configured on Earth Console's service are listed and explained in Table 3.2 and the selected configuration is reported in Table 3.3.

A range oversampling factor of 2 was selected and therefore zero-padding is applied during FFSAR processing (more about zero-padding is explained in Subsection 2.5.3). The processed_bandwidth_factor was recommended to be set to 0.6 (instead of 1) for ocean applications in order to remove Doppler ambiguities (from private communication, Fornari (ESA), 2022). As a consequence, the adaptation of data_block_length and data_block_margin to 2.1 was required (this corresponds to an integration time of 2.1 seconds in the back-projection algorithm). The multi-look posting rate was set to 200 Hz (on the higher end of the available posting rates) as higher posting rates lead to lower noise (Egido et al., 2021).

Considering the ground-track speed of 5800 m/s (Table 2.1), this posting rate leads to an on-ground resolution of ~29 m (distance between waveforms), which over segment 1 and segment 2, leads to a range of ~3500 waveforms available for further processing. It will be however seen in the next section, that only a portion of each segment was used to generate FFSAR spectra.

Table 3.3: FFSAR processor settings

Parameter	Value
Processor type	s6
L1B FF SL product flag	false
Range oversampling factor	2
Processed bandwidth factor	0.6
Multilook posting rate	200 Hz
Grating lobes mitigation flag	false
Grating lobes mitigation threshold	35
Data block length	2.1
Data block margin	2.1

3.3. FFSAR spectra generation

The FFSAR processor output resulted in L1B multi-looked waveforms for both segment 1 and segment 2, gathered in netCDF files for each separate pass date (see Table A.1 in Appendix A). As seen in Figure 3.2, each segment contains both raw and RMC waveforms. The latitude interval corresponding to each operating mode was therefore defined for each data file in order to separate the raw and RMC FFSAR waveforms and to allow the creation of separate spectra for each mode. To identify the latitude at which the calibration area starts (segment 1,2 starting points), the values of power at the last bin were extracted and waveform intervals with a power signal at the last bin were identified as raw waveforms. The separation between raw and RMC in segment 1 is well visualised in Figure 2.20 for a L1B dataset collected over the AOI. The resulting raw and RMC L1B FFSAR waveforms are then used to retrieve the corresponding FFSAR spectra using the processor by Altiparmaki et al. (2022). An example of raw and RMC waveform for a given pass is seen in Figure 3.4, where the differences in the two waveforms are due to the fact that they are retrieved from two different portions of segment 1 (as explained, different latitude intervals apply for the collection of raw and RMC waveforms).

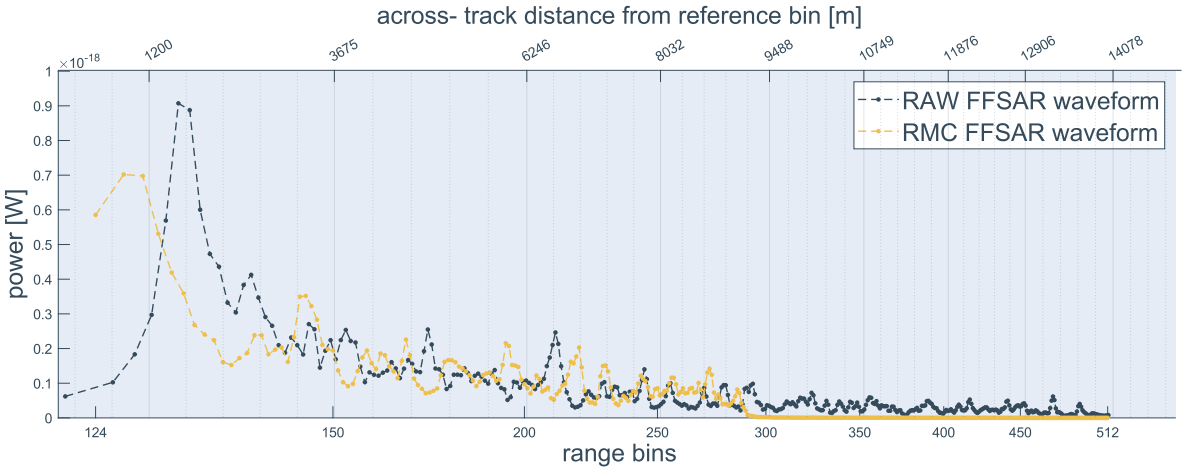

Figure 3.4: FFSAR raw (blue) vs RMC (yellow) waveforms collected by pass 119 of S6 over the AOI on 26.11.2022. Both range bins and the corresponding projected distance from nadir are shown. The across-track resolution increase is made evident by the reduced bin spacing in the trailing ege

The following S6 parameters were specified:

- **Range bin sampling distance:** 0.1897 m, see Subsection 2.5.3
- **Trailing edge start bin:** ~ 124 (100 in Eumetsat L1B UFSAR)
- **RMC last bin:** 300

- **raw last bin:** 512

It should be noted that during L1A to L1B FFSAR processing, the waveforms were shifted down as seen in Figure 4.1 (it was tested by Earth Console that surface elevation retrieval is not compromised by this shift), this explains why the last usable bin for RMC waveforms is bin 300 instead of bin 263, which is the ”cutting point” for RMC in Eumetsat Level 1b UFSAR data (from private communication, Fornari (ESA), 2023), as seen in Figure 2.20.

The FFSAR spectra were generated for each pass, for each segment, for both raw and RMC waveforms following the processing steps illustrated below, from Altiparmaki et al. (2022)'s methodology:

1. **Define cutting window along-track:** From the available raw and RMC waveform intervals, a suitable window of waveforms to be considered for the spectra generation is set by selecting a starting latitude along segment 1 ad 2 and window width. This sub-setting action ensures that waveforms generated in proximity to the limits of the calibration area are avoided, as mode switching can cause power losses around. The choice of the starting latitude and interval width is based on the considerations explained in Subsection 4.2.4. The cutting window is limited along-track by the parameters *wmin* and *wmax* and cross-track by the parameters *lim1* and *lim2* (see step 2) which are visualised in Figure 3.5.

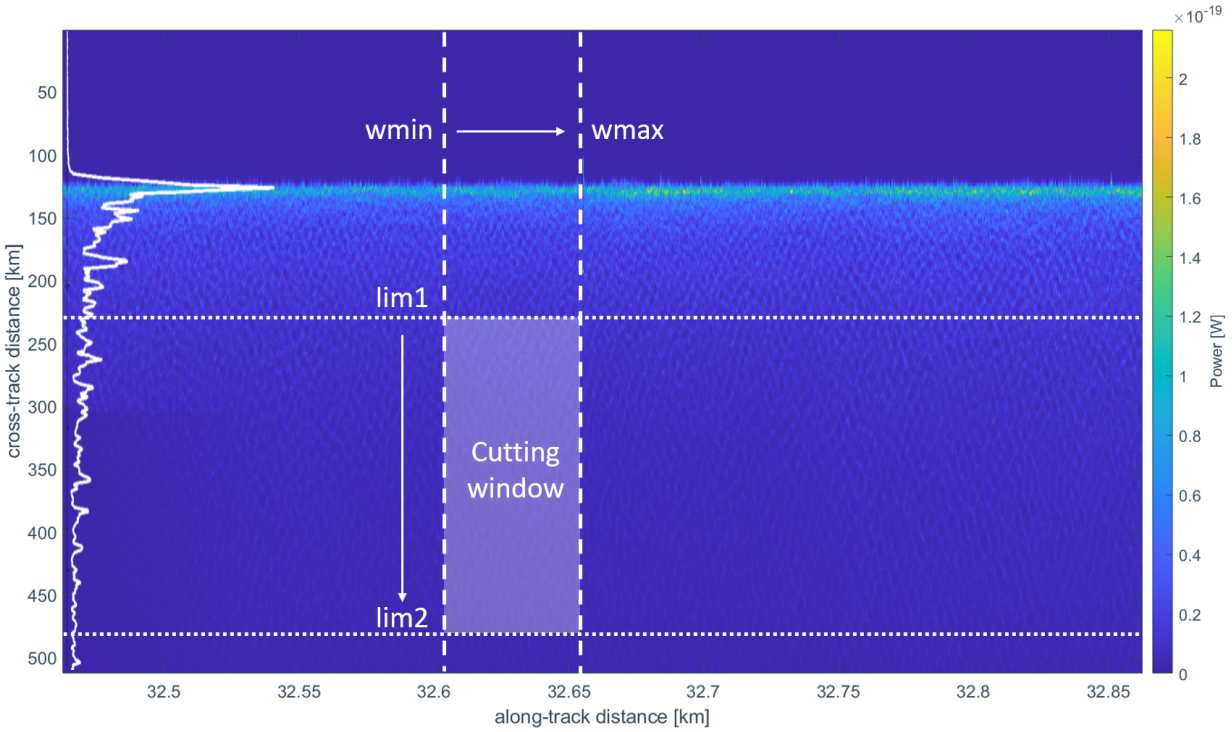

Figure 3.5: Latitude and waveform interval limits considered for FFSAR spectra generation

2. **Define cutting window across-track:** An interval *lim1* -*lim2* is defined to select the portion of the projected waveform tail to be normalised and used for spectra generation. *lim1* and *lim2* are measured in km starting from the reference bin of the projected waveform considered. Such reference bin is defined as the point in the leading edge where $P = 0.5P_{max}$. The reference bin is illustrated in Figure 3.6 together with *lim1* and *lim2*, which were set following the sensitivity analysis reported in Section 4.2. This reference bin could slightly change for each waveform: this is because, for different waveforms, the maximum power might be reached at different points. This step can be seen as applying a simple threshold retracker to align the waveforms before projecting on the ground. As Altiparmaki et al. (2022) stated, however, in the case of data sets with bigger misalignments, a multiple-step realignment strategy should be applied to avoid misprojection errors.

3. **Waveform filtering and fitting:** The waveforms are filtered and fitted: a Low Pass Filter followed by convolution along-track smooths the signal. Then, the coefficients of a degree-4 polynomial are

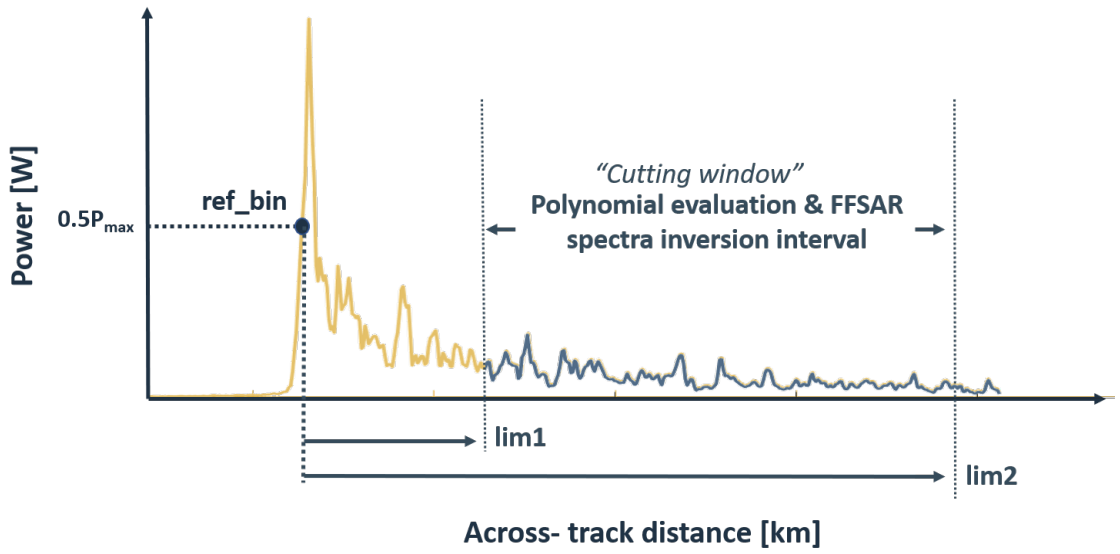

Figure 3.6: Visualisation of the cutting window limits on a raw waveform projected in across-track direction

evaluated based on the portion of the tail between *lim1* and *lim2*.

4. **Waveform normalisation:** A normalisation of the remaining original signal with respect to the fitted waveform signal is performed. The original waveform, together with the polynomial fitted on it and the resulting normalised waveform are shown in Figure 3.7.

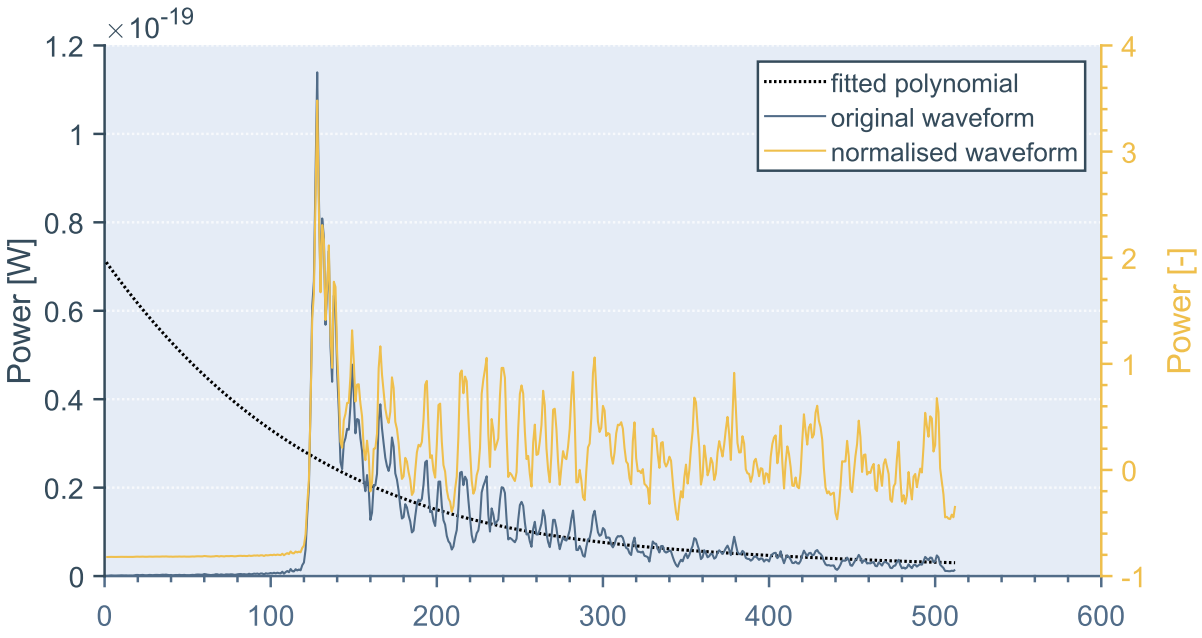

Figure 3.7: Example of an original waveform for segment 1 (track 119), its fitted polynomials for different window sizes, and the corresponding normalised waveforms (mean-centred ratio of the remaining original signal to fitted values)

5. **FFSAR spectra computation:** The normalised projected waveforms undergo a Fast Fourier Transform which generates the FFSAR spectra for each applicable pass, segment, operational mode (raw/RMC) and cutting window defined. This step can be visualised in Figure 2.14, where the projected radargram and FFSAR spectra corresponding to the cutting window shown in Figure 3.5 are shown.

3.3.1. First-degree estimate of swell period from FFSAR spectra

Although FFSAR spectra are not directly convertible into ocean wave spectra, a first estimate of the swell period T_s can be inferred from the FFSAR spectra. T_s is obtained from the wave-number k corresponding to the maximum power in the spectra as described in Equation 3.1. This relation between the swell period

and the wave-number follows from linear wave theory.

$$k_{maxE} = \frac{2\pi}{L_{maxE}} = \frac{4\pi^2}{g \cdot T_s^2} \Longrightarrow T_s = \sqrt{\frac{4\pi^2}{k_{maxE} g}} \tag{3.1}$$

where k_{maxE} is the radial component of the point of maximum power in polar coordinates. Given the 180° ambiguity of the power peak (which gets mirrored in the two quadrants where the waves travel (Bao and Alpers, 1998)), this can lead to two points of maximum power, both having the same power, wave-number and therefore T_s (this was clearly visible in Figure 2.14). It has to be noted that by estimating the swell period this way, only the primary power peaks in the spectra are considered and information from secondary peaks that might also be associated to the wave spectra is ignored.

3.4. Buoy data

In order to assess the performance of the FFSAR swell period estimates, buoy data has been retrieved from NDBC's station 46047 and station 46219 (operated by CDIP). The relative positioning of the buoys with respect to the satellite tracks is seen in Figure 3.2. These buoys were chosen as they are the source of validation data closest to the tracks and provide the highest time resolution for measurements.

3.4.1. Data description and sourcing

Buoy 46047 selected from the NDBC network is equipped with a Self-Contained Ocean Observations Payload (SCOOP) payload configuration (seen in Figure 3.8a), a recent set of instruments that allows continuing the measurements of ocean and wave parameters on a smaller, more efficient and advanced platform (Craig Kohler et al., 2015). This new payload reaches the same accuracy of previous configurations (Hall et al., 2018).

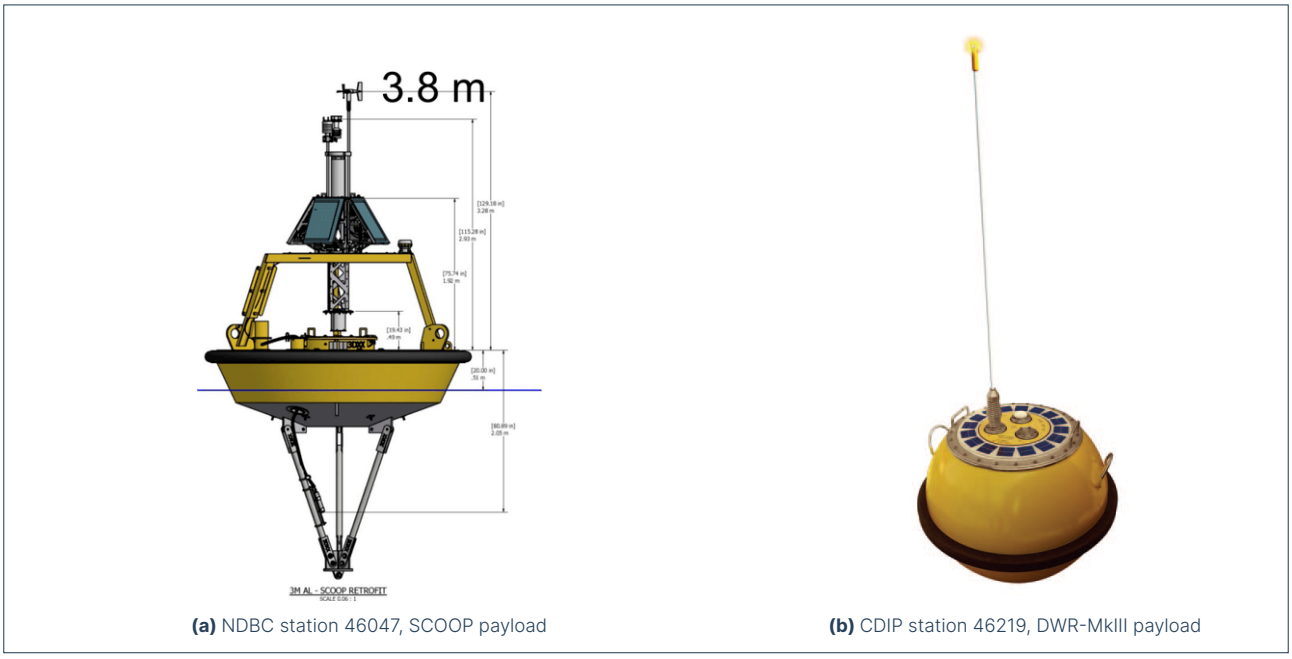

(a) NDBC station 46047, SCOOP payload

(b) CDIP station 46219, DWR-MkIII payload

Figure 3.8: Buoys used for validation

Buoy 46219 (Figure 3.8b) from CDIP features the Datawell Directional Waverider Mark III (DWR-MkIII) payload O'Reilly et al. (1996) of which the measuring characteristics are reported in Table 3.4 together with those of 46047 for the selected parameters. In the historical files of buoy 46047, measurements are reported every hour at the 40th minute as the averaging period begins on the 20th minute of every hour and lasts 20 minutes, while wind information is reported at every tenth minute. CDIP's buoy 46219 on the other hand starts a new averaging period on the half-hour and on the hour; the data (spectral and the parameters derived from it) is therefore reported on the 26th and 56th minute. Because of its higher sampling frequency, buoy 46219 was chosen as the reference platform for peak period measurements. The period data was retrieved from NDBC historical data (provided by CDIP). The wave direction and height have also been obtained from buoy 46219 in order to limit the spatial variability of the performance analysis, while information relative to the wind (speed and direction) was retrieved from buoy 46047 as

Table 3.4: Buoy payload specifications for chosen parameters

Parameter	Accuracy		Resolution		Averaging period	
	46047[b]	46219[a]	46047[b]	46219[a]	46047[b]	46219[a]
DPD	N/A	± 3% of value	N/A	0.01 s	N/A	26.6 min
MWD	N/A	± 10°	N/A	1°	N/A	26.6 min
SWH	N/A	< 1.0 % of value	N/A	1 cm	N/A	26.6 min
WDIR	10°	N/A	1°	N/A	8 min	N/A
WSPD	± 1 m/s	N/A	0.01	N/A	8 min	N/A

[a]Coastal Data Information Program (CDIP) (2018); Stoker (2020) [b]National Data Buoy Center (2017)

46219 does not feature wind sensors. A summary of the buoy parameters extracted from the historical data files is provided as follows:

- **Dominant (peak) Wave Period (DPD) [46219]:** in seconds, the inverse of the frequency with the highest energy density in the spectrum (peak period). This quantity will be compared with the swell period estimate from satellite spectra. *Performance metric. Retrieved for buoy 46219 from NDBC historical files*.

- **Mean Wave Direction (MWD) [46219]:** in degrees clockwise from true North, the mean direction from which the waves at the peak period are coming. This does not necessarily correspond to the direction of the highest energy waves (i.e. if there are multiple wave fields at the same frequency, MWD will not be the direction of the most energetic wave field, it will be the mean direction of all wave fields). *Retrieved from NDBC historical files. Used to compute swell travel time between buoy and satellite track in Equation 3.2*.

- **Significant Wave Height (SWH)**[1] **[46219]:** in meters, the average height of the highest one-third of the records of the sampling period *Retrieved from NDBC historical files, affects parameter retrieval from FFSAR spectra (Altiparmaki et al., 2022) and can therefore support FFSAR spectra interpretation*.

- **Wind Direction (WDIR) [46047]:** in degrees clockwise from true North, average direction from which the wind is coming. *Retrieved from NDBC historical files, provides additional insight for performance analysis*.

- **Wind Speed (WSPD) [46047]:** in m/s. *Retrieved from NDBC historical files, provides additional insight for performance analysis*.

3.4.2. Buoy data processing

The historical files containing the data recorded from both buoys in the time period of interest seen in Table 3.1 were downloaded. Only the dates matching valid satellite passes (featuring raw, RMC) were considered (an overview of collected satellite data for the chosen segments is shown in Appendix A, Table A.1). As explained in Section 2.2, it is important to determine if deep water conditions apply over the segments considered, to allow the application of linear wave theory to compute the wave group velocity and wave travel time. To check for this, Equation 2.2 was solved with trial and error for the maximum period measurement performed by buoy 46219 (T = 22s on Jan 24 2023, as seen in Appendix B) and for the average ocean depth d_{avg} below the satellite ground track segment considered (see Table 3.5). Using the resulting wavelength L for both segments, it could be confirmed that deep water conditions ($\frac{d_{avg}}{L} > 0.5$ from linear wave theory) apply for both segments 1 and 2, thus no further data sub-setting was needed. It was then important to ensure that the comparison of buoy and satellite parameters was performed on the same swell system thereby reducing the effect of time-dependent changes in the ocean surface on the analysis. For this, the time Δt necessary for the swell wave to travel between the buoy and the satellite's track segment (represented as its midpoint M in Figure 3.9) was computed using

[1]this parameter is reported in NDBC data as WVHT

Equation 3.2 (Altiparmaki et al., 2022):

$$\Delta t = \frac{\Delta X}{C_g} cos(MWD - \phi_m) \tag{3.2}$$

where:

- ΔX**:** in meters, is the distance from the buoy considered to the segment's midpoint (the reference geometry is visualised in Figure 3.9). It was obtained from Google Earth Pro®, see Table 3.5.
- C_g**:** the wave group speed, follows from Equation 2.4(linear wave theory).
- ϕ_m**:** in degrees clockwise from true North, is the direction of the alignment of buoy 46219 with the midpoint M of the considered ground-track segment among the two shown in Figure 3.2. It was obtained from Google Earth Pro®, see Table 3.5.
- Average depth: in meters, the average depth of the ocean below the ground-track segments.

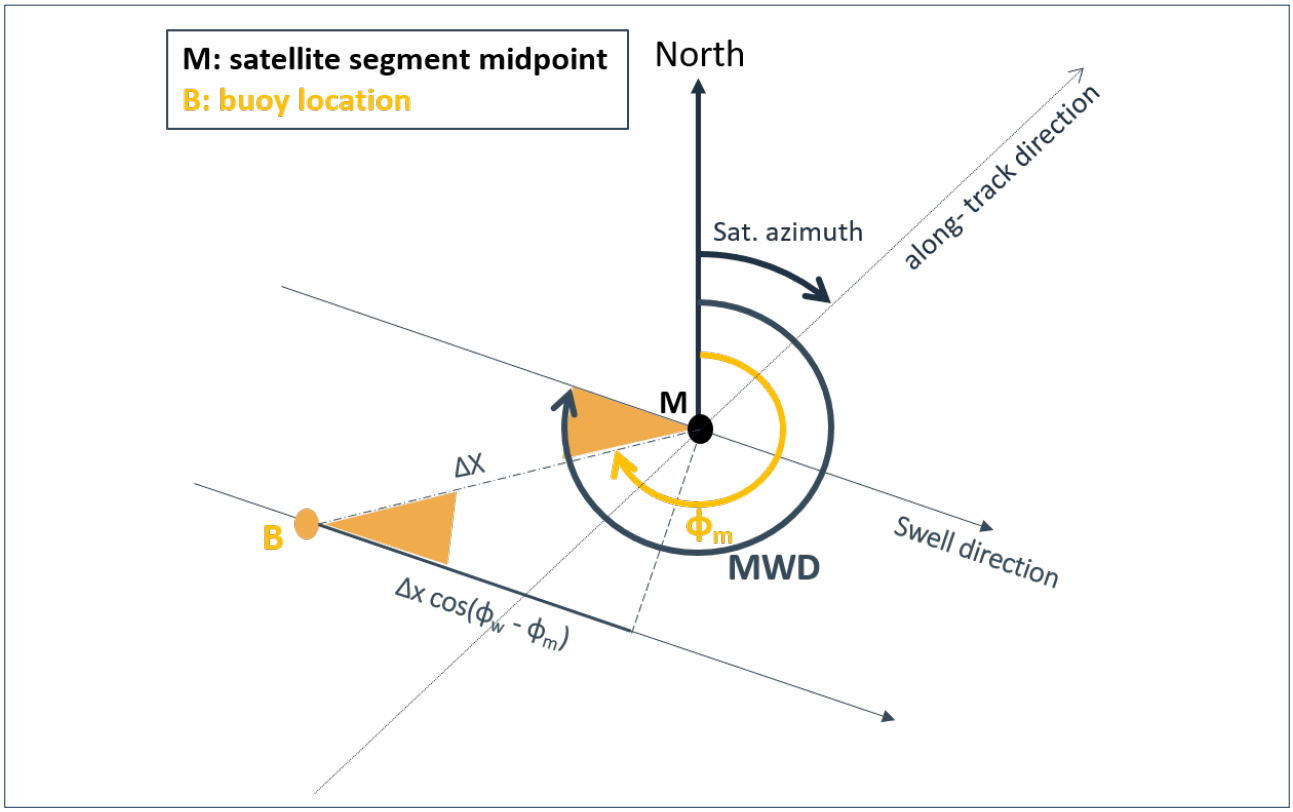

Figure 3.9: Schematic to support wave travel time calculation. ϕ_m: buoy-segment midpoint alignment, MWD: swell direction, ΔX: buoy-segment midpoint distance

As C_g depends on the wave period recorded by the buoy at a given epoch, a value of ΔT was obtained for each epoch. To choose the buoy epoch observing the same swell system as the one recorded at the satellite segment midpoint on a given day, the time t_M when the swell wave system observed by the buoy crossed the track segment midpoint was computed as follows:

$$t_M = t_{buoy} + \Delta t \tag{3.3}$$

It is to be noted that both a positive or negative Δt value could be obtained, depending on the wave travelling direction (positive Δt for waves crossing first the buoy, then the segment midpoint M). With the values of t_M corresponding to each buoy epoch, it was possible to select the epoch matching the swell observed by the satellite by simply considering the one leading to the smallest difference between t_M and the satellite observation time. Such an epoch was then used to retrieve all the relevant buoy parameters for the satellite observation dates.

Table 3.5: Geographical features affecting wave travel time

segment (track)	avg depth [m]	ϕ_m [°]		ΔX [km]	
		46047	46219	46047	46219
1 (119)	1189	239	299	72,2	108
2 (206)	293	219	317	43,5	80.9

3.5. Performance analysis strategy

To compare the swell period estimate retrieved from the FFSAR spectra (raw and RMC) with the one measured by the buoy for all the data points available in the period of interest, it was important to select a performance indicator fitting the application at hand. Both the Root Mean Square Error (RMSE) and the Mean Absolute Error (MAE) were found to be regularly utilized in studies assessing model performance (Brassington, 2017) and were therefore considered. Their formulation is introduced in Equation 3.4 and Equation 3.5 (Chai and Draxler, 2014):

$$RMSE = \sqrt{\frac{\sum_{i=1}^{n} (y_i - x_i)^2}{n}} \qquad (3.4)$$

$$\mathrm{MAE} = \frac{1}{n}\sum_{j=1}^{n} |y_i - x_i| \qquad (3.5)$$

where y_i is the prediction (FFSAR period), x_i is the observation (buoy period) and n is the sample size.

The main characteristic of RMSE is that it squares the errors *before* averaging them, meaning that big errors have a high impact on the RMSE value. The RMSE is therefore sensitive to the presence of a small number of outliers (Brassington, 2017) when compared to the MAE. This would be desirable when penalizing large errors would be needed (ie: if being off by 4 seconds is more than twice as worse as being off by 2 seconds). Furthermore, the RMSE is larger for increasing sample size (as its denominator increases with $\sqrt{n}$). MAE on the other hand averages the absolute differences between prediction (FFSAR period) and observation (buoy period) over the entire test sample (see Equation 3.5), meaning that each data point contributes in the same way to the final MAE value. Furthermore, the MAE measures the average magnitude of errors in a set of predictions, without considering their sign (positive and negative errors of the same magnitude have the same effect on the MAE).

As explained in Section 4.1, when the Level-1B data quality is degraded, the FFSAR parameter retrieval gets compromised. The outliers occurring, in this case, were removed before further analysis. As the remaining errors have an importance which is proportional to their value, it was deemed unnecessary to apply the RMSE. An additional reason for picking MAE as a performance indicator was that raw and RMC data sets do not necessarily have the same sample size (as explained, this can occur as either raw or RMC Level 1b data is compromised for a given pass). A difference in sample size would affect the RMSE value obtained for raw and RMC respectively, making it more challenging to analyse the results.

4

Results

In this chapter, the results obtained following the steps described in Chapter 3 are shown, analysed and discussed. As a first step, the available satellite data were pre-processed to remove passes without swell and outliers caused by compromised echoes. This is explained in Section 4.1. Then, a sensitivity analysis (Section 4.2) is performed on the across-track position of the cutting window on which polynomial evaluation and subsequent spectra generation are based for each FFSAR radargram. The sensitivity analysis was done for both raw and RMC waveforms, evaluating the swell period retrievals corresponding to different combinations using the Mean Absolute Error analysis. The optimal settings that were found were then used to explore a few different along-track window combinations and then generate the data set employed for the performance analysis, which is reported in Section 4.3, where the RMC and raw swell period are finally compared to the validation (buoy) data.

4.1. Pre-processing of data

Two processing steps were applied to the data before obtaining the final sample sizes:

- **Swell filter**: Only passes where swell was detected by the buoy (period > 10s, the cutoff value for swell used by CDIP (Coastal Data Information Program (CDIP), 2017)) were considered, leading to a maximum available sample size of 70 passes.
- **Outlier processing**: Only passes where FFSAR swell period retrieval was not compromised by the power deterioration present in the mode transition area were considered. This is explained more in detail below and further reduced the sample size for each case examined.

Before calculating the MAE for each dataset in the sensitivity and the final performance analysis, the available satellite passes were processed to detect the presence of compromised data. As the AOI in question (Figure 3.2) overlaps an area of transition between satellite modes, some satellite tracks suffer from power losses due to the mode switch, especially in proximity of the latitude at which the switch happens. This issue is a direct consequence of comparing data (raw, RMC) from two distinct areas and could be seen by inspecting the FFSAR echograms. It is a system constraint and therefore can't be solved with data processing. In extreme cases, the mode transition can cause the loss of entire data sets. A recommendation highlighting the advantages of using data over the same area is made at point **RC-1** in Chapter 6. To check for the presence of such compromised data sets, the Eumetsat L1B unfocused echoes and Earth Console Level-1B Fully Focused echoes collected in the period of interest were analysed. By investigating the average power of the signal, it was possible to identify passes where this value was much lower than the rest of the passes. An example of a compromised track is shown in the left of Figure 4.1 where it is seen how the Eumetsat Level-1B unfocused radargram is "washed out" and overall the signal is much lower than in a nominal radargram as the one shown for instance in Figure 2.20. Eumetsat L1B data is obtained from the same L1A data sets used to generate the L1B FFSAR echoes, which were equally impacted on the days when the low signal was observed. It can be therefore concluded that the issue regards the original L1A data sets. To avoid the outliers caused by this issue impacting the sensitivity and overall performance analysis, the data points where the detected power signal was low were excluded from the analysis, as they lead to a failure in FFSAR spectra generation. This was

done independently for raw and RMC spectra in the sensitivity analysis, meaning that when raw waveform cutting was investigated, only the passes where the raw portion of the radargram was 'washed out' were excluded and vice-versa for RMC. This resulted in the sample sizes reported in Table 4.5, while an overview of the corresponding excluded passes can be seen in Table B.1 and Table B.2 for each window limit combination.

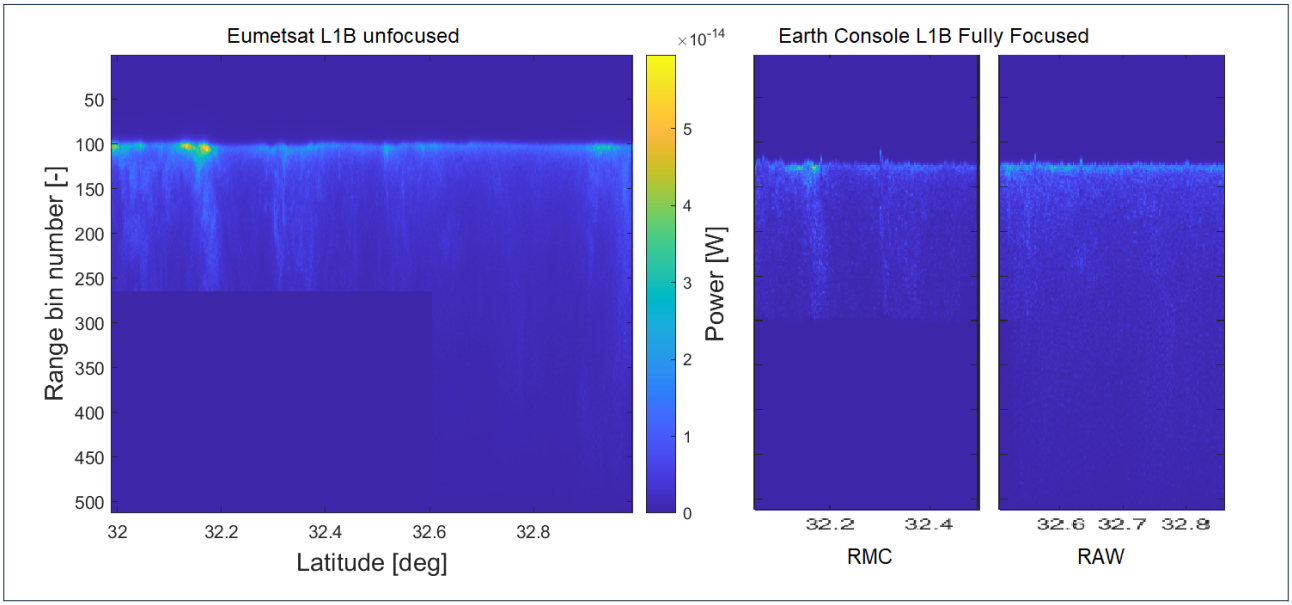

Figure 4.1: Unfocused (left) and Fully focused (right, 2x) echograms of pass 19 on Sep 25, 2021. The down-shift in waveforms in the FFSAR radargram is explained in Section 3.3

4.2. Sensitivity analysis

As seen in Figure 3.5, and explained in Section 3.3, the size of the cutting window considered during FFSAR spectra generation to subset the L1B FFSAR data can be adjusted along-track by changing the parameters *wmin* and *wmax* or across-track by changing the parameters *lim1* and *lim2*. A sensitivity analysis was run on the across-track window limits *lim1* and *lim2* as it has a considerable impact on the performance of the FFSAR retrieval algorithm. The analysis was performed using a fixed 14.5 km-wide along-track interval *wmin = 20 km, wmax = 34.5 km*. Once the best combination was found for *lim1* and *lim2*, a few different options were considered for *wmin* and *wmax* for such combination (see Subsection 4.2.4). The cutting window across-track defines the portion of the trailing edge about which polynomial fitting is performed: the widest possible window for raw waveforms would include the reference bin on the leading edge (defined at the first point of half maximum power on the leading edge) and the last bin (where the power signal is nearly zero), while for RMC waveforms, it can stretch until bin 300 where the trailing edge is cut. The performance of different cutting windows was compared using the MAE metric introduced in Section 3.5 on the swell period estimates retrieved from FFSAR.

4.2.1. Raw waveform cutting window

Before starting the raw cutting window sensitivity analysis, the across-track window was considered in its entirety to identify potential waveform portions to avoid polynomial fitting. The widest window along-track stretches for between $lim1 = 0km$ and $lim2 = 14km$, as can be computed with Equation 4.1), which is derived from Equation 2.6 with h the satellite altitude from Table 2.1, n_{ref} the reference bin number which can be always rounded to 124 and δR_{sr} the range bin sampling distance indicated in Section 3.3.

$$l_{\text{cross}} = \sqrt{[1336 \cdot 10^3 + (512 - 124) \cdot 0.1897]^2 - (1336 \cdot 10^3)^2} = 14024\ m \tag{4.1}$$

As explained in Section 3.3, a polynomial is fitted on the waveform based on the portion of the tail considered by the cutting window. As seen in Figure 4.2, for the full-size cutting window, the remaining signal ratio (original waveform/ fitted waveform, red line in the plot) seems to be higher than one mainly for the last part of the waveform. This indicates that the choice of a degree-4 polynomial is not ideal for fitting the original waveform, as the difference between the original waveforms and the fitted polynomials is significant. Investigating possible polynomials that better fit a larger portion of the waveform goes

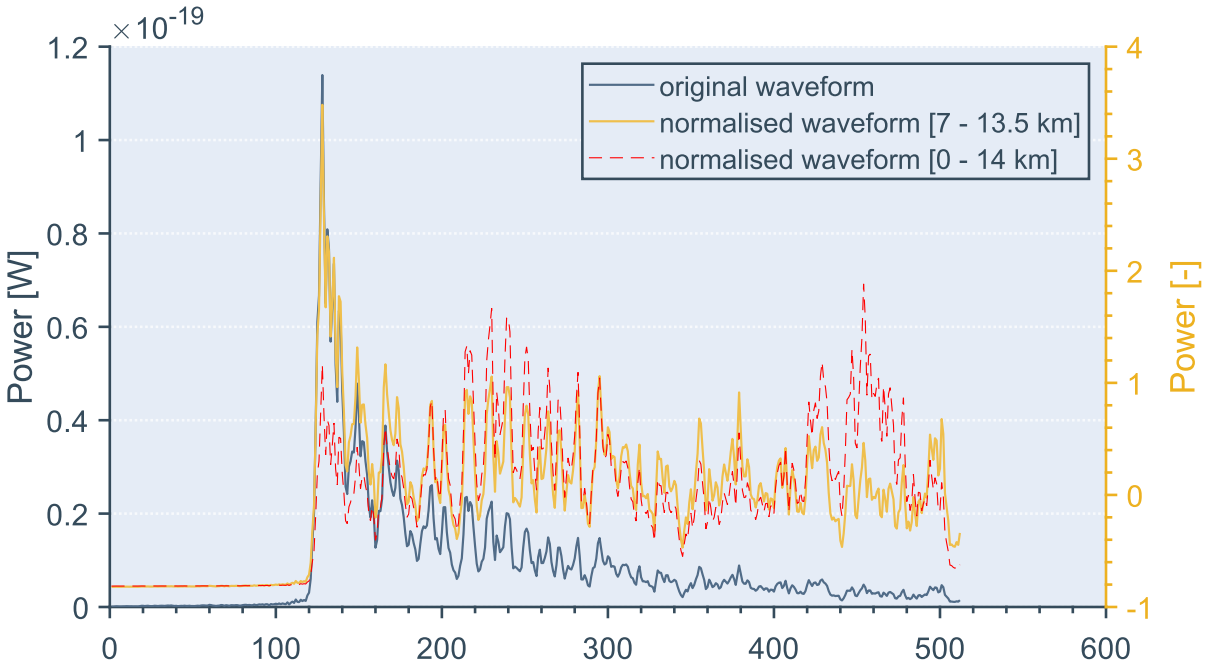

Figure 4.2: Example of an original waveform for segment 2 (track 206) and the corresponding normalised waveforms (mean-centred ratio of the remaining original signal to fitted values) obtained from two different combinations of fitting polynomials

beyond the scope of the project: this leads to recommendation **RC-5:** in Chapter 6. To be able to infer swell parameters from the FFSAR spectra, the size of the cutting window was reduced and the window was shifted towards the trailing edge to ensure a fitting in the waveform section most impacted by swell. A polynomial fitted on the trailing edge leads to a lower remaining signal ratio for the tail of the waveform (see yellow line in Figure 4.2) when compared to the full-scale cutting window setting considered above. This is definitely desirable when considering that waveform distortions due to swell are to be encountered in the tail (as explained in Subsection 2.5.3), which as a consequence needs to be normalised most optimally. These considerations resulted in the selection of the following cutting window combinations to be investigated (lim1-lim2): 4-10 km, 6-12 km, and 8-14 km. These combinations all have a fixed window width of 6 km such that only the effect of window positioning is investigated. This width was selected as it allows the exploration of different sections of the entire trailing edge, which, as shown in Figure 3.4 starts at about 4 km from the reference bin. The effect of changing the window width is not investigated at this point, a recommendation about this is made in Chapter 6 (see **RC-2**).

In order to evaluate which combination led to the best retrieval of parameters, FFSAR spectra were generated from RAW waveforms projected and cut at the selected intervals. The swell period estimate was then retrieved from the FFSAR data set and compared to the buoy measurement using the Mean Absolute Error analysis explained in Section 3.5. The swell period estimates per pass can be seen in Table B.1 while the final MAE values are reported in Table 4.1 for each limit combination. It should be noted that due to the pre-processing of the data sets explained in Section 4.1, the different limit combinations considered correspond to slightly different sample sizes (some combinations allowed for parameter retrieval even from compromised radargrams).

Table 4.1: MAE values for swell period retrievals from different cutting window limits for raw waveforms

lim1-lim2 [km]	MAE raw [s]
4-10	2.73
6-12	2.24
8-14	1.98

The combination leading to the lowest MAE and therefore to swell periods closer to the peak periods measured by the buoy is the cutting window from 8 to 14 km across-track. This was expected, as the

last part of the waveform features an increased range bin resolution (see Figure 2.3.3). Furthermore, as explained above, the chosen polynomial best fits the trailing edge, leading to improved performance in parameter retrieval. Having observed this behaviour, the cutting window was modified further to explore the following combinations (lim1-lim2): 7-13 km and 7-13.5 km. The last km of the projected waveform was left out in an attempt to reduce the fitting issues around it. This led to the MAE values reported in Table 4.2: From this final iteration on the limits, it can be concluded that the best across-track cutting window for the

Table 4.2: MAE values for swell period retrievals from different cutting window limits for raw waveforms

lim1-lim2 [km]	MAE raw [s]
7-13	1.87
7-13.5	1.77

raw waveforms is obtained by setting lim1 = 7 km and lim2 = 13.5 km from the reference bin. This leads to a Mean Absolute Error of 1.77 s which is the lowest encountered when changing the window limits. This optimal window will be used to analyse the performance of FFSAR spectra swell period retrieval from raw waveforms. The window closest to the leading edge however performs considerably worse (period retrievals are around one more second off the observations with respect to the best solution). This is in line with the previous considerations regarding poorer polynomial fitting and a lower range resolution at the beginning of the waveform.

To visualise the effect of considering different cutting window limits on the FFSAR spectra and projected radargrams, Figure 4.3 was generated. In the figure, data obtained from pass 119 and buoy 46219 on 26.11.2022 are shown. On this day, a high-period swell system is observed by the buoy (period of $\sim$ 17s). It can be observed that moving the window towards the trailing edge leads to the formation of multiple power peaks in the FFSAR spectra. For the 8-14 km window, however, the secondary peaks lead to a worse estimation of the swell period, while for the 7-13.5 km, the additional signal leads the period estimation towards the right direction. As explained in Subsection 3.3.1, the swell period estimate is retrieved based on the point in the FFSAR radargram where the power is highest. This means that secondary peaks (as the one seen in Figure 4.3 for the 8-14 km interval) are not relevant for period detection. This limitation might lead to under-evaluating the performance of certain retrievals. It is challenging to determine the correlation between the FFSAR power peaks and the wave spectra seen in Figure 4.4, as there might be ambiguities caused by the satellite's rolling movement (Altiparmaki et al., 2022), or by the effect that certain wave conditions can have on the modulations. As the FFSAR spectrum is not a wave spectrum, no direct conclusions can be drawn from this inspection, however, a recommendation to include a secondary peak in the performance analysis is made (**RC-3** in Chapter 6). A final recommendation that follows from this analysis is **RC-4**, regarding a more in-depth sensitivity analysis, considering other unexplored combinations of *lim1* and *lim2* (for example considering different window widths across-track).

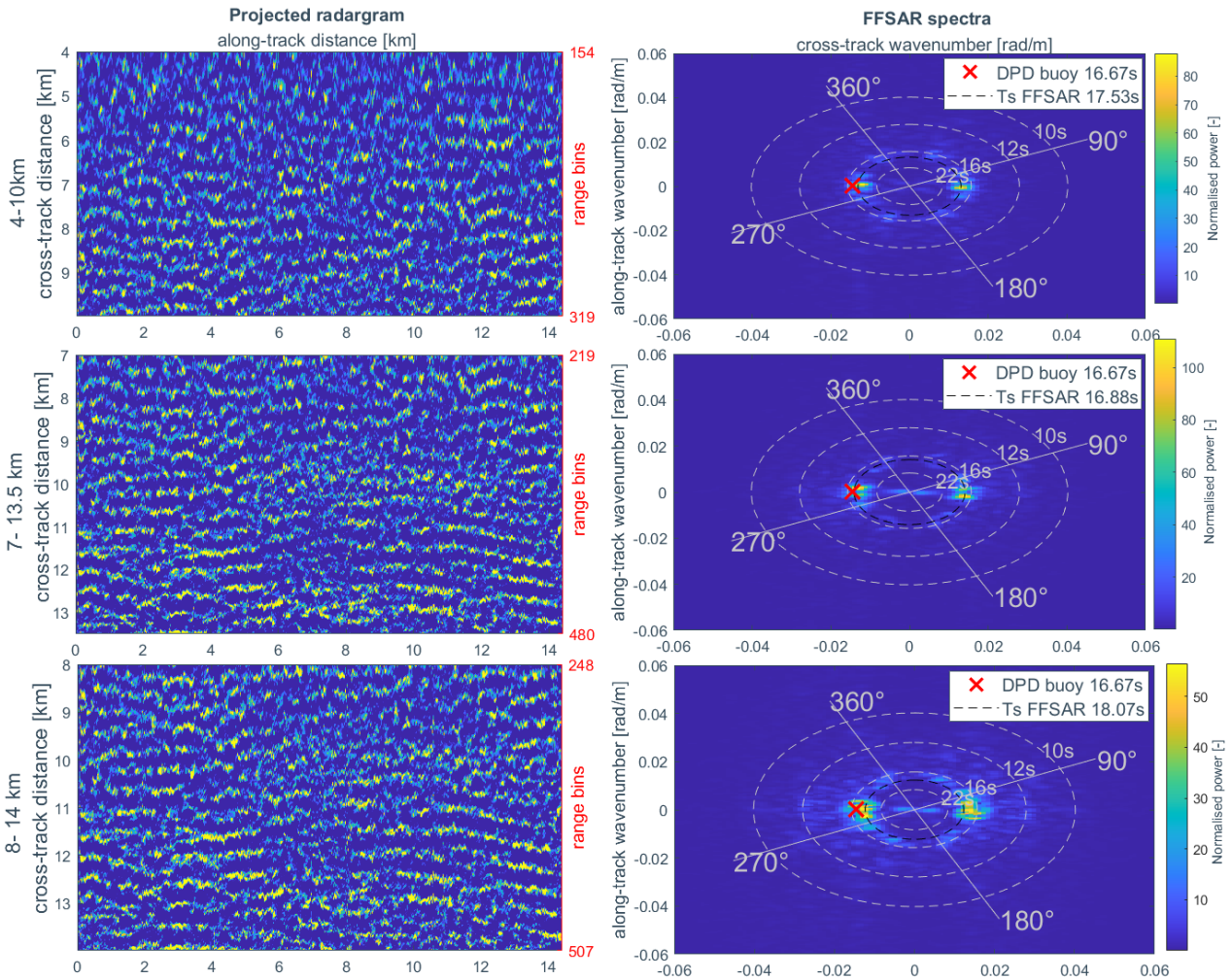

Figure 4.3: Projected radargrams (left) and relative FFSAR spectra (right) retrieved by pass 119 of S6 over the AOI on 26.11.2022. (WSPD= 1.4 m/s, SWH= 2.36 m) for 3 different raw across-track windows

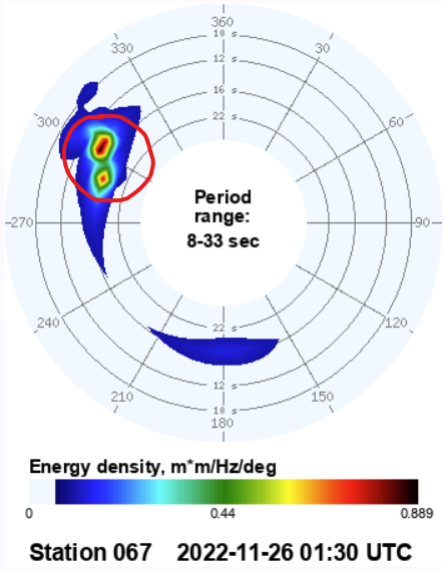

Figure 4.4: Wave spectra collected by buoy 46219 on 26.22.2022 at the time of the satellite observation. Two energy peaks (red circle) of swell waves travelling in similar directions are observed (Coastal Data Information Program (CDIP), 2022)

4.2.2. RMC waveform cutting window

The sensitivity analysis on the position of the cutting window across-track was performed also for the RMC waveforms. In this case, the maximum size of the window is limited by the last available RMC bin which is at around bin 300 (see Section 3.3). This corresponds to an across-track distance of ~ 9.5 km

as seen in Figure 3.4, which is, therefore, the maximum value which can be set for *lim2*. The left-side limit of the cutting window (minimum value of *lim1*) can be set as far back as 4 km for the same reasons reported for the raw sensitivity analysis. As the RMC waveform is about half of the raw waveform, the cutting window width for the RMC sensitivity analysis was set to 3 km. To cover the available width of the cutting window, the following combinations were considered (lim1-lim2): 4-7 km, 5-8 km, 6-9 km. The MAE analysis was then performed, leading to the results reported in Table 4.3. The values of all the relevant parameters (buoy peak period DPD, FFSAR swell period estimate T_s, satellite pass timestamp...) are reported in Table B.2. The cutting window limits lead to the lowest value of MAE and therefore the best

Table 4.3: MAE values for swell period retrievals from different cutting window limits for RMC waveforms

lim1-lim2 [km]	MAE RMC [s]
4-7	3.3
5-8	3.03
6-9	2.92

series of FFSAR swell period retrievals was found to be 6-9 km among the considered combinations. As noted above, however, the RMC projected waveform extends up to 9.5 km across the track. In pursuance of the best-performing combination, it was decided to consider four additional combinations extending the window until its right-most extreme for RMC which features the highest range resolution. The window width was kept to 3 km and the following sequences of limits were examined: 6.1-9.1 km, 6.2-9.2 km, 6.3-9.3 km and lastly 6.4-9.4 km which ends on the last bins of the RMC waveform. The results of this iteration are reported in Table 4.4. From this additional MAE analysis, it can be concluded that, based

Table 4.4: MAE values for swell period retrievals from different cutting window limits for RMC waveforms

lim1-lim2 [km]	MAE RMC [s]
6.1-9.1	2.75
6.2-9.2	2.83
6.3-9.3	2.85
6.4-9.4	3.42

on the intervals investigated, the most suitable cutting window for RMC waveforms is between 6.1 and 9.1 km across-track, with a Mean Absolute Error of 2.75 s with respect to the peak period measured by the buoy. From the MAE values in Table 4.3 and Table 4.4, it appears that the intervals closest to the beginning and to the end of the waveform perform the worst. While a low performance is expected from a window close to the leading edge (due to the poor polynomial fitting and lower resolutions explained in Subsection 4.2.1), the higher MAE for the 6.4-9.4 km interval could be explained by normalisation issues encountered due to the very low power values in the last bin of the RMC waveform where a particularly low signal is encountered. Parameter retrieval is consequentially compromised.

The impact of moving the cutting window towards the final part of the RMC waveform is shown in Figure 4.5, where the performance increase in parameter retrieval is made evident by the improvement in the FFSAR swell period estimate for the 6.1-9.1 km window, where the signal aliasing in the top and bottom quadrant of the FFSAR spectrum is significantly reduced. The buoy spectra corresponding to the satellite timestamp for the considered pass are shown in Figure 4.6. A relatively long swell is observed on that day (period of $\sim$ 18s), no other wave groups seem to be present. As the deformations in the waveform cause constructive velocity bunching for longer swells (due to the lower degradation in azimuthal resolution), parameter estimation from FFSAR is facilitated especially in the case of RMC where a shorter radargram is available. This explains why all the limit combinations lead to a relatively good swell period estimate, which falls within 2 seconds of the observed peak period.

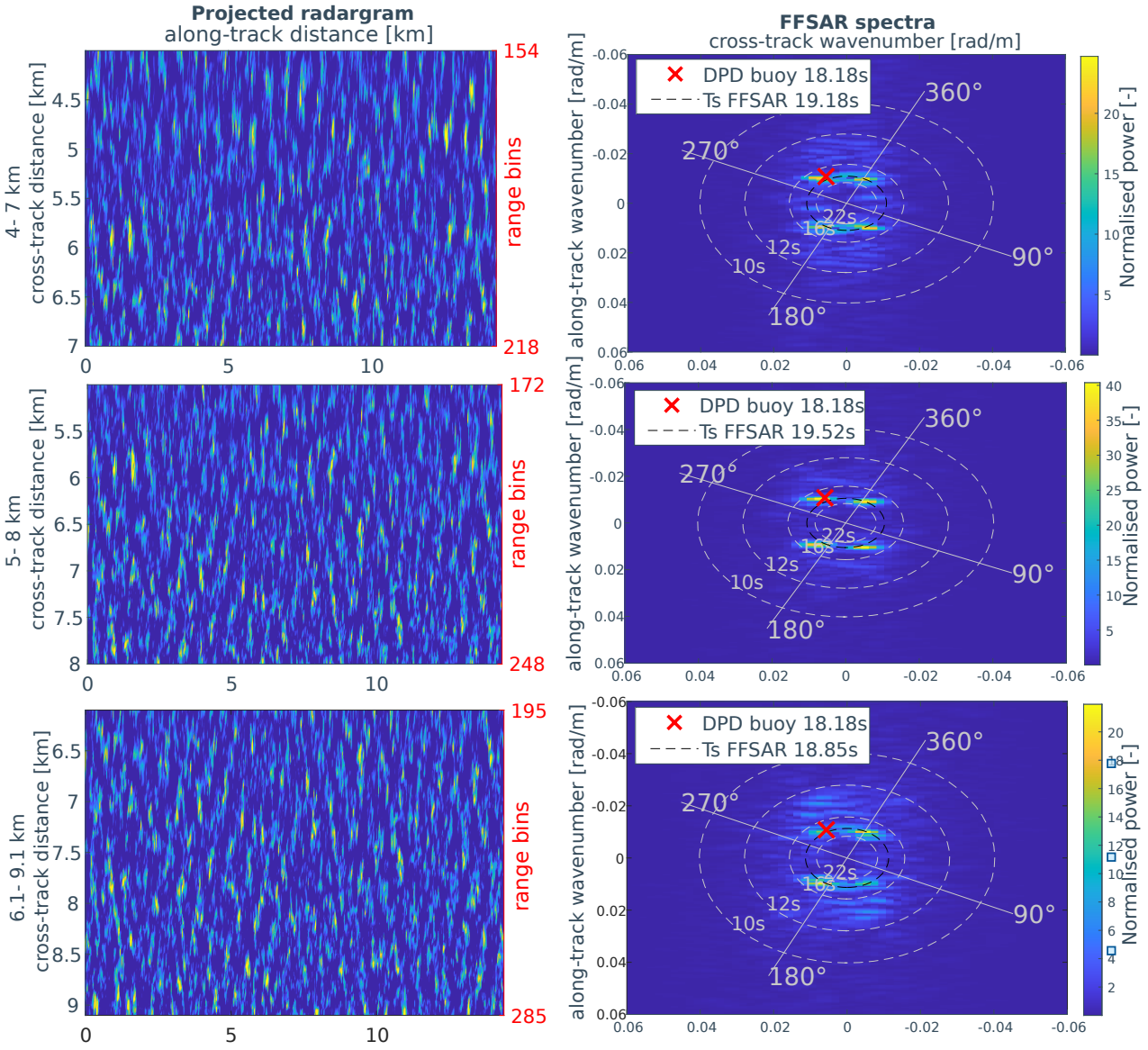

Figure 4.5: Projected radargrams (left) and relative FFSAR spectra (right) retrieved by pass 206 of S6 over the AOI on 28.10.2021. (WSPD= 2.4 m/s, SWH= 2.7 m) for 3 different RMC across-track windows

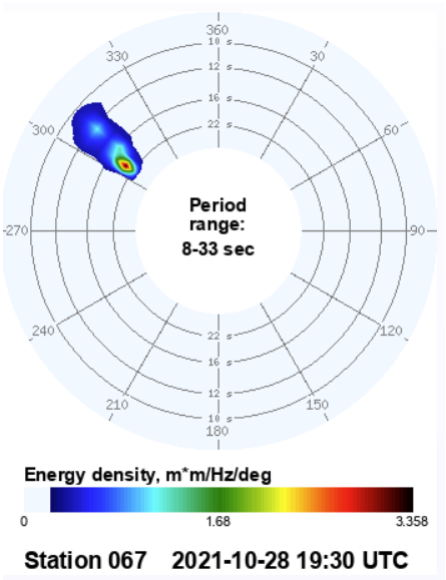

Figure 4.6: Wave spectra collected by buoy 46219 on 28.10.2021 at the time of the satellite observation. A single energy peak for swell waves is observed (Coastal Data Information Program (CDIP), 2021)

4.2.3. Discussion of the sensitivity analysis

There are some common observations that can be highlighted for both the raw and RMC cutting window sensitivity analysis, which are summarised in Table 4.5.

Table 4.5: raw and RMC cutting window sensitivity analysis summary

	Cutting window limits [km]	T_s MAE [s]	Sample size [n passes]
raw	4-10	2.73	66
	6-12	2.24	66
	8-14	1.98	66
	7-13	1.87	67
	7-13.5	1.77	66
RMC	4-7	3.3	68
	5-8	3.03	67
	6-9	2.92	67
	6.1-9.1	2.75	68
	6.2-9.2	2.83	69
	6.3-9.3	2.85	65
	6.4-9.4	3.42	65

The first thing to be noted is the similarity between MAEs within the raw or RMC intervals: the sensitivity analysis did not yield clear ”winners”. Buoy 46219 has an accuracy of 3% of the measured period (Table 3.4) which, for the considered data set, ranges between 0.35 and 0.6 seconds. When considering the buoy error range in the sensitivity analysis, the resulting MAE ranges of many intervals would overlap. It would be therefore wise to consider an increased sample size (as pointed out by recommendation **RC-1**) to make the sensitivity analysis more robust, as it was also observed that adding or removing a pass changed each interval's MAE significantly. Another point of attention is that the worse interval for retrieval is located towards the leading edge in both cases, while the best window is the one that gets closest to the last bin, without including the very last portion of the respective waveforms which in both cases are badly normalised by the chosen polynomial. Looking at the best performance, it can be seen that the best cutting window for raw waveforms leads to a MAE that is one full second lower than the one of RMC, while the best combination for RMC waveforms is outperformed by all proposed raw sensitivity settings. This is expected, as overall a longer (2x long) across-track window is used to generate FFSAR raw spectra. Finally, the sample size varies for each considered window size as out of the 70 passes with swell available in the given period, some were compromised (as explained in Section 4.1). Not all the compromised passes interfered with the retrieval of the swell period from the FFSAR spectra (except for the pass on 25.05.2022 where retrieval was not possible with any interval). For instance, the data collected by S6 on 20.08.2021 seems to have provided working spectra for all RMC cutting windows, while swell period retrieval was not possible using raw data. This indicates that the radargram quality on 20.08.2021 improved in the latitude interval where RMC data is collected. Overall however, raw and RMC waveforms seem to have been equally impacted as the sample size is quite similar for all ranges considered (ranges between 65 and 69) and the excluded passes are mostly the same for both raw and RMC. It should be however considered, that even when some compromised data led to an acceptable estimate of swell period from FFSAR, both raw and RMC intervals performed worse than the given interval MAE on those dates.

4.2.4. Changing the cutting window along-track width (wmin, wmax)

An in-depth sensitivity analysis was not performed on the parameters *wmin* and *wmax*, which define the waveforms that are selected along-track to generate spectra. Instead, a range of different values for *wmin* was considered, in combination with the originally proposed along-track window width of 14.5 km

and a smaller width of 6.5 km, corresponding to the across-track window width for the best raw interval: 7-13.5 km. This allows us to investigate the effect of using a smaller cutting window (6.5 x 6.5 km for raw data). Also for this analysis, the data was filtered for the presence of swell. The results can be seen in Table 4.6 for the across-track combinations found to work best in the sensitivity analysis. For this investigation, compromised passes were removed in case of failed raw and RMC FFSAR swell period retrievals, leading to a slightly different value of MAE for the RMC 6.1-9.1 km waveforms (compared to the one reported in Table 4.5) as one less pass was available due to a failure in parameter retrieval from raw waveforms on that pass.

Table 4.6: Mean Absolute Error for raw and RMC swell period retrievals obtained from radargrams located at different points along-track, with two principal window widths of 6.5 and 14.5 km. The across-track projection limits were set to the best setting found in the sensitivity analysis: 7-13.5 km for raw and 6.1-9.1 km for RMC waveforms. Highlighted: best raw and RMC performances, bold: best combined average performance.

along-track window width →	**6.5 km**		**14.5 km**	
wmin [km] ↓	**MAE raw [s]**	**MAE RMC [s]**	**MAE raw [s]**	**MAE RMC [s]**
5.8	2.00	2.83	2.12	2.77
11.5	1.98	2.61	2.05	2.55
20	1.95	2.92	1.77	2.75
26	**1.95**	**2.85**	1.90	2.97
31.7	1.78	2.45	out of bounds	
average MAE	1.93	2.73	1.96	2.79

In Table 4.6, only intervals starting after wmin = 5.8 km from the beginning of the raw/ RMC latitude interval were considered, as the presence of the transition zone disturbed the signal of the first raw waveforms in ascending passes (track 119) and of the first RMC waveforms in descending passes (track 206). The first thing that can be observed looking at the MAE values, is that the performance of all the along-track window widths is quite similar (when accounting for that the buoy accuracy ranges from 0.35 to 0.6s), with a slight improvement in average MAE of both raw and RMC retrievals for the shorter window of 6.5 km. Smaller windows feature waveforms from a more restricted area, which should therefore be more coherent, as the sea state should have smaller changes over 6.5 km than it does over 13, this could be a reason for the improvement. The best RMC performance corresponds to a window stretching from 31.7 to 38.2 km from the RMC interval starting point, while the best raw performance is obtained with the same settings used in the across-track sensitivity analysis (wmin = 20 km, width = 34.5 km). Overall, an improvement in computational time was noted when running the analysis for the narrower window: for the 70 passes considered, the time of execution for the processing of 6.5 km along-track was 2 min and that of 14.5 km was 3.5 min which is not a significant difference given the sample size considered but should be taken into account for growing sample sizes. These results highly depend on the effect that the mode transition has on different sections of each radargram. Overall, as mentioned in Section 4.1, a drop in signal power was observed in the proximity of the transition latitude.

In order to optimise the performance of both raw and RMC retrievals, it would be necessary to choose different along-track cutting windows for each analysis (see **RC-6** in Chapter 6), or more ideally (**RC-1**) analyse data from a same area. In this case, the same cutting window along-track needs to be applied to both raw and RMC to guarantee a fair assessment of parameter retrieval performance, therefore a single combination has to be chosen out of those proposed in Table 4.6 for the final performance analysis in Section 4.3. As a first thing, the along-track window width was chosen to be 6.5 km as it led to the lowest *average* MAE values for both raw and RMC (1.93 s for raw, 2.73 s for RMC). Among the different values of wmin explored for this window width, wmin = 26 km leads to MAE values closest to the average for both raw and RMC. This is considered to be the best combination to undergo further analysis, as it represents well the combined average performance of raw and RMC while guaranteeing a good retrieval quality for both. With both the across-track and along-track window limits investigated in the past sections, a conclusion can be made about the best choice of window location and dimension for raw and RMC radargrams:

The best overall performance for FFSAR swell period retrieval is achieved for a cutting window stretching across-a track from 7 to 13.5 km for raw and from 6.1 to 9.1 km for RMC, and along-track from 26 to 32.5 km from the start of the considered raw/ RMC latitude interval

4.3. Performance analysis on swell period estimation

Using the most optimal FFSAR spectra generation settings found in Section 4.2, namely a cutting window extending across-track from 7 to 13.5 km for raw and 6.1 to 9.1 km for RMC with 6.5 km of along-track width, the swell period estimates from raw and RMC FFSAR spectra could be collected, together with buoy data (wave height, wind speed, wind direction). The dataset was subset as described in Section 4.1. Passes where station 46219 recorded a period lower than 9 seconds were removed from the analysis. While in the sensitivity analysis, this value was set to 10s, for the performance analysis it was desirable to highlight the effect of lower period waves on the FFSAR parameter retrieval. This resulted in a sample size of 75 passes. A FFSAR spectrum obtained using the final cutting window is illustrated in Figure 4.7, where it can be clearly seen how the cutting window is square in the case of raw data (top row), while the RMC projected radargram is wider along-track and leads to a spectrum where multiple high power signals are observed, apart from the ones originating from the SAR ambiguity and altimeter symmetry explained in Figure 2.3.3. The complete overview of buoy and satellite parameters for the sample is provided in

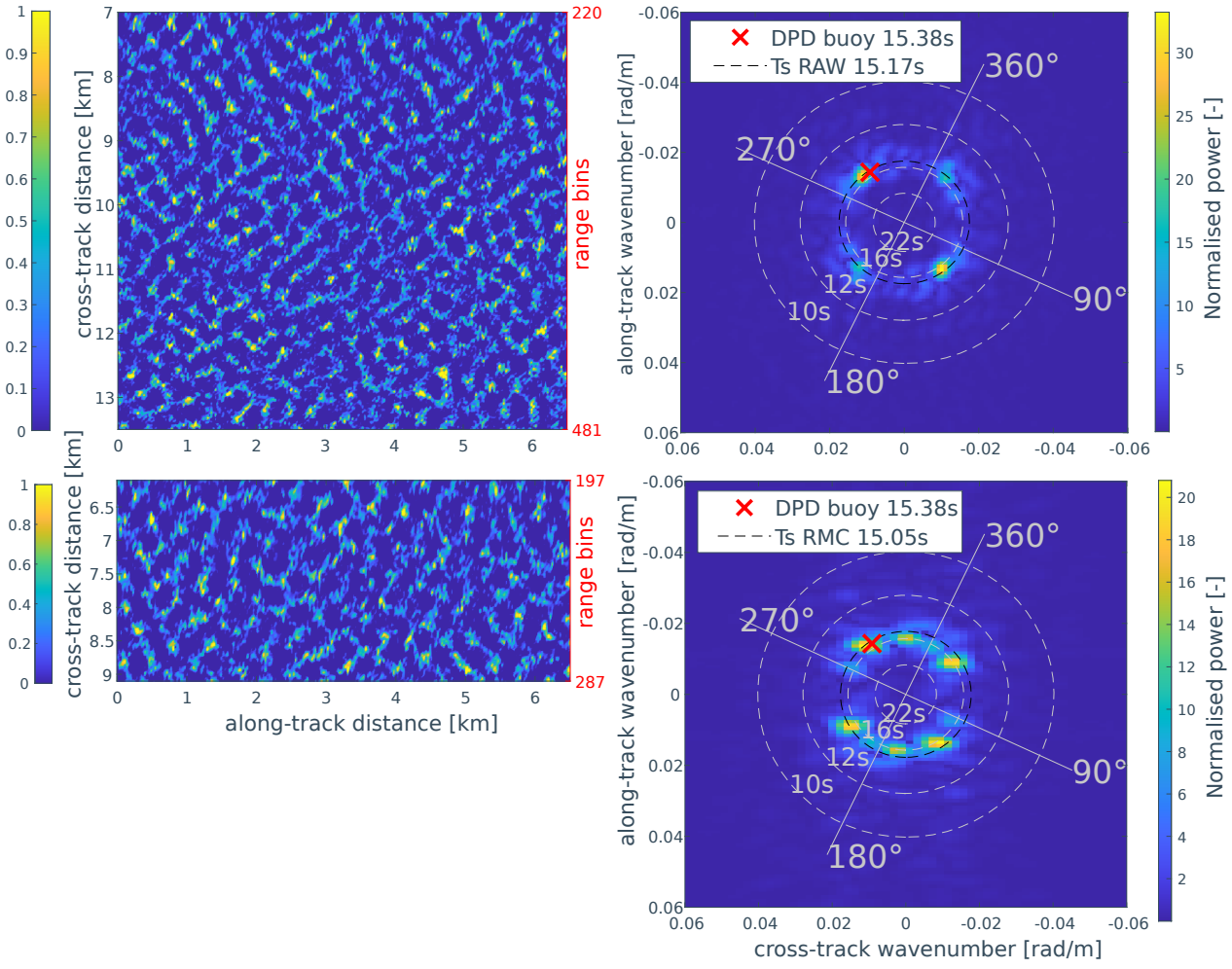

Figure 4.7: Projected radargram and corresponding FFSAR spectra collected by S6 over segment 2 on 27.22.2021. Top: raw, bottom: RMC

Table B.3. In Figure 4.8, the swell period T_s obtained from the FFSAR spectra using Equation 3.1 on raw and RMC waveforms is compared to the peak wave period retrieved by buoy 46219 for each pass. On the left of the figure, the entire dataset is considered, while the plots in the centre and on the right were obtained by considering only values where the FFSAR raw or RMC estimate was within 2σ or 1σ from the respective MAE value computed for the full sample. This 1 and 2σ analysis allows us to see the impact of outliers on the dataset: it is clearly seen that most of the raw and RMC retrievals corresponding to

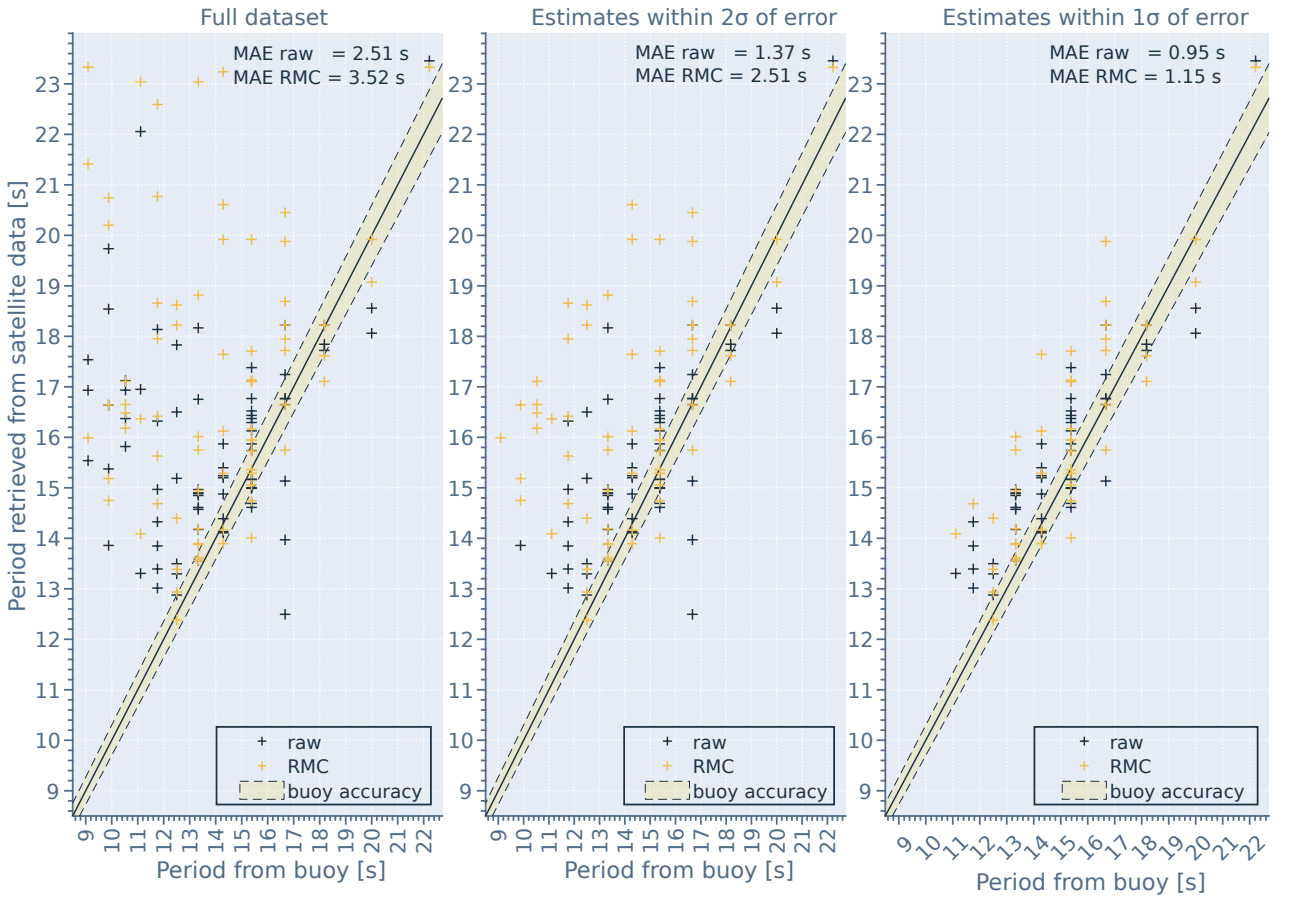

Figure 4.8: Raw and RMC FFSAR swell period estimate compared to buoy data for all passes (left), passes where the FFSAR period estimate was within 2σ from the mean error (centre) and within 1σ (right). Yellow: RMC data, blue: raw data, shaded area: buoy accuracy interval

passes where a lower wave period was detected from the buoy turned out to be outliers. The MAE values corresponding to each plot and dataset are reported in Table 4.7).

Table 4.7: Mean Absolute Errors of FFSAR estimates of swell period T_s from raw and RMC waveforms in the optimal cutting window. MAE values are reported for the original dataset and for the data points within 2σ and 1σ of the mean raw/ RMC difference

	Full dataset	**2σ datapoints**	**1σ datapoints**
MAE raw T_s [s]	2.51	1.37	0.95
MAE RMC T_s [s]	3.52	2.51	1.15

Due to the consideration of the 1σ and 2σ intervals, the MAE drops significantly for both raw and RMC spectra: the raw error is consistently lower than the RMC error, but for the 1σ analysis, both have a very small error of about 1 s. The buoy accuracy of platform 46219 (shaded yellow area in the figure) is quite high and inversely proportional to the period measured ($\pm 3\% DPD$). Most buoys from the NDBC network however (like buoy 46047), have a lower accuracy of ± 1 s, which is very close to the 1σ MAE values of both raw and RMC period estimates: this is promising, as it would mean that if RMC data generation will continue to be implemented in the upcoming altimetry missions, swell period estimation would be successful within a 1σ confidence interval. The difference with raw performance becomes irrelevant for such an interval, as it is smaller than the buoy accuracy.

Before further analysing the performance plot, it is necessary to acknowledge a few things about the dataset used:

- The sample size used is considerably small (< 100 samples) and is therefore very sensitive to the presence of outliers.

- The buoy measurements have a limited directional variability (in terms of swell travel direction): most swell systems observed in the considered time frame originate from West - North-West. This is visualised in Figure 4.9, where the MWD of each pass is plotted in the angular direction while the period recorded on such pass is plotted in the radial direction.

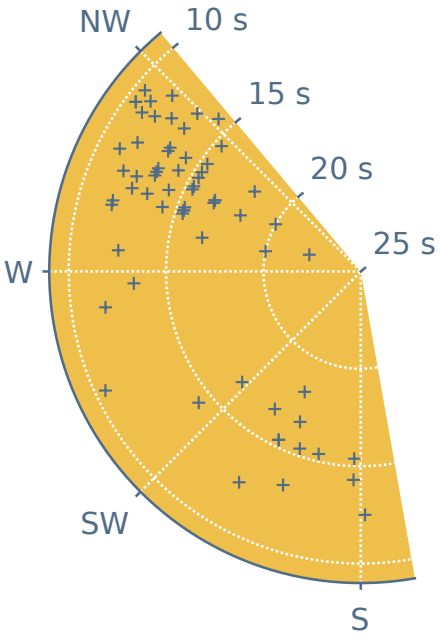

Figure 4.9: Directional distribution of the dataset: swell direction detected from the buoy for each timestamp considered; peak wave period is shown on the radial axis

- The period retrieved from the FFSAR spectra is only a first estimate of the swell period, as a spectra inversion to wave spectra is still not possible for FFSAR. The highly non-linear imaging effects described in Subsection 2.3.1 together with the dependency of such mechanisms on sea state, make it challenging to identify the sources of discrepancy between the FFSAR and ocean wave spectra.

From Figure 4.8, it can be seen that both raw and RMC spectra overestimate the swell period, especially for passes with a short wavelength. This is expected and can be related to the presence of a high cutoff wavelength: due to the smearing of the image caused by destructive velocity bunching, shorter wavelengths do not leave a trace in the FFSAR spectra. The overestimation is also clear in Figure 4.10. Only for

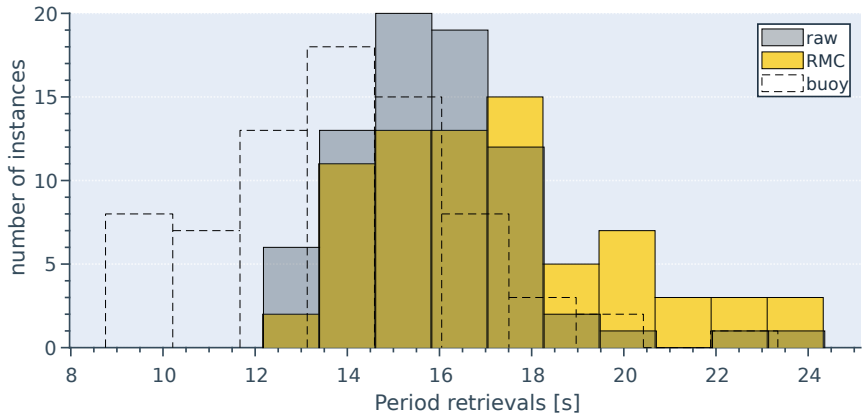

Figure 4.10: Histogram showing the distribution of period measurements performed by the buoy and period estimates from FFSAR raw and RMC spectra

a couple of raw passes where the buoy records a period of ~17 s, the FFSAR spectra period estimate is lower than that of the buoy. These specific passes (segment 2, 20.08.2021 and segment 1, 18.08.2022) were therefore investigated and it was found that the underestimation of the period from segment 2 was most likely due to a high misalignment in the leading edge of the waveforms in the considered latitude

interval, which was observed in the original FFSAR radargram. The FFSAR L1B data of segment 1 on 18.08.2022 on the other hand did not display anything unconventional. When looking at the FFSAR spectra however, (see Figure 4.11) a smearing in the projected radargram can be observed. This could be tied to the direction of the swell, which for this specific case diverges from the rest of the observations as the system originates from South - South-East and has, therefore, a bigger azimuthal wavenumber which degrades the resolution due to the high impact of non-linear velocity bunching effects on higher along-track wavenumbers. As noted above, the data sample is not large enough to make a statistically significant analysis on this, as only a few samples feature such swell directions. To better visualise the

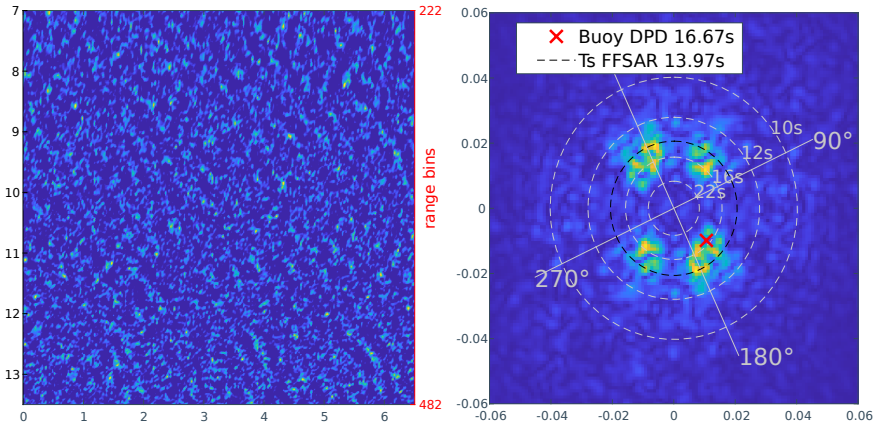

Figure 4.11: Projected radargram and raw FFSAR spectra collected by S6 over segment 1 on 18.08.2022

relationship between the raw and RMC performance and the recorded wave period, the swell period estimation error of raw and RMC is compared to the peak period measured by buoy 46219 on the right panel of Figure 4.12. It can be clearly seen that for higher measured periods, both raw and RMC perform better

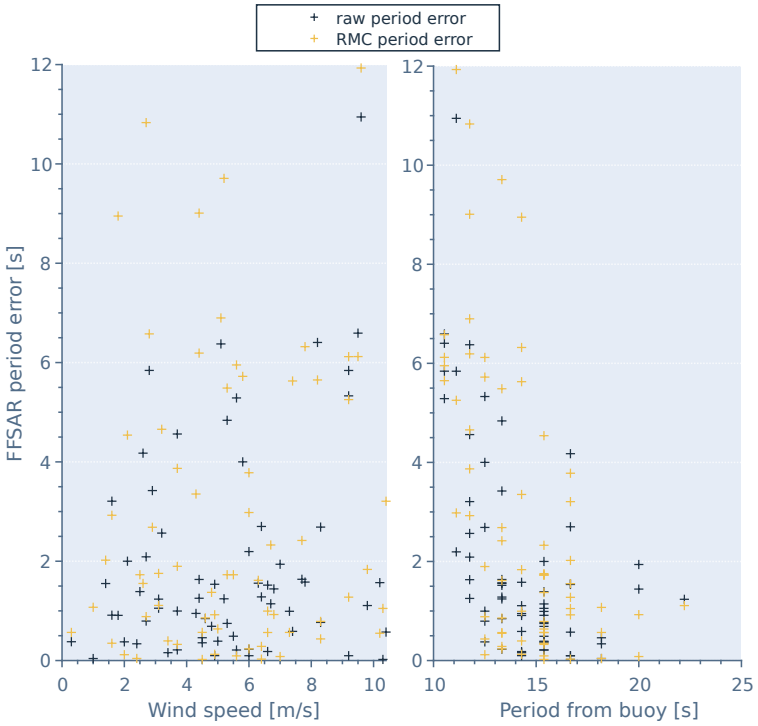

Figure 4.12: FFSAR period error vs wind speed and buoy period

(lower error). An increase in performance for stronger swells is to be expected due to velocity bunching being constructive for longer wavelengths (so leading to an FFSAR spectrum that is more similar to the wave spectrum). Again, in order to define a trend, it would be necessary to gather more data, especially for very strong swells, as most peak periods measured around 14s (this is seen in Figure 4.10, where the buoy measurements are shown in the dashed histogram). A recommendation is made about this (see

RC-7: in Chapter 6).

The left panel in Figure 4.12 shows the absolute error variation for each pass with windspeed. This was plotted with the aim of understanding if the windspeed affected the error in swell period estimates from FFSAR raw and RMC spectra. For each measured windspeed for each pass, a pair (raw, RMC) of data points is visualised: each pair with the same value and a different y-value corresponding to the respective period estimation error. Usually, a higher windspeed is not desirable as it negatively impacts the azimuth cutoff wavelength, making it harder for SAR instruments to retrieve wave parameters (as explained in Subsection 2.3.1). In this case, no correlation can be observed between the variation in wind speed and the performance of FFSAR swell period retrievals: for both raw and RMC retrievals, it can be seen that the magnitude of the errors is evenly distributed for different wind speeds. This can be due to the fact that overall, the wind measured for the considered time period is always less than 10 m/s and therefore not particularly strong.

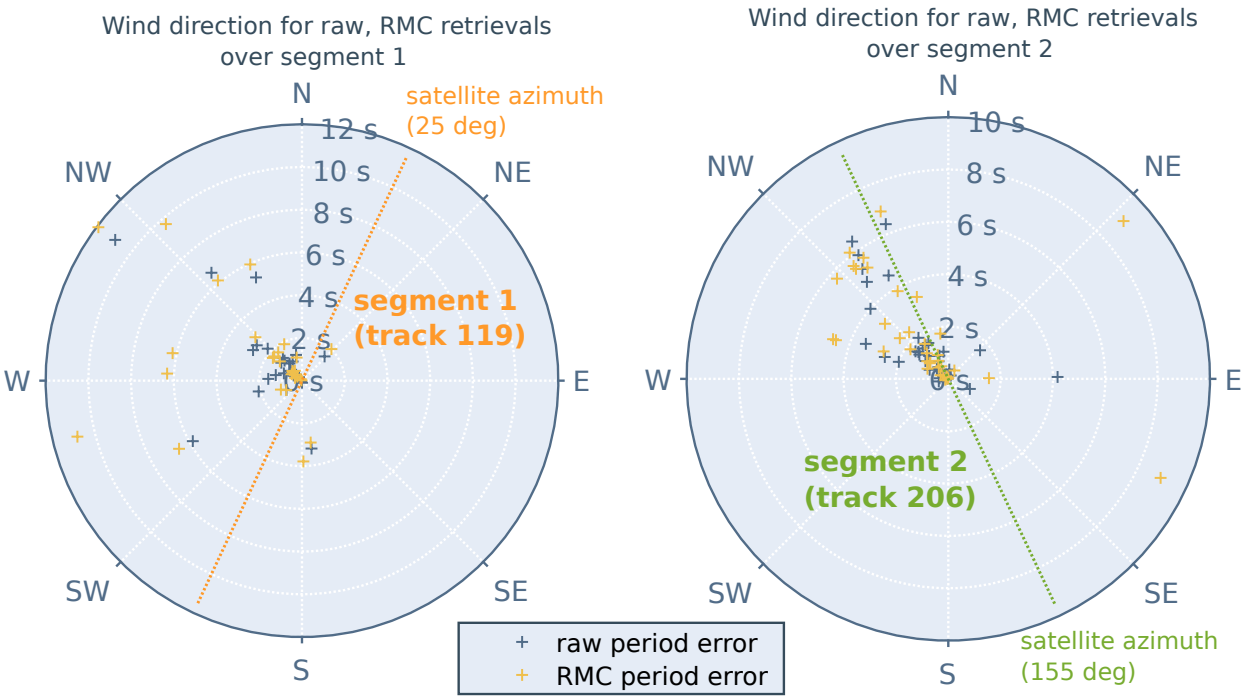

Figure 4.13: Wind direction vs period error

The FFSAR error variation with wind direction was also investigated to support the performance analysis. In Figure 4.13, the dataset is divided between samples collected over segment 1 (left, 33 data points) and segment 2 (right, 42 data points). This allows to determine the direction of the wind concerning the satellite azimuth for the given track. The wind direction is plotted in polar plots, with the FFSAR period estimate error increasing in the radial direction for the respective raw and RMC retrievals. The first thing to be noted is that also in this case, there is a directional distribution of the dataset: the wind predominantly comes from North West. When comparing the wind direction with the orientation of the two satellite segments, one can see that the wind mostly comes across-track for segment 1 and along-track for segment 2. To better see the wind direction and error distribution, Figure 4.14 can also be considered.

To quantify the relative performance of raw and RMC period estimates for these different swell and wind directions, the MAE values corresponding to the different segments are reported in Table 4.8.

Table 4.8: Mean Absolute Errors of FFSAR estimates of the swell period from raw and RMC waveforms for segment 1 and segment 2

	segment 1	**segment 2**
MAE raw T_s [s]	2.65	2.40
MAE RMC T_s [s]	3.87	3.24

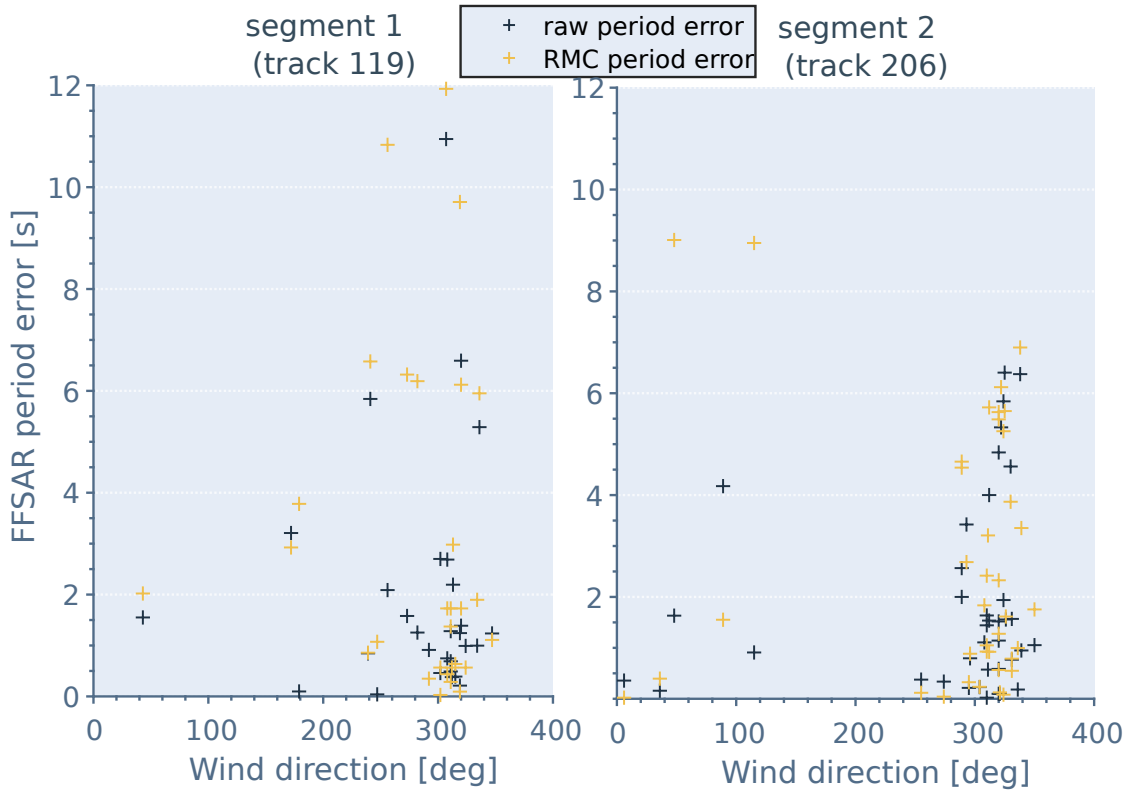

Figure 4.14: Wind direction vs period error

It can be seen that both modes perform better when wind and waves move along-track, in particular, the improvement concerning the RMC retrievals is slightly higher than that of RAW, but considering that the buoy accuracy is on average $\pm 0.45s$, the difference in improvement is not significant.

For the considered dataset, for winds moving along-track, the waves seem to be imaged better. As seen in Subsection 2.3.1, different modulations are responsible for the imaging of waves coming from along or across-track: while velocity bunching is the dominant imaging mechanism for waves travelling along-track, range bunching allows for waves travelling cross-track to be imaged. As the wind directional distribution is very similar to the swell directional distribution and swell also travels mainly along-track for segment 2, with a bigger dataset, it could be confirmed that velocity bunching is the dominant imaging mechanism for altimetry spectra. This would be in contrast with previous observations by Altiparmaki et al. (2022), which concluded that range bunching was dominant. It should be noted that due to the low wind-speed in the considered sample, it could be that velocity bunching is mainly constructive and image-smearing effects caused by movements typical of shorter, wind waves are limited. However, these discrepancies should be further investigated with a bigger dataset where strong swells coming from along and across-track can be considered.

5 Conclusions

Given the newly discovered potential of satellite Synthetic Aperture Radar altimetry data to contribute to the monitoring of swell waves from space, and the presence of a new on-board compression mode on the latest SAR altimetry mission: Sentinel-6, a thesis work to investigate the impact of such compression on swell parameter retrieval was carried out to answer the following research question:

> Does the truncation of waveforms performed by the RMC algorithm on board Sentinel-6 affect the potential of retrieving swell wave parameters from FFSAR spectra?

The relevance of this query is tied to the added value that a global ocean coverage such as the one provided by Sentinel-6 could provide to the growing database of swell measurements. Characterising swell is fundamental for the coastal communities threatened by inundations, for modelling the climate system and for weather monitoring.

To answer this question, Sentinel-6 FFSAR waveforms were collected for two satellite tracks in the proximity of the JPL calibration area in the Channel Islands of California, where the swell is present and raw and RMC waveforms, together with in-situ data, are available. Buoy 46219 from the NDBC network was found to be an appropriate source of period measurements while buoy 46047 was used to retrieve wind data. The period estimates were extracted from the FFSAR spectra using the wavenumbers of the point of highest normalised power. The Mean Absolute Error of the satellite swell periods concerning the buoy peak period was found to be a suitable metric for assessing the performance of the raw and RMC operating modes in estimating the swell period. It was noticed that the presence of a transition area between operational modes made it necessary to pre-process the data set to exclude passes impacted by such mode switches.

A sensitivity analysis on the portion of waveform to be considered across-track for spectra generation revealed that the best intervals for both raw and RMC echoes lie towards the trailing edge (tail) where the range resolution is highest. In particular, projection limits of 7-13.5 km and 6.1-9.1 km were found to work best for raw and RMC modes respectively. These results were also dependent on the fitting polynomial employed. The width and position of the window along-track were also varied to find the most optimal settings among the given options. It was concluded that a 6.5 km-wide window along-track, cut within the mentioned projection limits across-track, is the best combination of settings to evaluate the performance of FFSAR raw and RMC parameter retrieval. This is a square cutting window for raw data: it was observed that a shorter window width along-track performs better, as waveforms are more coherent within a smaller interval.

Having defined the most suitable settings to limit the across and along-track dimensions of the projected radargrams, the corresponding FFSAR spectra were computed for both raw and RMC waveforms, and the relative swell period estimates were retrieved and compared with buoy data. Overall, both raw and RMC retrievals consistently overestimated the period observed by the buoy, especially for passes where a lower swell period was observed. This was expected, as velocity bunching smears the resolution along-track, resulting in a high cut-off wavelength. The Mean Absolute Error of the raw swell period estimates was found to be consistently lower than RMC both for the final performance analysis and for the sensitivity runs with sub-optimal settings. When excluding passes where the error was 1σ and 2σ from the mean,

the difference between the raw and RMC MAE dropped significantly (MAE raw = 0.95, MAE RMC = 1.15 at 1σ), resulting in a value that is neglectable as it is lower than the buoy accuracy. This demonstrated that also RMC FFSAR data from altimeters data has the potential to be used to estimate swell period within a 1σ confidence interval.

It was also noticed that the dataset considered has a directional distribution of wind and swell, with swell coming predominantly from West - North-West, with period measurements distributed normally around a mean of 14s, while wind the mean direction from North West. It was seen that, for wind and waves travelling in the azimuth direction (along-track), a lower error in the FFSAR period estimate was encountered, especially for RMC tracks. This finding is in contrast with previous observations about the dominance of range bunching as a modulator of FFSAR altimetry spectra, but it should be noted that the wind speed for the analysis at hand was always below 10 m/s, therefore the non-linear effects of velocity bunching induced by random motions of shorter waves are limited, and more constructive velocity bunching can take place.

Overall, it can be said that the retrieval of the swell period from FFSAR spectra derived from Sentinel-6 data is impacted by the presence of compressed (RMC) data, however, estimating the swell period is still possible, especially for strong swells travelling along-track. Using raw waveforms for swell parameter retrieval has the inherent advantage of featuring a complete trailing edge with higher usable range resolution. Should altimetry further be investigated as a source of swell data, the need for the higher performance provided by raw spectra estimates would be limited to coastal oceanic areas that are particularly impacted by the presence of swell and would therefore benefit from the reduced error in the swell period estimate. Future altimetry mission designs could benefit from activating a raw-acquisition mode over such areas.

6

Recommendations

This section will discuss the steps to be considered for future work. Most recommendations have been introduced in the previous chapters, as they followed directly from the analysis of the results.

- **RC-1:** As the main assumption in this thesis is about the use of raw and RMC data from adjacent areas for comparison, it is important to make a recommendation in this regard. In order to reduce the differences between raw and RMC data to the ones caused by factors related to the waveform cutting, raw and RMC waveforms collected over the same area should be considered. For this analysis, data collected during cycles 25-27 during the mission commissioning phase should be retrieved and analysed.
- **RC-2:** The normalisation of the waveforms is a fundamental step in the process leading to the final spectra, as it is the normalised projected waveforms that constitute the radargrams from which the spectra are obtained. The choice of the polynomial to be fitted on the original waveform to generate the normalised data is therefore crucial. A dedicated polynomial should be used to ensure a fit that spans over a bigger portion of the waveform compared to the current solution. A different polynomial order or another model might be more suitable for the normalisation of raw waveforms in particular.
- **RC-3:** Currently, only the point of maximum power in the FFSAR spectra were considered to retrieve the swell period. For a more complete investigation of the correlation between FFSAR and wave spectra, secondary power peaks in power should also be considered for swell period retrieval: a secondary period could then be compared to respective secondary peaks visible in wave spectra retrieved by buoy data.
- **RC-4:** Considering the reduced sample size available at the time of this study and the lack of robustness of the sensitivity analysis associated with it, a reduced number of across-track window combinations was considered. However, should a bigger sample of data become available for comparison, a systematic optimisation of the cutting window limits for the waveforms projection across-track should be considered, to find the best limit combination for both raw and RMC waveforms. This can be achieved by iterating through multiple combinations until the lowest Mean Absolute Error is reached. Multiple optimisation/ minimisation algorithms can be employed for this purpose, depending on the sample size and computational power available.
- **RC-5:** While in this elaborate, only a couple of options were considered for the width of the cutting window along-track, systematic optimisation of the cutting window width for the waveforms projection across-track should be considered, to find the best width for both raw and RMC waveforms. This can be achieved by iterating through multiple combinations until the lowest Mean Absolute Error is reached.
- **RC-6:** The research objective constrained the choice of a common along-track window position and width for both raw and RMC intervals. In case of an analysis where the comparison of raw and RMC performance is not the goal, the choice of latitude interval to be used for spectra generation (along-track cutting window), should be made separately for raw and RMC, to achieve the best performance in parameter retrieval for each dataset.
- **RC-7:** The study area considered and the limited availability of data at the time of this study led to a small sample size which limited the possibilities of statistical analysis. It would be ideal for bigger-scale investigations to employ data sets featuring a higher directional distribution of swell and wind

measurements.

Further recommendations can be made regarding for instance the **FFSAR processor and its settings**. The comparison of the quality of swell retrievals using different FFSAR processing algorithms could be a study by itself and was therefore considered outside the scope of this research, however, it would be recommendable to explore the outcomes obtained when processing RMC waveforms with a back-projection algorithm. When it comes to processor settings, the multi-look posting rate is another interesting parameter that can be tuned to observe its effect on the analysis: as also suggested by literature (Egido et al., 2021), higher posting rates lead to better results due to the reduced noise, however, as the resolution along-track decreases, it would be valuable to investigate the use of different posting rates for swell detection.

The choice of **validation data** was driven for practical reasons towards the use of buoy measurements, however, it would be valuable to diversify the validation data pool with data originating from models, for instance, the CMEMS wave model or from other satellite platforms like Sentinel-1, Sentinel-2 or the Level-2 products of the SWIM spectrometer on board of the CFOSAT mission. This last option would allow a comparison of S6 data with another satellite product: both the 2D ocean spectra and the radargrams used to produce them would be available for analysis. In the case of employing CFOSAT data, care should be taken in ensuring that the time difference between observations at ground tracks crossover points would be acceptable.

Another note about the use of validation data concerns its timeliness: for the first months of 2023, only real-time buoy data was available, while the use of historical data is recommended wherever possible, due to its higher reliability. One last recommendation can be made within this topic, and it is about the buoy parameter choice. While the current method utilizes the peak period to filter for days where the swell is present, it would be preferable to retrieve also the swell period measurements from buoy data. This would allow us to consider timestamps when swell waves are observed by the satellite, and buoy spectra feature both wind and swell wave groups with swell waves having lower energy. Furthermore, in the case where two swell systems with different energies are observed by the buoy for a given timestamp, getting access to both the peak period and the swell period can provide a better comparison to satellite spectra, which might only show the higher period wave group. If the analysis of the swell period is contemplated, it should be noted that for NDBC, it is only available for recent (real-time) measurements and should therefore be downloaded periodically.

Bibliography

S. Abdalla, A. Abdeh Kolahchi, M. Ablain, et al. Altimetry for the future: Building on 25 years of progress. *Advances in Space Research*, 68(2):319–363, 2021. ISSN 0273-1177. doi: https://doi.org/10.1016/j.asr.2021.01.022. URL https://www.sciencedirect.com/science/article/pii/S0273117721000594. 25 Years of Progress in Radar Altimetry.

W. Alpers and K. Hasselmann. The two-frequency microwave technique for measuring ocean-wave spectra from an airplane or satellite. *Boundary-Layer Meteorology*, 13(1):215–230, Jan 1978. ISSN 1573-1472. doi: 10.1007/BF00913873. URL https://doi.org/10.1007/BF00913873.

W. Alpers and C. Rufenach. The effect of orbital motions on synthetic aperture radar imagery of ocean waves. *IEEE Transactions on Antennas and Propagation*, 27(5):685–690, 1979. doi: 10.1109/TAP.1979.1142163.

W. R. Alpers, D. B. Ross, and C. L. Rufenach. On the detectability of ocean surface waves by real and synthetic aperture radar. *Journal of Geophysical Research: Oceans*, 86(C7):6481–6498, 1981. doi: https://doi.org/10.1029/JC086iC07p06481. URL https://agupubs.onlinelibrary.wiley.com/doi/abs/10.1029/JC086iC07p06481.

O. Altiparmaki, M. Kleinherenbrink, M. Naeije, C. Slobbe, and P. Visser. Sar altimetry data as a new source for swell monitoring. *Geophysical Research Letters*, 49(7):e2021GL096224, 2022. doi: https://doi.org/10.1029/2021GL096224. URL https://agupubs.onlinelibrary.wiley.com/doi/abs/10.1029/2021GL096224. e2021GL096224 2021GL096224.

J.-H. G. Alves. Numerical modeling of ocean swell contributions to the global wind-wave climate. *Ocean Modelling*, 11(1):98–122, 2006. ISSN 1463-5003. doi: https://doi.org/10.1016/j.ocemod.2004.11.007. URL https://www.sciencedirect.com/science/article/pii/S1463500305000028.

P. Aouf. On the signature of swell for the cryosat-2 sar-mode wave data. OSTST Meeting 2015, Reston, Virginia, USA, 10 2015. URL hhttps://meetings.aviso.altimetry.fr/fileadmin/user_upload/tx_ausyclsseminar/files/OSTST2015/IPM-02-ostst_Aouf_sarmode_2015_1.pdf.

F. Ardhuin, B. Chapron, and F. Collard. Observation of swell dissipation across oceans. *Geophysical Research Letters*, 36(6), 2009. doi: https://doi.org/10.1029/2008GL037030. URL https://agupubs.onlinelibrary.wiley.com/doi/abs/10.1029/2008GL037030.

F. Ardhuin, J. Stopa, B. Chapron, F. Collard, M. Smith, J. Thomson, M. Doble, B. Blomquist, O. Persson, C. O. Collins, and P. Wadhams. Measuring ocean waves in sea ice using sar imagery: A quasi-deterministic approach evaluated with sentinel-1 and in situ data. *Remote Sensing of Environment*, 189:211–222, 2017. ISSN 0034-4257. doi: https://doi.org/10.1016/j.rse.2016.11.024. URL https://www.sciencedirect.com/science/article/pii/S0034425716304710.

F. Ardhuin, J. E. Stopa, B. Chapron, F. Collard, R. Husson, R. E. Jensen, J. Johannessen, A. Mouche, M. Passaro, G. D. Quartly, V. Swail, and I. Young. Observing sea states. *Frontiers in Marine Science*, 6, 2019. ISSN 2296-7745. doi: 10.3389/fmars.2019.00124. URL https://www.frontiersin.org/articles/10.3389/fmars.2019.00124.

A. V. Babanin, A. Ganopolski, and W. R. Phillips. Wave-induced upper-ocean mixing in a climate model of intermediate complexity. *Ocean Modelling*, 29(3):189–197, 2009. ISSN 1463-5003. doi: https://doi.org/10.1016/j.ocemod.2009.04.003. URL https://www.sciencedirect.com/science/article/pii/S1463500309000857.

M. Bao and W. Alpers. On the cross spectrum between individual-look synthetic aperture radar images of ocean waves. *IEEE Transactions on Geoscience and Remote Sensing*, 36(3):922–932, 1998. doi: 10.1109/36.673683.

K. R. Barnhart, I. Overeem, and R. S. Anderson. The effect of changing sea ice on the physical vulnerability of arctic coasts. *The Cryosphere*, 8(5):1777–1799, 2014. doi: 10.5194/tc-8-1777-2014. URL https:

//tc.copernicus.org/articles/8/1777/2014/.

F. Boy, J.-D. Desjonqueres, N. Picot, T. Moreau, and M. Raynal. Cryosat-2 sar-mode over oceans: Processing methods, global assessment, and benefits. *IEEE Transactions on Geoscience and Remote Sensing*, PP:1–11, 09 2016. doi: 10.1109/TGRS.2016.2601958.

G. Brassington. Mean absolute error and root mean square error: which is the better metric for assessing model performance? In *EGU General Assembly Conference Abstracts*, EGU General Assembly Conference Abstracts, page 3574, Apr. 2017.

M. F. Bruno, M. G. Molfetta, V. Totaro, and M. Mossa. Performance assessment of era5 wave data in a swell dominated region. *Journal of Marine Science and Engineering*, 8(3):214, Mar 2020. ISSN 2077-1312. doi: 10.3390/jmse8030214. URL http://dx.doi.org/10.3390/jmse8030214.

M. Casas-Prat and X. L. Wang. Projections of extreme ocean waves in the arctic and potential implications for coastal inundation and erosion. *Journal of Geophysical Research: Oceans*, 125(8):e2019JC015745, 2020. doi: https://doi.org/10.1029/2019JC015745. URL https://agupubs.onlinelibrary.wiley.com/doi/abs/10.1029/2019JC015745. e2019JC015745 10.1029/2019JC015745.

Centre National d'Etudes Spatiales. Delay-Doppler / SAR altimetry, 2017. URL https://www.aviso.altimetry.fr/en/techniques/altimetry/principle/delay-doppler-/-sar-altimetry.html.

T. Chai and R. R. Draxler. Root mean square error (rmse) or mean absolute error (mae)? – arguments against avoiding rmse in the literature. *Geoscientific Model Development*, 7(3):1247–1250, 2014. doi: 10.5194/gmd-7-1247-2014. URL https://gmd.copernicus.org/articles/7/1247/2014/.

Coastal Data Information Program. San nicolas island, ca - 067. CDIP, 4 2023. URL http://cdip.ucsd.edu/m/products/?stn=067p1.

Coastal Data Information Program (CDIP). Cdip faq: The cdip buoys report larger wind waves, while the ndbc buoys report more swell. why is this the case. Coastal Data Information Program, 06 2017. URL https://cdip.ucsd.edu/m/about/faq/.

Coastal Data Information Program (CDIP). Instrumentation: Datawell directional waverider buoy (mark iii). Coastal Data Information Program, 06 2018. URL https://cdip.ucsd.edu/m/documents/instrumentation.html#directional-buoys.

Coastal Data Information Program (CDIP). Station 067 - san nicolas island, ca. polar spectrum for 28.10.2021, 19:30 utc. Coastal Data Information Program, 11 2021. URL http://cdip.ucsd.edu/themes/cdip?zoom=auto&tz=UTC&ll_fmt=dm&numcolorbands=10&palette=cdip_classic&high=6.096&r=999&un=1&pb=1&d2=p70&u2=s:067:st:1:v:polar_plot:max_frq:0.12:dt:202110281930.

Coastal Data Information Program (CDIP). Station 067 - san nicolas island, ca. polar spectrum for 26.11.2022, 01:30 utc. Coastal Data Information Program, 11 2022. URL http://cdip.ucsd.edu/themes/cdip?zoom=auto&tz=UTC&ll_fmt=dm&numcolorbands=10&palette=cdip_classic&high=6.096&r=999&un=1&pb=1&d2=p70&u2=s:067:st:1:v:polar_plot:max_frq:0.12:dt:202211260130:t:plot.

F. Collard, F. Ardhuin, and B. Chapron. Monitoring and analysis of ocean swell fields from space: New methods for routine observations. *Journal of Geophysical Research: Oceans*, 114(C7), 2009. doi: https://doi.org/10.1029/2008JC005215. URL https://agupubs.onlinelibrary.wiley.com/doi/abs/10.1029/2008JC005215.

Collecte Localisation Satellites. Cmems swell monitoring. CLS, 4 2023. URL http://satwave-report.cls.fr/.

P. Craig Kohler, L. LeBlanc, and J. Elliott. Scoop - ndbc's new ocean observing system. In *OCEANS 2015 - MTS/IEEE Washington*, pages 1–5, 2015. doi: 10.23919/OCEANS.2015.7401834.

I. G. Cumming and F. H.-c. Wong. *Digital processing of synthetic aperture radar data : algorithms and implementation / Ian G. Cumming, Frank H. Wong*. Artech House remote sensing library. Artech House, Boston, 2005. ISBN 1580530583.

S. Dinardo, L. Fenoglio-Marc, C. Buchhaupt, M. Becker, R. Scharroo, M. Joana Fernandes, and J. Benveniste. Coastal sar and plrm altimetry in german bight and west baltic sea. *Advances in Space Research*, 62(6):1371–1404, 2018. ISSN 0273-1177. doi: https://doi.org/10.1016/j.asr.2017.12.018. URL

https://www.sciencedirect.com/science/article/pii/S0273117717308943. The CryoSat Satellite Altimetry Mission: Eight Years of Scientific Exploitation.

C. J. Donlon, R. Cullen, L. Giulicchi, P. Vuilleumier, C. R. Francis, M. Kuschnerus, W. Simpson, A. Bouridah, M. Caleno, R. Bertoni, J. Rancaño, E. Pourier, A. Hyslop, J. Mulcahy, R. Knockaert, C. Hunter, A. Webb, M. Fornari, P. Vaze, S. Brown, J. Willis, S. Desai, J.-D. Desjonqueres, R. Scharroo, C. Martin-Puig, E. Leuliette, A. Egido, W. H. Smith, P. Bonnefond, S. Le Gac, N. Picot, and G. Tavernier. The copernicus sentinel-6 mission: Enhanced continuity of satellite sea level measurements from space. *Remote Sensing of Environment*, 258:112395, 2021. ISSN 0034-4257. doi: https://doi.org/10.1016/j.rse.2021.112395. URL https://www.sciencedirect.com/science/article/pii/S0034425721001139.

A. Egido and W. Smith. Fully focused sar altimetry: Theory and applications. *IEEE Transactions on Geoscience and Remote Sensing*, PP:1–15, 01 2017. doi: 10.1109/TGRS.2016.2607122.

A. Egido, S. Dinardo, and C. Ray. The case for increasing the posting rate in delay/-doppler altimeters. *Advances in Space Research*, 68(2):930–936, 2021. ISSN 0273-1177. doi: https://doi.org/10.1016/j.asr.2020.03.014. URL https://www.sciencedirect.com/science/article/pii/S0273117720301691. 25 Years of Progress in Radar Altimetry.

F. Ehlers, F. Schlembach, M. Kleinherenbrink, and C. Slobbe. Validity assessment of samosa retracking for fully-focused sar altimeter waveforms. *Advances in Space Research*, 71(3):1377–1396, 2023. ISSN 0273-1177. doi: https://doi.org/10.1016/j.asr.2022.11.034. URL https://www.sciencedirect.com/science/article/pii/S0273117722010651.

G. Engen and H. Johnsen. Sar-ocean wave inversion using image cross spectra. *IEEE Transactions on Geoscience and Remote Sensing*, 33(4):1047–1056, 1995. doi: 10.1109/36.406690.

ESA. Sentinel-6 mission overview, 2021. URL https://sentinels.copernicus.eu/web/sentinel/missions/sentinel-6/overview.

ESA. Sentinel-3 altimetry sampling, 2023. URL https://sentinels.copernicus.eu/web/sentinel/user-guides/sentinel-3-altimetry/resolutions/sampling.

EUMETSAT. Sentinel-6/jason-cs alt level 1 product generation specification (l1 alt pgs). Technical report, EUMETSAT, EUM/LEO-JASCS/SPE/17/901031, 2021.

Eumetsat. Earth observation portal. Eumetsat, 4 2023. URL https://eoportal.eumetsat.int/.

European Space Agency. Nor sponsorship. ESA, 6 2020. URL https://eo4society.esa.int/network-of-resources/nor-sponsorship/.

B. C. Glavovic, R. Dawson, W. Chow, M. Garschagen, M. Haasnoot, C. Singh, and A. Thomas. 2022: Cross-chapter paper 2: Cities and settlements by the sea. *In: Climate Change 2022: Impacts, Adaptation and Vulnerability. Contribution of Working Group II to the Sixth Assessment Report of the Intergovernmental Panel on Climate Change*, pages 2163–2194, 2022. doi: 10. 1017/9781009325844.019.

M. Grgic and T. Bašić. *Radar Satellite Altimetry in Geodesy -Theory, Applications and Recent Developments*. intechopen, 04 2021. ISBN 978-1-83962-763-7. doi: 10.5772/intechopen.97349.

P. Guccione, M. Scagliola, and D. Giudici. 2d frequency domain fully focused sar processing for high prf radar altimeters. *Remote Sensing*, 10(12), 2018. ISSN 2072-4292. doi: 10.3390/rs10121943. URL https://www.mdpi.com/2072-4292/10/12/1943.

C. Hall, R. H. Bouchard, and D. C. Petraitis. Wave module field evaluations between the ndbc's scoop on modified 3-m foam hulls and nearby operational systems. In *OCEANS 2018 MTS/IEEE Charleston*, pages 1–6, 2018. doi: 10.1109/OCEANS.2018.8604855.

K. Hasselmann and S. Hasselmann. On the nonlinear mapping of an ocean wave spectrum into a synthetic aperture radar image spectrum and its inversion. *Journal of Geophysical Research: Oceans*, 96(C6): 10713–10729, 1991. doi: https://doi.org/10.1029/91JC00302. URL https://agupubs.onlinelibrary.wiley.com/doi/abs/10.1029/91JC00302.

K. Hasselmann, R. K. Raney, W. J. Plant, W. Alpers, R. A. Shuchman, D. R. Lyzenga, C. L. Rufenach, and M. J. Tucker. Theory of synthetic aperture radar ocean imaging: A marsen view. *Journal of Geophysical*

Research: Oceans, 90(C3):4659–4686, 1985. doi: https://doi.org/10.1029/JC090iC03p04659. URL https://agupubs.onlinelibrary.wiley.com/doi/abs/10.1029/JC090iC03p04659.

D. Hauser, C. Tison, T. Amiot, L. Delaye, N. Corcoral, and P. Castillan. Swim: The first spaceborne wave scatterometer. *IEEE Transactions on Geoscience and Remote Sensing*, 55(5):3000–3014, 2017. doi: 10.1109/TGRS.2017.2658672.

D. Hauser, S. Abdalla, F. Ardhuin, J.-R. Bidlot, M. Bourassa, D. Cotton, C. Gommenginger, H. Evers-King, H. Johnsen, J. Knaff, S. Lavender, A. Mouche, N. Reul, C. Sampson, E. C. Steele, and A. Stoffelen. Satellite remote sensing of surface winds, waves, and currents: Where are we now? *Surveys in Geophysics*, Mar. 2023. doi: 10.1007/s10712-023-09771-2. URL https://doi.org/10.1007/s10712-023-09771-2.

J. Jensen. Angle measurement with a phase monopulse radar altimeter. *Antennas and Propagation, IEEE Transactions on*, 47:715 – 724, 05 1999a. doi: 10.1109/8.768812.

J. Jensen. Radar altimeter gate tracking: theory and extension. *IEEE Transactions on Geoscience and Remote Sensing*, 37(2):651–658, 1999b. doi: 10.1109/36.752182.

L. Jiang, R. Schneider, O. B. Andersen, and P. Bauer-Gottwein. Cryosat-2 altimetry applications over rivers and lakes. *Water*, 9(3), 2017. ISSN 2073-4441. doi: 10.3390/w9030211. URL https://www.mdpi.com/2073-4441/9/3/211.

V. Kerbaol, B. Chapron, and P. W. Vachon. Analysis of ers-1/2 synthetic aperture radar wave mode imagettes. *Journal of Geophysical Research: Oceans*, 103(C4):7833–7846, 1998. doi: https://doi.org/10.1029/97JC01579. URL https://agupubs.onlinelibrary.wiley.com/doi/abs/10.1029/97JC01579.

B. Kinsman. *Wind Waves: Their Generation and Propagation on the Ocean Surface*. Dover Books on Chemistry and Earth Sciences. Dover Publications, 1984. ISBN 9780486646527. URL https://books.google.nl/books?id=_5ESAQAAIAAJ.

M. Kleinherenbrink, M. Naeije, C. Slobbe, A. Egido, and W. Smith. The performance of cryosat-2 fully-focussed sar for inland water-level estimation. *Remote Sensing of Environment*, 237:111589, 2020. ISSN 0034-4257. doi: https://doi.org/10.1016/j.rse.2019.111589. URL https://www.sciencedirect.com/science/article/pii/S0034425719306091.

H. J. Kramer. Copernicus: Sentinel-6 michael freilich mission — formerly sentinel-6 / jason-cs (jason continuity of service) mission. ESA, 2022. URL https://directory.eoportal.org/web/eoportal/satellite-missions/c-missions/copernicus-sentinel-6-michael-freilich.

H. E. Krogstad and Øivind A. Arntsen. *Linear Wave Theory, Part A*. Norwegian University of Science and Technology, Trondheim, Norway, February 2000. Draft, available at https://folk.ntnu.no/oivarn/hercules_ntnu/LWTcourse/lwt_new_2000_Part_A.pdf.

V. Kudryavtsev, M. Yurovskaya, B. Chapron, F. Collard, and C. Donlon. Sun glitter imagery of ocean surface waves. part 1: Directional spectrum retrieval and validation. *Journal of Geophysical Research: Oceans*, 122(2):1369–1383, 2017. doi: https://doi.org/10.1002/2016JC012425. URL https://agupubs.onlinelibrary.wiley.com/doi/abs/10.1002/2016JC012425.

M. Kuschnerus, R. Cullen, M. Fornari, L. Giulicchi, T. Moreau, P. Rieu, F. Boy, E. Makhoul varona, and M. Roca. Sentinel-6 poseidon-4 rmc mode processing and expected performance, Sep. 2018.

C. Maraldi, E. Cadier, S. Dinardo, A. Guerou, and T. Moreau. S6 validation team meeting product quality over ocean. url: https://s6vt.org, Oct. 2021. Last visited 2022-02-11.

T. Moreau, N. Tran, J. Aublanc, C. Tison, S. Le Gac, and F. Boy. Impact of long ocean waves on wave height retrieval from sar altimetry data. *Advances in Space Research*, 62(6):1434–1444, 2018. ISSN 0273-1177. doi: https://doi.org/10.1016/j.asr.2018.06.004. URL https://www.sciencedirect.com/science/article/pii/S0273117718304708. The CryoSat Satellite Altimetry Mission: Eight Years of Scientific Exploitation.

R. Morrow, L.-L. Fu, F. Ardhuin, M. Benkiran, B. Chapron, E. Cosme, F. d'Ovidio, J. T. Farrar, S. T. Gille, G. Lapeyre, P.-Y. Le Traon, A. Pascual, A. Ponte, B. Qiu, N. Rascle, C. Ubelmann, J. Wang, and E. D. Zaron. Global observations of fine-scale ocean surface topography with the surface water and ocean

topography (swot) mission. *Frontiers in Marine Science*, 6, 2019. ISSN 2296-7745. doi: 10.3389/fmars.2019.00232. URL https://www.frontiersin.org/articles/10.3389/fmars.2019.00232.

H. Naeser. Why ripples become sweiis, and swells in shallow water decay rapidly. *Geophysical & Astrophysical Fluid Dynamics*, 13(1):335–345, 1979. doi: 10.1080/03091927908243780. URL https://doi.org/10.1080/03091927908243780.

National Data Buoy Center. What are the sensors' reporting, sampling, and accuracy readings?, Feb. 28, 2017. URL https://www.ndbc.noaa.gov/rsa.shtml.

National Data Buoy Center. Astation 46047 (llnr 82) - tanner bank - 121 nm west of san diego, ca. NDBC, 4 2023. URL https://www.ndbc.noaa.gov/station_page.php?station=46047.

T. Nishanka, D. Prajwal, M. Nishmitha, and V. s bhat. Real-time flow visualization using projection mapping technique. *IOP Conference Series: Materials Science and Engineering*, 1187:012013, 09 2021. doi: 10.1088/1757-899X/1187/1/012013.

Observing Systems Capability Analysis and Review Tool. Satellite: Sentinel-6a, May 20, 2021. URL https://space.oscar.wmo.int/satellites/view/sentinel_6a.

W. C. O'Reilly, T. H. C. Herbers, R. J. Seymour, and R. T. Guza. A comparison of directional buoy and fixed platform measurements of pacific swell. *Journal of Atmospheric and Oceanic Technology*, 13(1):231 – 238, 1996. doi: https://doi.org/10.1175/1520-0426(1996)013<0231:ACODBA>2.0.CO;2. URL https://journals.ametsoc.org/view/journals/atot/13/1/1520-0426_1996_013_0231_acodba_2_0_co_2.xml.

C. Orrù. *SARvatore Altimetry Virtual Lab Migration and Integration in the EarthConsole Platform – Software User Manual*. Progressive Systems, Via Enrico Fermi, 62, 00044 Frascati RM, Italia, 01.00 edition, December 2021. Available at https://earthconsole.eu/wp-content/uploads/2021/10/SARvatore-AVL-EarthConsole-AVL_Software_User_Manual.pdf.

L. Phalippou and F. Demeestere. Ocean sar altimetry from siral2 on cryosat2 to poseidon-4 on jason-cs. SAR Altimetry EGM, 06 2013. URL https://www.satoc.eu/projects/CP4O/docs/SARALT_EG_pdfs/SAR%20Altimetry%20NOC%20Southampton%202013%20Phalippou.pdf.

L. Phalippou, E. Caubet, F. Demeestere, J. Richard, M. Deschaux-Beaume, S. Francis, and R. Cullen. Reaching sub-centimeter range noise on jason-cs with the poseidon-4 continuous sar interleaved mode. Ocean Surface Topography Science Team meeting, 09 2012. URL https://www.aviso.altimetry.fr/fileadmin/documents/OSTST/2012/oral/02_friday_28/05_instr_processing_IIb/05_IP2B_Phalippou.pdf.

N. Picot, P. Rieu, T. Moreau, and P. Thibaut. Sentinel-6 sar-rmc mode: assessment using sentinel-3 data, Sep. 2018.

A. W. M. Pomeroy, C. D. Storlazzi, K. J. Rosenberger, R. J. Lowe, J. E. Hansen, and M. L. Buckley. The contribution of currents, sea-swell waves, and infragravity waves to suspended-sediment transport across a coral reef-lagoon system. *Journal of Geophysical Research: Oceans*, 126(3):e2020JC017010, 2021. doi: https://doi.org/10.1029/2020JC017010. URL https://agupubs.onlinelibrary.wiley.com/doi/abs/10.1029/2020JC017010. e2020JC017010 2020JC017010.

H.-O. Pörtner, D. Roberts, H. Adams, I. Adelekan, C. Adler, R. Adrian, P. Aldunce, E. Ali, R. A. Begum, B. B. Friedl, R. B. Kerr, R. Biesbroek, J. Birkmann, K. Bowen, M. Caretta, J. Carnicer, E. Castellanos, T. Cheong, W. Chow, G. C. G. Cissé, and Z. Z. Ibrahim. *Climate Change 2022: Impacts, Adaptation and Vulnerability*. Technical Summary. Cambridge University Press, Cambridge, UK and New York, USA, 2022. ISBN 9781009325844.

E. Quataert, C. Storlazzi, A. van Dongeren, and R. McCall. The importance of explicitly modelling sea-swell waves for runup on reef-lined coasts. *Coastal Engineering*, 160:103704, 2020. ISSN 0378-3839. doi: https://doi.org/10.1016/j.coastaleng.2020.103704. URL https://www.sciencedirect.com/science/article/pii/S0378383919302728.

R. Raney. The delay/doppler radar altimeter. *IEEE Transactions on Geoscience and Remote Sensing*, 36 (5):1578–1588, 1998. doi: 10.1109/36.718861.

R. K. Raney. Maximizing the intrinsic precision of radar altimetric measurements. *IEEE Geoscience and*

Remote Sensing Letters, 10(5):1171–1174, 2013. doi: 10.1109/LGRS.2012.2235138.

D. T. Resio, S. M. Bratos, and E. F. Thompson. *Coastal Engineering Manual Part II Chapter 2, Meteorology and Wave Climate*. U.S. Army Corps of Engineers, 441 G Street, NW Washington, DC 20314-1000, April 2002. Available at http://msi.ttu.ee/~elken/CEM_Part-II_Chap-2.pdf.

K. F. Rieder and J. A. Smith. Removing wave effects from the wind stress vector. *Journal of Geophysical research*, 103(C1):1363–1374, jan 1998. doi: 10.1029/97JC02571. URL https://ui.adsabs.harvard.edu/abs/1998JGR...103.1363R.

P. Rieu, T. Moreau, L. Amarouche, P. Thibaut, F. Boy, S. Le Gac, N. Picot, F. Borde, and C. Mavrocordatos. From unfocused to fully-focused sar processing: benefits for different surfaces. Ocean Surface Topography Science Team meeting, 09 2018. URL https://meetings.aviso.altimetry.fr/fileadmin/user_upload/IPC_04_Rieu.pdf.

P. Rieu, T. Moreau, E. Cadier, M. Raynal, S. Clerc, C. Donlon, F. Borde, F. Boy, and C. Maraldi. Exploiting the sentinel-3 tandem phase dataset and azimuth oversampling to better characterize the sensitivity of sar altimeter sea surface height to long ocean waves. *Advances in Space Research*, 67(1):253–265, 2021. ISSN 0273-1177. doi: https://doi.org/10.1016/j.asr.2020.09.037. URL https://www.sciencedirect.com/science/article/pii/S0273117720306840.

V. Rosmorduc, J. Benveniste, E. Bronner, S. Dinardo, O. Lauret, C. Maheu, M. Milagro, N. Picot, A. Ambrozio, R. Escolà, A. Garcia-Mondejar, E. Schrama, M. Restano, and M. Terra-Homem. Radar Altimetry Tutorial. Technical report, ESA, October 2018.

S3-MPC. *Sentinel-3 SRAL Land User Handbook*. European Space Agency, issue 1.1 edition, December 2022. Available at https://sentinel.esa.int/documents/247904/4871083/Sentinel-3+SRAL+Land+User+Handbook+V1.1.pdf.

M. Scagliola, O. Altiparmaki, N. Bercher, L. Fenoglio, K. Nielsen, M. Passaro, M. Restano, B. Abis, M. Fornari, G. Sabatino, and J. Benveniste. Aresys ff-sar service for cryosat-2 at esa gpod. CryoSat 10th Anniversary Conference, 06 2021.

R. Scharroo, B. Hans, C. Ponsard, F. Parisot, A. Engeln, M. Tahtadjiev, K. Vriendt, and F. Montagner. Jason continuity of services: Continuing the jason altimeter data records as copernicus sentinel-6. *Ocean Science (OS)*, 12:471–479, 04 2016. doi: 10.5194/os-12-471-2016.

R. Scharroo, C. Donlon, E. Leuliette, J. Willis, and P. Bonnefond. S6 validation team meeting summary and conclusions. url: https://cdn.eventsforce.net/files/ef-xnn67yq56ylu/website/40/s6vt-04_summary_conclusions_recommendations.pdf, Jul. 2022. Last visited 2023-04-11.

F. Schlembach, F. Ehlers, M. Kleinherenbrink, M. Passaro, D. Dettmering, F. Seitz, and C. Slobbe. Benefits of fully focused sar altimetry to coastal wave height estimates: A case study in the north sea. *Remote Sensing of Environment*, 289:113517, 2023. ISSN 0034-4257. doi: https://doi.org/10.1016/j.rse.2023.113517. URL https://www.sciencedirect.com/science/article/pii/S0034425723000688.

A. Semedo, K. Sušelj, A. Rutgersson, and A. Sterl. A global view on the wind sea and swell climate and variability from era-40. *Journal of Climate*, 24(5):1461 – 1479, 2011. doi: https://doi.org/10.1175/2010JCLI3718.1. URL https://journals.ametsoc.org/view/journals/clim/24/5/2010jcli3718.1.xml.

F. A. Shillington. Low frequency 0.045-hz swell from the southern ocean. *Nature*, 290(5802):123–125, Mar 1981. ISSN 1476-4687. doi: 10.1038/290123a0. URL https://doi.org/10.1038/290123a0.

E. Stoker. *DWR-MkIII, DWR-G, WR-SG Reference Manual*. Datawell BV Oceanographic Instruments, Voltastraat 3, 1704 RP Heerhugowaard, The Netherlands, February 2020. Available at https://datawell.nl/wp-content/uploads/2022/09/datawell_manual_dwr-mk3_dwr-g_wr-sg.pdf.

Swellbeat. What is a wave spectrum? Swellbeat, 11 2020. URL https://swellbeat.com/.

Symbios. Ceos eo handbook – instrument summary - poseidon-4 altimeter, 2022. URL http://database.eohandbook.com/database/instrumentsummary.aspx?instrumentID=1723.

G. R. Valenzuela. Theories for the interaction of electromagnetic and oceanic waves — a review. *Boundary-Layer Meteorology*, 13(1):61–85, Jan 1978. ISSN 1573-1472. doi: 10.1007/BF00913863. URL https://doi.org/10.1007/BF00913863.

Y. Wan, X. Zhang, Y. Dai, and X. Shi. An azimuth cut-off wavelength compensation method based on multiview synthetic aperture radar synchronization data. *Remote Sensing Letters*, 11:245–254, 03 2020. doi: 10.1080/2150704X.2019.1706008.

H. Wang, A. Mouche, R. Husson, A. Grouazel, B. Chapron, and J. Yang. Assessment of ocean swell height observations from sentinel-1a/b wave mode against buoy in situ and modeling hindcasts. *Remote Sensing*, 14(4), 2022. ISSN 2072-4292. doi: 10.3390/rs14040862. URL https://www.mdpi.com/2072-4292/14/4/862.

Y. Wei, H. Kawamura, and Z. Tang. Swell parameters retrieval using alos/palsar data. In *2013 IEEE International Geoscience and Remote Sensing Symposium - IGARSS*, pages 2416–2419, 2013. doi: 10.1109/IGARSS.2013.6723307.

D. Wingham, C. Francis, S. Baker, C. Bouzinac, D. Brockley, R. Cullen, P. de Chateau-Thierry, S. Laxon, U. Mallow, C. Mavrocordatos, L. Phalippou, G. Ratier, L. Rey, F. Rostan, P. Viau, and D. Wallis. Cryosat: A mission to determine the fluctuations in earth's land and marine ice fields. *Advances in Space Research*, 37(4):841–871, 2006. ISSN 0273-1177. doi: https://doi.org/10.1016/j.asr.2005.07.027. URL https://www.sciencedirect.com/science/article/pii/S0273117705009348. Natural Hazards and Oceanographic Processes from Satellite Data.

World Meteorological Organization (WMO), United Nations Educational Scientific and Cultural Organization, Intergovernmental Oceanographic Commission, United Nations Environment Programme, and International Science Council (ISC). The 2022 GCOS ECVs Requirements (GCOS 245). Technical Report 245, Global Climate Observing System programme, 2022.

I. R. Young, S. Zieger, and A. V. Babanin. Global trends in wind speed and wave height. *Science*, 332 (6028):451–455, 2011. doi: 10.1126/science.1197219. URL https://www.science.org/doi/abs/10.1126/science.1197219.

Z. Zou, J. Song, P. Li, J. Huang, J. A. Zhang, Z. Wan, and S. Li. Effects of swell waves on atmospheric boundary layer turbulence: A low wind field study. *Journal of Geophysical Research: Oceans*, 124(8): 5671–5685, 2019. doi: https://doi.org/10.1029/2019JC015153. URL https://agupubs.onlinelibrary.wiley.com/doi/abs/10.1029/2019JC015153.

A

Overview of available passes and passes with swell

Table A.1: Passes processed in FFSAR from 2020 to Feb 2023 featuring the presence of both RAW and RMC

n	track 119	track 206
	'L1B_FF_ML_YYYYMMDDTHHMMSSstart_YYYYMMDDTHHMMSSstop.nc	*'L1B_FF_ML_YYYYMMDDTHHMMSSstart_YYYYMMDDTHHMMSSstop.nc*
1	L1B_FF_ML_20210618T125327_20210618T125345.nc	L1B_FF_ML_20210403T141333_20210403T141350.nc
2	L1B_FF_ML_20210817T004435_20210817T004452.nc	L1B_FF_ML_20210621T220146_20210621T220203.nc
3	L1B_FF_ML_20210925T163842_20210925T163859.nc	L1B_FF_ML_20210820T095254_20210820T095311.nc
4	L1B_FF_ML_20211005T143713_20211005T143731.nc	L1B_FF_ML_20210929T014700_20210929T014718.nc
5	L1B_FF_ML_20211015T123545_20211015T123602.nc	L1B_FF_ML_20211008T234532_20211008T234549.nc
6	L1B_FF_ML_20211025T103416_20211025T103433.nc	L1B_FF_ML_20211018T214403_20211018T214420.nc
7	L1B_FF_ML_20220221T101634_20220221T101651.nc	L1B_FF_ML_20211028T194234_20211028T194252.nc
8	L1B_FF_ML_20220303T081505_20220303T081522.nc	L1B_FF_ML_20211107T174106_20211107T174123.nc
9	L1B_FF_ML_20220313T061336_20220313T061353.nc	L1B_FF_ML_20211117T153937_20211117T153955.nc
10	L1B_FF_ML_20220323T041208_20220323T041225.nc	L1B_FF_ML_20211127T133809_20211127T133826.nc
11	L1B_FF_ML_20220402T021040_20220402T021057.nc	L1B_FF_ML_20211207T113641_20211207T113658.nc
12	L1B_FF_ML_20220412T000911_20220412T000929.nc	L1B_FF_ML_20211217T093512_20211217T093530.nc
13	L1B_FF_ML_20220421T220743_20220421T220800.nc	L1B_FF_ML_20211227T073344_20211227T073402.nc
14	L1B_FF_ML_20220501T200615_20220501T200632.nc	L1B_FF_ML_20220106T053216_20220106T053233.nc
15	L1B_FF_ML_20220511T180446_20220511T180503.nc	L1B_FF_ML_20220116T033048_20220116T033105.nc
16	L1B_FF_ML_20220521T160317_20220521T160335.nc	L1B_FF_ML_20220126T012919_20220126T012936.nc
17	L1B_FF_ML_20220531T140149_20220531T140206.nc	L1B_FF_ML_20220204T232750_20220204T232807.nc
18	L1B_FF_ML_20220610T120020_20220610T120037.nc	L1B_FF_ML_20220214T212621_20220214T212638.nc
19	L1B_FF_ML_20220620T095851_20220620T095908.nc	L1B_FF_ML_20220224T192452_20220224T192509.nc
20	L1B_FF_ML_20220630T075723_20220630T075740.nc	L1B_FF_ML_20220306T172323_20220306T172340.nc
21	L1B_FF_ML_20220710T055555_20220710T055612.nc	L1B_FF_ML_20220316T152155_20220316T152212.nc
22	L1B_FF_ML_20220720T035427_20220720T035444.nc	L1B_FF_ML_20220326T132027_20220326T132044.nc
23	L1B_FF_ML_20220730T015258_20220730T015316.nc	L1B_FF_ML_20220405T111858_20220405T111916.nc
24	L1B_FF_ML_20220808T235130_20220808T235147.nc	L1B_FF_ML_20220415T091730_20220415T091747.nc
25	L1B_FF_ML_20220818T215002_20220818T215019.nc	L1B_FF_ML_20220425T071601_20220425T071619.nc
26	L1B_FF_ML_20220828T194833_20220828T194851.nc	L1B_FF_ML_20220505T051433_20220505T051450.nc
27	L1B_FF_ML_20220907T174705_20220907T174722.nc	L1B_FF_ML_20220515T031305_20220515T031322.nc
28	L1B_FF_ML_20220917T154536_20220917T154553.nc	L1B_FF_ML_20220525T011136_20220525T011153.nc
29	L1B_FF_ML_20220927T134407_20220927T134424.nc	L1B_FF_ML_20220603T231007_20220603T231024.nc
30	L1B_FF_ML_20221007T114238_20221007T114255.nc	L1B_FF_ML_20220613T210838_20220613T210855.nc
31	L1B_FF_ML_20221017T094110_20221017T094127.nc	L1B_FF_ML_20220623T190709_20220623T190726.nc
32	L1B_FF_ML_20221027T073942_20221027T074000.nc	L1B_FF_ML_20220703T170541_20220703T170559.nc
33	L1B_FF_ML_20221106T053815_20221106T053832.nc	L1B_FF_ML_20220713T150414_20220713T150431.nc
34	L1B_FF_ML_20221116T033647_20221116T033704.nc	L1B_FF_ML_20220723T130245_20220723T130303.nc
35	L1B_FF_ML_20221126T013519_20221126T013536.nc	L1B_FF_ML_20220802T110117_20220802T110134.nc
36	L1B_FF_ML_20221205T233351_20221205T233408.nc	L1B_FF_ML_20220812T085949_20220812T090006.nc
37	L1B_FF_ML_20221215T213222_20221215T213239.nc	L1B_FF_ML_20220822T065820_20220822T065837.nc
38	L1B_FF_ML_20221225T193053_20221225T193110.nc	L1B_FF_ML_20220901T045652_20220901T045709.nc
39	L1B_FF_ML_20230104T172923_20230104T172941.nc	L1B_FF_ML_20220911T025523_20220911T025540.nc
40	L1B_FF_ML_20230114T152754_20230114T152811.nc	L1B_FF_ML_20220921T005354_20220921T005412.nc
41	L1B_FF_ML_20230124T132625_20230124T132643.nc	L1B_FF_ML_20221010T205056_20221010T205114.nc
42	L1B_FF_ML_20230203T112458_20230203T112515.nc	L1B_FF_ML_20221020T184929_20221020T184946.nc
43	L1B_FF_ML_20230213T092330_20230213T092348.nc	L1B_FF_ML_20221030T164801_20221030T164818.nc
44	L1B_FF_ML_20230223T072203_20230223T072220.nc	L1B_FF_ML_20221109T144634_20221109T144651.nc
45		L1B_FF_ML_20221119T124506_20221119T124523.nc
46		L1B_FF_ML_20221129T104338_20221129T104355.nc
47		L1B_FF_ML_20221209T084209_20221209T084226.nc
48		L1B_FF_ML_20221219T064040_20221219T064057.nc
49		L1B_FF_ML_20221229T043911_20221229T043928.nc
50		L1B_FF_ML_20230108T023741_20230108T023759.nc
51		L1B_FF_ML_20230118T003612_20230118T003629.nc
52		L1B_FF_ML_20230127T223444_20230127T223501.nc
53		L1B_FF_ML_20230206T203317_20230206T203334.nc
54		L1B_FF_ML_20230216T183149_20230216T183206.nc
55		L1B_FF_ML_20230226T163021_20230226T163039.nc

Table A.2: Passes processed in FFSAR from Dec 2020 to Feb 2023 featuring the presence of both RAW, RMC and swell (DPD >10 s)

	segment 1		segment 2	
	satellite timestamp	**buoy 46219 timestamp**	**satellite timestamp**	**buoy 46219 timestamp**
1	17-08-21 0:44	17-08-21 0:56	03-04-21 14:13	03-04-21 12:26
2	25-09-21 16:38	25-09-21 13:26	21-06-21 22:01	21-06-21 22:56
3	05-10-21 14:37	05-10-21 11:26	20-08-21 9:52	20-08-21 10:56
4	15-10-21 12:35	15-10-21 8:56	29-09-21 1:47	29-09-21 0:26
5	25-10-21 10:34	25-10-21 7:56	08-10-21 23:45	08-10-21 21:26
6	21-02-22 10:16	21-02-22 7:56	28-10-21 19:42	28-10-21 17:56
7	03-03-22 8:15	03-03-22 5:56	07-11-21 17:41	07-11-21 15:26
8	13-03-22 6:13	13-03-22 3:26	27-11-21 13:38	27-11-21 11:56
9	23-03-22 4:12	23-03-22 0:56	17-12-21 9:35	17-12-21 7:26
10	02-04-22 2:10	02-04-22 0:26	27-12-21 7:33	27-12-21 5:26
11	12-04-22 0:09	12-04-22 0:26	06-01-22 5:32	06-01-22 3:26
12	21-04-22 22:07	21-04-22 18:56	16-01-22 3:30	16-01-22 1:56
13	11-05-22 18:04	11-05-22 13:56	26-01-22 1:29	26-01-22 0:26
14	21-05-22 16:03	21-05-22 12:26	04-02-22 23:27	04-02-22 21:56
15	31-05-22 14:01	31-05-22 9:56	06-03-22 17:23	06-03-22 14:56
16	20-06-22 9:58	20-06-22 5:26	16-03-22 15:21	16-03-22 13:26
17	30-06-22 7:57	30-06-22 7:26	26-03-22 13:20	26-03-22 11:56
18	20-07-22 3:54	20-07-22 4:26	25-04-22 7:16	25-04-22 5:56
19	18-08-22 21:50	18-08-22 23:56	05-05-22 5:14	05-05-22 2:26
20	28-08-22 19:48	28-08-22 20:56	15-05-22 3:13	15-05-22 0:56
21	07-09-22 17:47	07-09-22 18:26	25-05-22 1:11	25-05-22 3:56
22	07-10-22 11:42	07-10-22 8:56	03-06-22 23:10	03-06-22 23:26
23	17-10-22 9:41	17-10-22 9:56	23-06-22 19:07	23-06-22 16:26
24	16-11-22 3:36	16-11-22 0:56	13-07-22 15:04	13-07-22 15:56
25	26-11-22 1:35	26-11-22 0:26	02-08-22 11:01	02-08-22 12:56
26	05-12-22 23:33	05-12-22 20:26	22-08-22 6:58	22-08-22 8:26
27	15-12-22 21:32	15-12-22 18:56	21-09-22 0:53	21-09-22 0:56
28	25-12-22 19:30	25-12-22 16:56	10-10-22 20:50	10-10-22 21:26
29	04-01-23 17:29	04-01-23 15:26	20-10-22 18:49	20-10-22 16:56
30	24-01-23 13:26	24-01-23 11:56	30-10-22 16:48	30-10-22 14:56
31	03-02-23 11:24	03-02-23 9:26	09-11-22 14:46	09-11-22 12:26
32	13-02-23 9:23	13-02-23 5:56	19-11-22 12:45	19-11-22 10:56
33	23-02-23 7:22	23-02-23 4:56	29-11-22 10:43	29-11-22 7:26
34			09-12-22 8:42	09-12-22 6:56
35			19-12-22 6:40	19-12-22 5:56
36			29-12-22 4:39	29-12-22 2:56
37			08-01-23 2:37	08-01-23 0:26
38			18-01-23 0:36	18-01-23 0:26
39			27-01-23 22:34	27-01-23 21:26
40			06-02-23 20:33	06-02-23 18:26
41			16-02-23 18:31	16-02-23 15:56
42			26-02-23 16:30	26-02-23 13:56

B

Performance data tables

Table B.1: Performance data for the RAW cutting window sensitivity analysis on across- track limit values. Along-track interval (wmin- wmax): 20 km → 34.5 km.

Satellite timestamp	Buoy timestamp	Segment	DPD 46219 [s]	T_s RAW 4-10 km [s]	T_s RAW 6-12 km [s]	T_s RAW 8-14 km [s]	T_s RAW 7-13 km [s]	T_s RAW 7-13.5 km [s]
03-Apr-2021 12:26:00	12:26:00	2	14.29	14.81	14.97	14.45	14.64	14.87
21-Jun-2021 22:56:00	22:56:00	2	15.38	18.06	16.15	17.73	17.77	17.71
17-Aug-2021 00:56:00	00:56:00	1	10.53	16.07	16.16	16.73	16.68	16.75
20-Aug-2021 10:56:00	10:56:00	2	16.67	*N/A*	*N/A*	*N/A*	*N/A*	*N/A*
25-Sep-2021 13:26:00	13:26:00	1	11.76	*N/A*	16.09	16.60	16.47	16.51
29-Sep-2021 00:26:00	00:26:00	2	14.29	15.90	15.66	15.09	15.46	15.51
05-Oct-2021 11:26:00	11:26:00	1	12.50	16.09	14.32	13.66	13.29	13.52
08-Oct-2021 21:26:00	21:26:00	2	11.11	17.30	16.77	16.43	16.60	16.97
25-Oct-2021 07:56:00	07:56:00	1	13.33	14.58	13.96	15.07	12.62	12.82
28-Oct-2021 17:56:00	17:56:00	2	18.18	17.47	18.71	17.44	17.36	17.25
07-Nov-2021 15:26:00	15:26:00	2	12.50	19.31	18.20	17.12	17.32	17.20
27-Nov-2021 11:56:00	11:56:00	2	15.38	14.86	15.01	15.01	14.98	15.16
17-Dec-2021 07:26:00	07:26:00	2	13.33	21.25	14.62	14.50	14.03	13.82
27-Dec-2021 05:26:00	05:26:00	2	13.33	14.63	13.82	13.66	14.47	14.52
06-Jan-2022 03:26:00	03:26:00	2	13.33	14.98	14.81	14.57	14.23	14.72
16-Jan-2022 01:56:00	01:56:00	2	15.38	16.64	16.64	16.33	16.33	16.26
26-Jan-2022 00:26:00	00:26:00	2	15.38	16.44	16.17	16.17	15.75	15.76
04-Feb-2022 21:56:00	21:56:00	2	15.38	15.65	15.37	15.37	15.13	15.28
21-Feb-2022 07:56:00	07:56:00	1	15.38	15.75	15.70	16.16	16.20	16.30
24-Feb-2022 16:56:00	16:56:00	2	11.11	21.86	*N/A*	*N/A*	*N/A*	*N/A*
03-Mar-2022 05:56:00	05:56:00	1	15.38	16.62	15.74	16.28	15.74	15.88
06-Mar-2022 14:56:00	14:56:00	2	10.53	15.98	15.89	16.51	16.73	15.24
13-Mar-2022 03:26:00	03:26:00	1	12.50	15.46	20.03	13.01	13.03	12.71

Table B.1 continued from previous page

Satellite timestamp	Buoy timestamp	Segment	DPD 46219 [s]	T_S RAW 4-10 km [s]	T_S RAW 6-12 km [s]	T_S RAW 8-14 km [s]	T_S RAW 7-13 km [s]	T_S RAW 7-13.5 km [s]
16-Mar-2022 13:26:00	13:26:00	2	16.67	16.96	17.00	16.87	16.54	17.40
23-Mar-2022 00:56:00	00:56:00	1	11.76	14.03	13.36	13.29	13.98	13.02
26-Mar-2022 11:56:00	11:56:00	2	11.76	16.11	15.88	13.55	15.98	15.91
02-Apr-2022 00:26:00	00:26:00	1	13.33	15.61	14.40	13.69	13.37	13.31
21-Apr-2022 18:56:00	18:56:00	1	11.76	22.57	22.62	22.62	22.62	22.12
25-Apr-2022 05:56:00	05:56:00	2	20.00	18.96	19.76	18.40	18.49	18.72
21-May-2022 12:26:00	12:26:00	1	10.53	15.77	15.96	16.31	15.81	16.26
25-May-2022 03:56:00	03:56:00	2	14.29	*N/A*	*N/A*	*N/A*	*N/A*	*N/A*
31-May-2022 09:56:00	09:56:00	1	10.53	16.35	17.53	17.48	17.37	17.39
03-Jun-2022 23:26:00	23:26:00	2	16.67	17.77	16.62	16.59	16.62	16.69
30-Jun-2022 07:26:00	07:26:00	1	15.38	15.28	15.15	15.03	15.03	15.05
13-Jul-2022 15:56:00	15:56:00	2	13.33	16.31	17.00	18.56	13.74	14.89
20-Jul-2022 04:26:00	04:26:00	1	18.18	18.49	17.96	17.11	17.96	17.99
30-Jul-2022 02:56:00	02:56:00	1	11.76	13.62	*N/A*	*N/A*	13.15	*N/A*
02-Aug-2022 12:56:00	12:56:00	2	12.50	13.05	11.66	12.13	12.34	12.58
18-Aug-2022 23:56:00	23:56:00	1	16.67	16.51	16.51	17.10	16.51	16.44
22-Aug-2022 08:26:00	08:26:00	2	14.29	14.32	14.35	14.48	13.86	14.27
28-Aug-2022 20:56:00	20:56:00	1	15.38	15.29	15.52	15.11	14.98	15.07
07-Sep-2022 18:26:00	18:26:00	1	15.38	15.81	16.24	16.09	15.91	15.76
21-Sep-2022 00:56:00	00:56:00	2	16.67	16.90	16.15	15.48	15.98	16.73
07-Oct-2022 08:56:00	08:56:00	1	13.33	19.77	14.41	14.02	13.69	13.91
10-Oct-2022 21:26:00	21:26:00	2	12.50	18.21	17.95	15.98	13.51	13.56
17-Oct-2022 09:56:00	09:56:00	1	15.38	15.19	15.29	14.58	14.17	13.98
20-Oct-2022 16:56:00	16:56:00	2	12.50	13.11	13.66	13.48	12.62	12.63
30-Oct-2022 14:56:00	14:56:00	2	15.38	15.24	15.24	14.83	15.02	15.27
09-Nov-2022 12:26:00	12:26:00	2	13.33	15.70	15.15	14.81	16.96	16.83
16-Nov-2022 00:56:00	00:56:00	1	15.38	16.87	15.74	16.23	15.74	15.88
19-Nov-2022 10:56:00	10:56:00	2	14.29	13.79	13.89	13.52	14.07	14.02
26-Nov-2022 00:26:00	00:26:00	1	16.67	17.53	16.20	18.07	16.81	16.88
05-Dec-2022 20:26:00	20:26:00	1	11.11	14.00	13.06	13.69	14.00	13.57
09-Dec-2022 06:56:00	06:56:00	2	14.29	15.33	15.19	14.39	14.63	14.39
15-Dec-2022 18:56:00	18:56:00	1	15.38	16.02	15.52	16.07	15.26	15.42
19-Dec-2022 05:56:00	05:56:00	2	14.29	14.34	14.33	14.27	14.33	14.10
25-Dec-2022 16:56:00	16:56:00	1	15.38	17.30	16.16	16.73	18.07	18.04
29-Dec-2022 02:56:00	02:56:00	2	13.33	23.18	23.93	14.53	14.66	14.78

Table B.1 continued from previous page

Satellite timestamp	Buoy timestamp	Segment	DPD 46219 [s]	T_S RAW 4-10 km [s]	T_S RAW 6-12 km [s]	T_S RAW 8-14 km [s]	T_S RAW 7-13 km [s]	T_S RAW 7-13.5 km [s]
04-Jan-2023 15:26:00	15:26:00	1	16.67	19.01	17.46	16.77	17.46	16.84
08-Jan-2023 00:26:00	00:26:00	2	11.76	16.51	14.35	14.99	15.34	15.42
14-Jan-2023 13:26:00	13:26:00	1	16.67	21.99	19.13	18.75	18.75	18.04
18-Jan-2023 00:26:00	00:26:00	2	16.67	17.26	16.77	15.59	15.94	16.19
24-Jan-2023 11:56:00	11:56:00	1	22.22	22.62	24.32	22.64	23.73	23.05
27-Jan-2023 21:26:00	21:26:00	2	20.00	18.49	18.77	18.74	18.49	18.55
03-Feb-2023 09:26:00	09:26:00	1	18.18	18.23	18.26	18.26	18.26	18.23
06-Feb-2023 18:26:00	18:26:00	2	13.33	21.21	20.52	19.30	15.49	15.58
13-Feb-2023 05:56:00	05:56:00	1	11.11	20.96	22.57	22.57	22.57	22.07
16-Feb-2023 15:56:00	15:56:00	2	11.76	14.16	14.22	13.82	14.47	13.60
23-Feb-2023 04:56:00	04:56:00	1	14.29	21.25	19.10	16.27	19.10	16.88
26-Feb-2023 13:56:00	13:56:00	2	11.76	*N/A*	15.08	15.85	15.08	15.51
n samples				66	66	66	67	66
MAE [s]				2.73	2.24	1.98	1.87	1.77

Table B.2: Performance data for the RMC cutting window sensitivity analysis on across- track limit values. Along- track interval (wmin- wmax): 20 km → 34.5 km.

Satellite timestamp	Buoy timestamp	Segment	DPD 46219 [s]	T_S RMC 4-7 km [s]	T_S RMC 5-8 km [s]	T_S RMC 6-9 km [s]	T_S RMC 6.1-9.1 km [s]	T_S RMC 6.2-9.2 km [s]	T_S RMC 6.3-9.3 km [s]	T_S RMC 6.4-9.4 km [s]
03-Apr-2021 12:26:00	12:26:00	2	14.29	15.97	14.91	15.45	14.91	14.91	14.91	17.19
21-Jun-2021 22:56:00	22:56:00	2	15.38	17.74	19.88	18.25	18.25	18.25	18.25	18.25
17-Aug-2021 00:56:00	00:56:00	1	10.53	16.01	17.15	17.18	17.18	17.18	17.18	17.18
20-Aug-2021 10:56:00	10:56:00	2	16.67	16.37	17.09	17.09	17.09	17.09	17.09	20.66
25-Sep-2021 13:26:00	13:26:00	1	11.76	15.97	14.90	*N/A*	14.73	14.73	24.67	24.67
29-Sep-2021 00:26:00	00:26:00	2	14.29	*N/A*	15.59	15.78	15.78	16.17	16.17	16.17
05-Oct-2021 11:26:00	11:26:00	1	12.50	15.79	15.60	15.99	15.99	15.99	15.61	15.58
08-Oct-2021 21:26:00	21:26:00	2	11.11	17.74	17.49	17.14	17.14	17.14	15.04	18.69
25-Oct-2021 07:56:00	07:56:00	1	13.33	18.27	20.01	22.27	22.27	22.27	15.45	14.68
28-Oct-2021 17:56:00	17:56:00	2	18.18	19.18	19.52	19.18	18.85	18.85	17.99	18.25

Table B.2 continued from previous page

Satellite timestamp	Buoy timestamp	Segment	DPD 46219 [s]	T_S RMC 4-7 km [s]	T_S RMC 5-8 km [s]	T_S RMC 6-9 km [s]	T_S RMC 6.1-9.1 km [s]	T_S RMC 6.2-9.2 km [s]	T_S RMC 6.3-9.3 km [s]	T_S RMC 6.4-9.4 km [s]
07-Nov-2021 15:26:00	15:26:00	2	12.50	18.32	18.53	19.19	19.19	19.19	19.19	19.19
27-Nov-2021 11:56:00	11:56:00	2	15.38	17.26	17.26	16.90	15.36	15.19	15.19	15.19
17-Dec-2021 07:26:00	07:26:00	2	13.33	15.41	18.23	16.65	16.65	16.65	16.65	16.01
27-Dec-2021 05:26:00	05:26:00	2	13.33	14.13	14.07	15.21	14.89	14.89	14.89	*N/A*
06-Jan-2022 03:26:00	03:26:00	2	13.33	15.98	16.59	16.81	16.81	16.81	16.81	16.59
16-Jan-2022 01:56:00	01:56:00	2	15.38	16.37	16.58	15.79	15.79	15.79	15.79	15.79
26-Jan-2022 00:26:00	00:26:00	2	15.38	15.60	15.14	17.10	17.10	17.10	17.10	17.30
04-Feb-2022 21:56:00	21:56:00	2	15.38	15.63	16.18	16.15	16.15	16.15	16.15	17.19
21-Feb-2022 07:56:00	07:56:00	1	15.38	17.15	15.03	15.82	15.82	15.96	17.15	17.15
24-Feb-2022 16:56:00	16:56:00	2	11.11	18.08	18.63	20.62	18.08	18.08	20.66	20.66
03-Mar-2022 05:56:00	05:56:00	1	15.38	22.94	15.96	17.83	16.61	16.61	16.61	16.70
06-Mar-2022 14:56:00	14:56:00	2	10.53	15.23	18.52	15.59	15.44	15.44	15.59	17.19
13-Mar-2022 03:26:00	03:26:00	1	12.50	17.81	15.99	17.81	12.93	12.93	12.93	12.93
16-Mar-2022 13:26:00	13:26:00	2	16.67	17.39	18.23	17.26	17.26	17.26	17.26	17.26
23-Mar-2022 00:56:00	00:56:00	1	11.76	18.53	18.26	14.41	14.41	14.41	14.41	13.99
26-Mar-2022 11:56:00	11:56:00	2	11.76	15.77	17.49	16.42	16.42	16.32	16.32	16.23
02-Apr-2022 00:26:00	00:26:00	1	13.33	16.16	15.23	16.52	16.52	20.65	20.65	20.66
21-Apr-2022 18:56:00	18:56:00	1	11.76	22.73	22.73	22.73	22.73	22.73	22.73	22.73
25-Apr-2022 05:56:00	05:56:00	2	20.00	20.25	20.25	20.25	20.25	20.25	20.25	20.25
21-May-2022 12:26:00	12:26:00	1	10.53	16.07	14.89	15.99	15.79	15.79	17.19	20.66
25-May-2022 03:56:00	03:56:00	2	14.29	*N/A*	*N/A*	*N/A*	*N/A*	*N/A*	*N/A*	*N/A*
31-May-2022 09:56:00	09:56:00	1	10.53	16.70	16.96	16.96	16.96	16.96	20.66	18.69
03-Jun-2022 23:26:00	23:26:00	2	16.67	18.52	17.29	17.29	17.29	17.83	17.83	17.83
30-Jun-2022 07:26:00	07:26:00	1	15.38	14.47	14.72	14.72	14.72	14.72	14.72	17.19
13-Jul-2022 15:56:00	15:56:00	2	13.33	18.11	19.07	19.07	19.07	19.07	19.07	18.69
20-Jul-2022 04:26:00	04:26:00	1	18.18	17.04	17.82	17.31	17.31	17.52	17.52	17.52
30-Jul-2022 02:56:00	02:56:00	1	11.76	12.79	13.36	13.00	12.95	12.95	12.95	*N/A*
02-Aug-2022 12:56:00	12:56:00	2	12.50	12.06	11.99	11.78	12.45	12.45	12.45	17.19
18-Aug-2022 23:56:00	23:56:00	1	16.67	17.30	17.10	17.10	17.10	17.10	17.10	16.43
22-Aug-2022 08:26:00	08:26:00	2	14.29	14.47	13.73	14.08	13.86	13.86	15.04	18.69
28-Aug-2022 20:56:00	20:56:00	1	15.38	15.60	16.07	16.00	16.00	16.00	16.00	16.07
07-Sep-2022 18:26:00	18:26:00	1	15.38	15.38	15.46	15.46	15.46	15.38	15.19	16.08
21-Sep-2022 00:56:00	00:56:00	2	16.67	17.09	16.95	17.03	17.26	17.26	17.26	17.03
07-Oct-2022 08:56:00	08:56:00	1	13.33	14.70	13.60	13.37	13.37	13.37	13.34	17.19
10-Oct-2022 21:26:00	21:26:00	2	12.50	18.25	18.25	18.25	18.25	18.25	18.25	16.01

Table B.2 continued from previous page

Satellite timestamp	Buoy timestamp	Segment	DPD 46219 [s]	T_S RMC 4-7 km [s]	T_S RMC 5-8 km [s]	T_S RMC 6-9 km [s]	T_S RMC 6.1-9.1 km [s]	T_S RMC 6.2-9.2 km [s]	T_S RMC 6.3-9.3 km [s]	T_S RMC 6.4-9.4 km [s]
17-Oct-2022 09:56:00	09:56:00	1	15.38	14.78	14.89	15.07	15.07	15.07	15.07	15.04
20-Oct-2022 16:56:00	16:56:00	2	12.50	14.07	13.59	13.80	12.48	12.48	12.48	12.48
30-Oct-2022 14:56:00	14:56:00	2	15.38	16.46	15.27	15.81	15.81	15.81	15.81	15.81
09-Nov-2022 12:26:00	12:26:00	2	13.33	15.62	15.78	14.58	14.42	14.58	14.58	14.42
16-Nov-2022 00:56:00	00:56:00	1	15.38	14.83	15.05	15.05	15.86	15.86	15.81	17.19
19-Nov-2022 10:56:00	10:56:00	2	14.29	14.12	15.33	15.07	14.63	14.63	14.63	13.99
26-Nov-2022 00:26:00	00:26:00	1	16.67	16.60	18.53	15.96	15.96	15.96	15.96	23.43
05-Dec-2022 20:26:00	20:26:00	1	11.11	16.72	14.21	15.78	15.08	14.98	13.53	20.66
09-Dec-2022 06:56:00	06:56:00	2	14.29	15.15	15.31	15.31	15.31	15.31	15.31	15.81
15-Dec-2022 18:56:00	18:56:00	1	15.38	17.18	15.86	17.12	17.12	17.12	17.12	17.08
19-Dec-2022 05:56:00	05:56:00	2	14.29	17.10	17.43	17.27	16.52	16.52	16.52	16.01
25-Dec-2022 16:56:00	16:56:00	1	15.38	16.11	17.19	18.38	18.38	18.38	18.38	18.38
29-Dec-2022 02:56:00	02:56:00	2	13.33	22.27	22.74	13.49	13.49	13.88	*N/A*	16.01
04-Jan-2023 15:26:00	15:26:00	1	16.67	21.42	16.98	17.04	18.58	18.63	18.66	18.66
08-Jan-2023 00:26:00	00:26:00	2	11.76	21.43	15.13	15.79	15.97	15.97	14.37	17.19
14-Jan-2023 13:26:00	13:26:00	1	16.67	20.27	21.07	*N/A*	*N/A*	23.43	20.40	19.13
18-Jan-2023 00:26:00	00:26:00	2	16.67	23.25	21.43	19.13	19.13	20.01	20.01	18.69
24-Jan-2023 11:56:00	11:56:00	1	22.22	23.41	23.43	23.35	23.35	23.25	23.35	23.35
27-Jan-2023 21:26:00	21:26:00	2	20.00	18.52	21.47	19.35	19.35	19.35	19.35	19.35
03-Feb-2023 09:26:00	09:26:00	1	18.18	11.44	*N/A*	13.74	11.81	15.87	*N/A*	*N/A*
06-Feb-2023 18:26:00	18:26:00	2	13.33	23.25	23.25	20.49	20.49	20.40	20.40	16.01
13-Feb-2023 05:56:00	05:56:00	1	11.11	20.54	23.35	23.25	23.25	23.25	23.25	23.25
16-Feb-2023 15:56:00	15:56:00	2	11.76	14.63	13.87	14.46	14.46	14.54	18.69	18.69
23-Feb-2023 04:56:00	04:56:00	1	14.29	24.80	*N/A*	21.48	21.48	20.62	*N/A*	*N/A*
26-Feb-2023 13:56:00	13:56:00	2	11.76	17.74	20.62	20.28	20.49	20.49	*N/A*	16.01
n samples				68	67	67	68	69	65	65
MAE [s]				3.30	3.03	2.92	2.75	2.83	2.85	3.42

Table B.3: Performance data for the best raw and RMC cutting window (7- 13.5 km for raw and 6.1- 9.1 km for RMC across- track, waveform interval 26- 32.5 km along- track). All passes with DPD > 9s included.

Satellite timestamp	Buoy timestamp	Segment	DPD 46219 [s]	T_s RAW 7-13.5 km [s]	T_s RMC 5-8 km [s]	ABS. ERROR RAW [s]	ABS. ERROR RMC [s]	WSPD 46047 [m/s]	WDIR 46047 [degN]	SWH 46219 [m]	MWD 46219 [degN]
03-Apr-2021 14:13:33	12:26:00	2	14.29	14.88	19.92	0.59	5.63	7.4	320	1.6	293
21-Jun-2021 22:01:46	22:56:00	2	15.38	17.38	19.92	2.00	4.54	2.1	289	1.81	2
17-Aug-2021 00:44:35	00:56:00	1	10.53	16.37	17.11	5.84	6.58	2.8	241	1.47	245
20-Aug-2021 09:52:54	10:56:00	2	16.67	12.49	18.22	4.18	1.55	2.6	89	2.23	202
25-Sep-2021 16:38:42	13:26:00	1	11.76	14.97	14.69	3.21	2.93	1.6	172	1.41	293
29-Sep-2021 01:47:00	00:26:00	2	14.29	15.40	16.12	1.11	1.83	9.8	308	3.07	303
05-Oct-2021 14:37:13	11:26:00	1	12.5	13.50	14.40	1.00	1.90	3.7	334	1.47	309
08-Oct-2021 23:45:32	21:26:00	2	11.11	16.95	16.36	5.84	5.25	9.2	324	2.13	306
15-Oct-2021 12:35:45	08:56:00	1	9.88	15.37	15.18	5.49	5.30	1.1	322	2.41	313
25-Oct-2021 10:34:16	07:56:00	1	13.33	14.18	14.19	0.85	0.86	4.6	239	1.96	296
28-Oct-2021 19:42:34	17:56:00	2	18.18	17.84	18.22	0.34	0.04	2.4	274	2.7	307
07-Nov-2021 17:41:06	15:26:00	2	12.5	17.83	18.62	5.33	6.12	9.2	322	2.31	290
27-Nov-2021 13:38:09	11:56:00	2	15.38	15.17	15.05	0.21	0.33	3.7	295	1.76	302
17-Dec-2021 09:35:12	07:26:00	2	13.33	14.85	13.89	1.52	0.56	6.6	320	2.98	303
27-Dec-2021 07:33:44	05:26:00	2	13.33	13.56	13.57	0.23	0.24	6	304	3.19	309
06-Jan-2022 05:32:16	03:26:00	2	13.33	14.89	14.95	1.56	1.62	6.3	326	3	302
16-Jan-2022 03:30:48	01:56:00	2	15.38	16.43	17.13	1.05	1.75	3.1	350	2.33	297
26-Jan-2022 01:29:19	00:26:00	2	15.38	16.52	17.71	1.14	2.33	6.7	320	2.45	289
04-Feb-2022 23:27:50	21:56:00	2	15.38	15.74	15.36	0.36	0.02	4.5	6	1.56	288
21-Feb-2022 10:16:34	07:56:00	1	15.38	15.87	17.11	0.49	1.73	5.5	311	1.95	296
03-Mar-2022 08:15:05	05:56:00	1	15.38	16.13	17.11	0.75	1.73	5.3	308	3.24	290
06-Mar-2022 17:23:23	14:56:00	2	10.53	16.93	16.18	6.40	5.65	8.2	325	3.08	310
13-Mar-2022 06:13:36	03:26:00	1	12.5	15.19	12.94	2.69	0.44	8.3	308	1.69	275
16-Mar-2022 15:21:55	13:26:00	2	16.67	16.65	17.72	0.02	1.05	10.3	310	4.12	296
23-Mar-2022 04:12:08	00:56:00	1	11.76	13.01	17.95	1.25	6.19	4.4	282	1.98	300
26-Mar-2022 13:20:27	11:56:00	2	11.76	16.32	15.63	4.56	3.87	3.7	330	1.77	262
02-Apr-2022 02:10:40	00:26:00	1	13.33	14.57	23.04	1.24	9.71	5.2	319	2.46	297
12-Apr-2022 00:09:11	00:26:00	1	9.88	18.54	20.74	8.66	10.86	10.5	311	2.72	307
21-Apr-2022 22:07:43	18:56:00	1	11.76	13.85	22.59	2.09	10.83	2.7	256	1.52	285
25-Apr-2022 07:16:01	05:56:00	2	20	18.06	19.92	1.94	0.08	7	324	2.28	299
05-May-2022 05:14:33	02:26:00	2	9.88	16.64	16.64	6.76	6.76	5.8	320	1.92	313
11-May-2022 18:04:46	13:56:00	1	9.09	15.54	23.33	6.45	14.24	11.2	322	2.97	306
15-May-2022 03:13:05	00:56:00	2	9.88	13.86	14.75	3.98	4.87	6.8	317	1.76	303
21-May-2022 16:03:17	12:26:00	1	10.53	15.82	16.48	5.29	5.95	5.6	336	2.21	307

Table B.3 continued from previous page

Satellite timestamp	Buoy timestamp	Segment	DPD 46219 [s]	T_s RAW 7-13.5 km [s]	T_s RMC 5-8 km [s]	ABS. ERROR RAW [s]	ABS. ERROR RMC [s]	WSPD 46047 [m/s]	WDIR 46047 [degN]	SWH 46219 [m]	MWD 46219 [degN]
25-May-2022 01:11:36	03:56:00	2	14.29	15.20	23.24	0.91	8.95	1.8	115	1.43	168
31-May-2022 14:01:49	09:56:00	1	10.53	17.12	16.65	6.59	6.12	9.5	320	3.65	307
03-Jun-2022 23:10:07	23:26:00	2	16.67	16.77	17.95	0.10	1.28	9.2	320	2.09	212
20-Jun-2022 09:58:51	05:26:00	1	9.09	17.54	15.99	8.45	6.90	7.1	314	2.59	295
23-Jun-2022 19:07:09	16:26:00	2	9.88	19.73	20.20	9.85	10.32	5.2	317	1.46	309
30-Jun-2022 07:57:23	07:26:00	1	15.38	14.99	14.74	0.39	0.64	5	315	1.87	199
13-Jul-2022 15:04:14	15:56:00	2	13.33	18.17	18.82	4.84	5.49	5.3	320	1.3	200
20-Jul-2022 03:54:27	04:26:00	1	18.18	17.72	17.61	0.46	0.57	4.5	302	1.88	205
02-Aug-2022 11:01:17	12:56:00	2	12.5	12.88	12.38	0.38	0.12	2	255	1.85	179
18-Aug-2022 21:50:02	23:56:00	1	16.67	13.97	16.64	2.70	0.03	6.4	302	1.27	158
22-Aug-2022 06:58:20	08:26:00	2	14.29	14.39	14.16	0.10	0.13	4.9	321	1.22	182
28-Aug-2022 19:48:33	20:56:00	1	15.38	15.17	15.29	0.21	0.09	5.6	319	1.86	182
07-Sep-2022 17:47:05	18:26:00	1	15.38	16.29	15.73	0.91	0.35	1.6	292	1.52	193
21-Sep-2022 00:53:54	00:56:00	2	16.67	15.13	15.75	1.54	0.92	4.9	312	1.81	227
07-Oct-2022 11:42:38	08:56:00	1	13.33	14.61	13.61	1.28	0.28	6.4	311	1.61	267
10-Oct-2022 20:50:56	21:26:00	2	12.5	16.50	18.22	4.00	5.72	5.8	312	1.38	210
17-Oct-2022 09:41:10	09:56:00	1	15.38	14.69	14.01	0.69	1.37	4.8	311	1.16	2
20-Oct-2022 18:49:29	16:56:00	2	12.5	13.29	13.38	0.79	0.88	2.7	296	1.48	293
30-Oct-2022 16:48:01	14:56:00	2	15.38	14.61	16.17	0.77	0.79	8.3	331	2.96	312
09-Nov-2022 14:46:34	12:26:00	2	13.33	14.97	15.75	1.64	2.42	7.7	310	3.06	314
16-Nov-2022 03:36:47	00:56:00	1	15.38	16.37	15.95	0.99	0.57	7.3	324	1.91	300
19-Nov-2022 12:45:06	10:56:00	2	14.29	14.13	13.89	0.16	0.40	3.4	36	2.03	288
26-Nov-2022 01:35:19	00:26:00	1	16.67	18.22	18.69	1.55	2.02	1.4	43	2.36	296
29-Nov-2022 10:43:38	07:26:00	2	9.09	16.93	21.41	7.84	12.32	12.2	316	3.05	305
05-Dec-2022 23:33:51	20:26:00	1	11.11	13.30	14.09	2.19	2.98	6	313	1.99	297
09-Dec-2022 08:42:09	06:56:00	2	14.29	14.11	15.29	0.18	1.00	6.6	336	1.58	299
15-Dec-2022 21:32:22	18:56:00	1	15.38	15.00	15.95	0.38	0.57	0.3	312	1.7	289
19-Dec-2022 06:40:40	05:56:00	2	14.29	15.24	17.64	0.95	3.35	4.3	339	0.84	231
25-Dec-2022 19:30:53	16:56:00	1	15.38	16.77	17.11	1.39	1.73	2.5	320	2.06	305
29-Dec-2022 04:39:11	02:56:00	2	13.33	16.75	16.01	3.42	2.68	2.9	293	3.59	290
04-Jan-2023 17:29:23	15:26:00	1	16.67	16.77	20.45	0.10	3.78	6	179	2.69	282
08-Jan-2023 02:37:41	00:26:00	2	11.76	14.33	16.42	2.57	4.66	3.2	289	3.24	286
18-Jan-2023 00:36:12	00:26:00	2	16.67	17.24	19.88	0.57	3.21	10.4	311	3.3	295
24-Jan-2023 13:26:25	11:56:00	1	22.22	23.46	23.33	1.24	1.11	3.1	347	2.16	288
27-Jan-2023 22:34:44	21:26:00	2	20	18.56	19.07	1.44	0.93	6.8	310	1.67	282

Table B.3 continued from previous page

Satellite timestamp	Buoy timestamp	Segment	DPD 46219 [s]	T_S RAW 7-13.5 km [s]	T_S RMC 5-8 km [s]	ABS. ERROR RAW [s]	ABS. ERROR RMC [s]	WSPD 46047 [m/s]	WDIR 46047 [degN]	SWH 46219 [m]	MWD 46219 [degN]
03-Feb-2023 11:24:58	09:26:00	1	18.18	18.22	17.11	0.04	1.07	1	247	1.45	295
06-Feb-2023 20:33:17	18:26:00	2	13.33	14.90	13.88	1.57	0.55	10.2	331	4.05	295
13-Feb-2023 09:23:30	05:56:00	1	11.11	22.06	23.04	10.95	11.93	9.6	307	3.27	309
16-Feb-2023 18:31:49	15:56:00	2	11.76	13.39	20.77	1.63	9.01	4.4	48	2.34	307
23-Feb-2023 07:22:03	04:56:00	1	14.29	15.87	20.61	1.58	6.32	7.8	273	4.21	317
26-Feb-2023 16:30:21	13:56:00	2	11.76	18.14	18.66	6.38	6.90	5.1	338	2.34	313